

Materials Chemistry of Neural Interface Technologies and Recent Advances in Three-Dimensional Systems

Yoonseok Park,[○] Ted S. Chung,[○] Geumbee Lee,[○] and John A. Rogers^{*}



Cite This: *Chem. Rev.* 2022, 122, 5277–5316



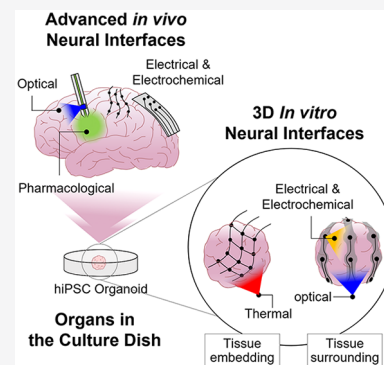
Read Online

ACCESS |

Metrics & More

Article Recommendations

ABSTRACT: Advances in materials chemistry and engineering serve as the basis for multifunctional neural interfaces that span length scales from individual neurons to neural networks, neural tissues, and complete neural systems. Such technologies exploit electrical, electrochemical, optical, and/or pharmacological modalities in sensing and neuromodulation for fundamental studies in neuroscience research, with additional potential to serve as routes for monitoring and treating neurodegenerative diseases and for rehabilitating patients. This review summarizes the essential role of chemistry in this field of research, with an emphasis on recently published results and developing trends. The focus is on enabling materials in diverse device constructs, including their latest utilization in 3D bioelectronic frameworks formed by 3D printing, self-folding, and mechanically guided assembly. A concluding section highlights key challenges and future directions.



CONTENTS

| | |
|--|------|
| 1. Introduction | 5277 |
| 2. Materials for Neural Interfaces | 5279 |
| 2.1. Electrical and Electrochemical Interfaces | 5281 |
| 2.1.1. Nano/Microstructured Materials | 5283 |
| 2.1.2. Stretchable and Viscoplastic Materials | 5284 |
| 2.1.3. Bioresorbable Materials | 5285 |
| 2.1.4. Biohybrid Materials | 5286 |
| 2.2. Optical Techniques | 5286 |
| 2.2.1. Nano/Microstructured Materials | 5288 |
| 2.2.2. Stretchable and Compliant Materials | 5289 |
| 2.2.3. Bioresorbable Materials | 5289 |
| 2.3. Pharmacological Techniques | 5291 |
| 2.3.1. Nano/Microstructured Materials | 5291 |
| 2.3.2. Stretchable and Compliant Materials | 5291 |
| 2.3.3. Bioresorbable Materials | 5292 |
| 2.4. Multimodal Interfaces | 5293 |
| 3. Three-Dimensional Neural Interfaces | 5294 |
| 3.1. Advanced Routes to 3D Structures | 5296 |
| 3.1.1. Three-Dimensional Printing | 5296 |
| 3.1.2. Self-Folding and Self-Rolling Assembly | 5298 |
| 3.1.3. Mechanically Guided Assembly | 5298 |
| 3.2. Implementation of 3D Neural Interfaces | 5299 |
| 3.2.1. Probe Arrays | 5299 |
| 3.2.2. Transformable Mesh Structures | 5299 |
| 3.2.3. Three-Dimensional Printing | 5301 |
| 3.2.4. Self-Rolling and Folding | 5303 |
| 3.2.5. Mechanically Guided 3D Assembly | 5303 |
| 4. Additional Opportunities | 5304 |
| 5. Conclusions | 5305 |

| | |
|-----------------------------------|------|
| Author Information | 5306 |
| Corresponding Author | 5306 |
| Authors | 5306 |
| Author Contributions | 5306 |
| Notes | 5306 |
| Biographies | 5306 |
| Acknowledgments | 5307 |
| References | 5307 |
| Note Added after ASAP Publication | 5316 |

1. INTRODUCTION

Advanced forms of life operate under the control of vast collections of neurons connected into complex networks with physical, chemical, and electrical linkages, embedded in matrixes of various types of cells and supporting structures. The cells in the brain that perform essential neural processes include neurons that specialize in electrical communication over long distances and glia that support this signaling. Diverse types of neurons fall into categories defined by their structure (e.g., unipolar, bipolar, multipolar, anaxonic), function (sensory, motor, interneurons), and origin in the brain (e.g., cortical, cerebellar, thalamic).^{1,2} In the brain of an adult human,

Special Issue: Smart Materials

Received: July 18, 2021

Published: November 5, 2021



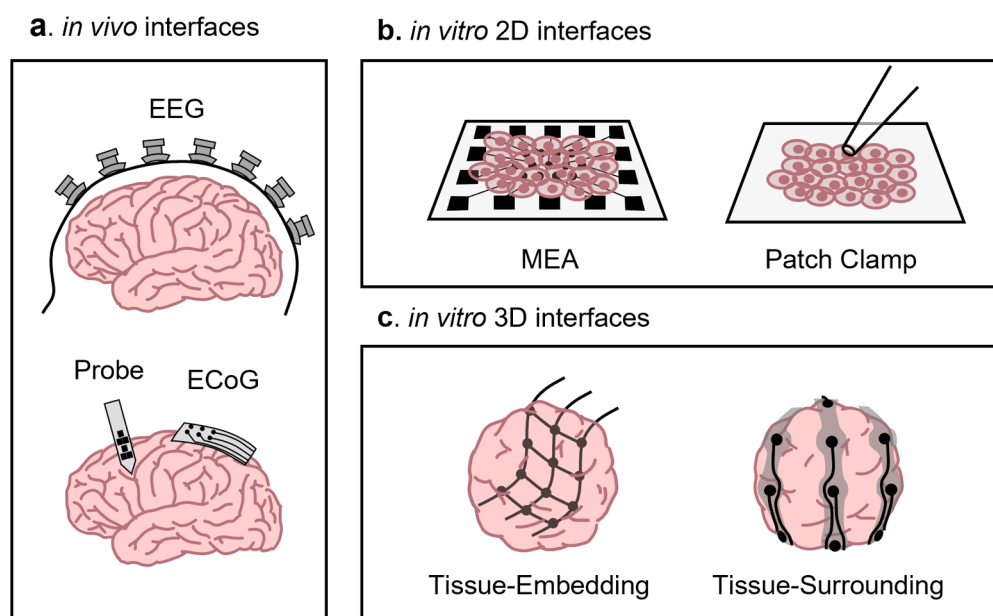


Figure 1. Neural interfaces for various biological systems. (a) *In vivo* neural interface systems include arrays of electrodes attached on the scalp for EEG (top). Related structures can interface directly with the surface of the brain, as the basis of ECoG (bottom). Depths of the brain can be probed using small penetrating shanks with electrodes distributed along their lengths. (b) *In vitro* 2D neural interfaces for thin cell cultures or tissue slices include MEA (left) and patch clamp probes (right). (c) *In vitro* 3D neural interfaces for 3D biological systems include mesh electronics as tissue-embedding systems (left) and 3D bioelectronic frameworks as tissue-surrounding or permeating devices (right).

approximately 86 billion such neurons fill a three-dimensional (3D) space that has a volume of 1000 cm^3 .³ Communication occurs through roughly 4 quadrillion electrical and chemical junctions known as synapses (each neuron receives 1–100 000 synapses) via transport of ions and over 100 different neurotransmitters (e.g., adrenaline, noradrenaline, dopamine, serotonin, γ -aminobutyric acid (GABA), acetylcholine, glutamate, endorphins). Neurons from this central location transmit and receive signals along the spinal cord through axons with lengths that can exceed 1 m, to permeate nearly all parts of the body, as the basis of the peripheral nervous system. A compelling frontier in modern scientific research relies on sophisticated, emerging methods for probing the operation of this complex, extended 3D system, with a goal of establishing a detailed biological and chemical understanding of the underlying processes and governing principles. Successful outcomes will satisfy our basic desire for fundamental knowledge, and they will also establish the basis for treating various forms of brain disorders and, through control of the peripheral nerve interfaces, myriad health conditions that arise from dysfunction of other vital organs.

Wide-ranging types of engineered neural interfaces are available to measure and modulate the activity of these neural networks *in vivo* and *in vitro*. For clinical practice in the context of the brain, such technologies typically involve arrays of a few tens of electrodes that interface with the skin of the scalp or the surface of the brain to capture spatiotemporal variations in electrical potential, through techniques known as electroencephalography (EEG) and electrocorticography (ECoG), respectively (Figure 1a). These devices can provide essential information for investigating and diagnosing degenerative conditions such as Parkinson's^{4–8} and Alzheimer's diseases^{9–11} and also various neurological disorders such as Zika virus induced microcephaly^{12–15} and epilepsy.^{16,17} The resulting signals can also be used as brain–machine interfaces to control prosthetics and other external devices.^{18,19} As sources of

electrical stimulation, the electrodes can activate or inactivate targeted neural networks to eliminate seizures and tremors.^{20,21} In rehabilitation, related types of stimulation can modulate cortical excitability in stroke patients to enhance the effects of training for various tasks associated with daily life.^{22,23} In the context of research, neural interfaces can be applied in wide-ranging animal models for fundamental studies. For *in vitro* experiments that use human induced pluripotent stem cells (hiPSCs), these technologies can be used to explore drugs,^{24,25} genetic diseases,^{26,27} and cancers.^{28,29} Here, electrophysiological measurements^{30–32} occur with multielectrode arrays (MEAs)^{33,34} and patch clamps^{35,36} for thin films of cells (Figure 1b).

Recent progress in tissue engineering provides the basis for culturing stem cells and inducing organogenesis to create 3D, millimeter-scale biological systems that anatomically and functionally resemble real organs such as human neural,^{37–40} retinal,^{41,42} pulmonary,⁴³ renal,⁴⁴ and intestinal⁴⁵ systems. Although the formation and study of such 3D organoids represent areas of growing research activity,^{37,38,46–49} conventional 1D and 2D electrode constructs highlighted in Figure 1b constrain the range of options in studies due to intrinsic geometric and functional limitations associated with these systems. These same considerations prevent many classes of studies of native tissues in animal models and human subjects. Emerging approaches involve mesh-type electronics as tissue-embedding devices^{50,51} and compliant, complex frameworks as tissue-surrounding systems^{52–54} to enable 3D modes of engagement in such cases (Figure 1c), with implications as electrical, optical, chemical, and physical interfaces for measurement and stimulation.

This review highlights the most recent neural interfaces of these types, with an emphasis on underlying topics in materials chemistry and a focus on the central nervous system, specifically brain and brainlike engineered tissues.^{40,54,55} The first sections introduce sensing interfaces and modulation schemes that rely

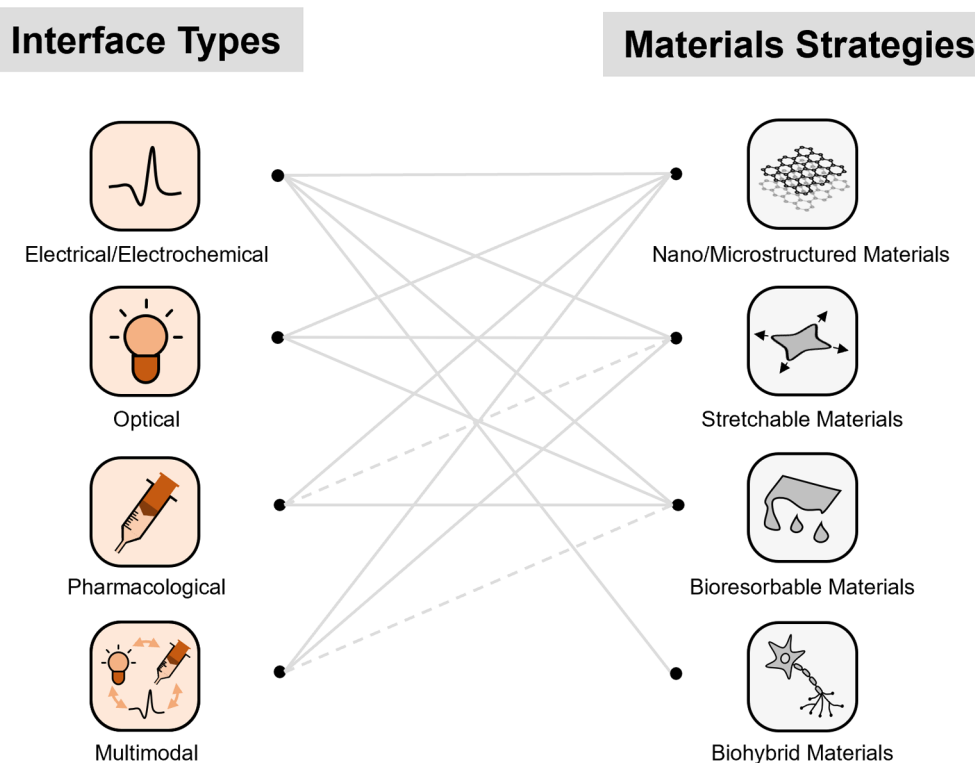


Figure 2. Materials strategies for neural interface technologies. Network diagram that highlights the relationship between electrical/electrochemical, optical, pharmacological, and multimodal sensing or modulating interfaces and associated materials strategies. Diverse approaches in materials chemistry span nano/microstructured platforms and tissue hybrids, to materials with stretchable and bioresorbable characteristics.

on electrical, electrochemical, optical, and pharmacological interactions. *In vivo* and *in vitro* implementations of these neural interfaces with various living systems highlight some of the latest examples. The content then shifts to materials, assembly methods, and techniques for the most recent 3D bioelectronic platforms, primarily in the context of the study of neural organoids and extracellular matrix (ECM) models that exploit hiPSCs, but with additional examples in cardiac tissues and organoids as suggestive of future additional possibilities in neural applications. A concluding section outlines emerging areas where these technologies have the strongest potential, not only for studies of 3D biological tissues but also for control interfaces in biohybrid and prosthetic robotic systems.

2. MATERIALS FOR NEURAL INTERFACES

The fundamental objective of neural interface technologies is to provide a bidirectional link between the nervous system and the outside world. Such capabilities are essential to fundamental studies, and they form core aspects of clinical care, from surgical tools and diagnostics to long-term implants designed to modulate and monitor function. Advanced materials, including organic polymers, composites, nanomaterials, and others, serve as the basis of nano/microstructured systems, devices that have stretchable and bioresorbable properties, and tissue hybrids. Functional interfaces that exploit these materials offer diverse sets of options in both sensing and modulation. This review discusses advanced materials implemented into engineered systems as key elements for the most sophisticated neural interfaces. Figure 2 and Table 1 provide a schematic summary of these topics and a list of characteristics of materials, respectively, as organized for this review. Each interface type is introduced and reviewed through categorized materials strategies. The

implemented items are represented by solid lines, and the ones that have not yet been implemented are displayed by dotted lines. Note that this content does not include interesting, complementary schemes to neuromodulation that rely on base materials not integrated into devices (e.g., nanoparticles with magnetothermal/optothermal functions, sono-optical modulation, nanoscopic and molecular interface materials), as reviewed and reported elsewhere.^{56–63}

The nervous system expresses physiological information in the form of electrical signals and chemical gradients, for processing/storing data, sensing the environment, and controlling organ function.^{1,2} Physiological information captured from the central and peripheral nervous systems (CNS and PNS, respectively) is most powerful when obtained with high spatiotemporal resolution through devices that exploit biocompatible functional materials and device architectures.^{1,2} Capabilities in stimulating or inhibiting neural activity form useful complements to those in sensing; combinations of these two modalities create opportunities in closed-loop control.^{21,64} Electrical, electrochemical, optical, and pharmacological mechanisms of neuromodulation have well-established utility in research into treatments for disorders of the brain, spinal cord, and peripheral nervous systems, and into processes of neuroregeneration. Many examples of these approaches represent the standard of care in clinical practice. Various advances in nano/microstructured, stretchable, bioresorbable, and tissue hybrid material systems for such interfaces define the frontier of this field of engineering science, with vast potential for improved functionality in sensing and modulating interfaces to biological systems, as described in the following sections.

Table 1. Characteristics of Materials

| interface type | materials (dimensions) | implementation | characteristics | refs | |
|--|--------------------------------|--|--|---|----------|
| electrical/electrochemical (section 2.1) | nano/microstructured materials | SiNW (80 nm diameter, 2 μm long) | FET for nanoelectronic scaffolds (16 channels)/3D nanoprobes | 96, 97 | |
| | | nanowire-templated 3D fuzzy graphene (2 \times 2 μm^2 size) | ultramicroscale electrode | surface area, 1017 $\text{m}^2 \text{g}^{-1}$; electrical conductivity, 2400 S m^{-1} | 75 |
| stretchable materials | | Au mesh (70 nm wide, 1 μm pitch, 25 nm thick) coated with PEDOT:PSS (85 nm thick) | transparent electrode | optical transmittance, 70% | 100 |
| | | Au (500 \times 500 μm^2 size, 145 nm thick) encapsulated with PI (2.5 μm thick) | ultrathin electrode arrays | conformal contact on the cortex of brain | 99 |
| | | PFPE-DMA (1 \times 0.5 mm^2 size) coated with PEDOT:PSS | hydrogel-based electrode | Young's modulus, 32 kPa; stable up to 20% strain | 112 |
| | | PDMS with Pt microparticles (0.2–1.8 μm diameter) | 3D printable ink for stretchable electrodes and wires | Young's modulus, 1.2 MPa; stable up to 45% strain | 109 |
| | | PDMS (9 mm long, 5 mm wide, 200 μm thick) coated with PEDOT:PSS | morphing electrodes and wires | Young's modulus, 0.4 MPa; stable up to 100% strain | 115 |
| | | phosphorus-doped SiNM (200 \times 200 μm^2 size, 300 nm thick; dopant concentration, $\sim 10^{20} \text{ cm}^{-3}$) | transient electrode arrays | <i>in vitro</i> degradation time, 15 days (pH 10 at 37 $^\circ\text{C}$); impedance, $\sim 10^6 \Omega$ at 1 kHz | 123 |
| | | Mg (10 mm diameter, 50 μm thick; 34 turns) | coil for energy harvester | <i>in vitro</i> degradation time, 25 days (pH 7.4 at 37 $^\circ\text{C}$); resonance frequency, ~ 5 MHz | 126 |
| | | collagen (100 μm wide, 5 mm long, 30 μm thick) | extracellular matrix (ECM) microelectrodes | improved host tissue integration | 131 |
| | | GaN μ -ILED (25 \times 25 μm^2 size, 6.45 μm thick) | cellular scale optoelectronics | peak wavelength, 447 nm at 1 mA | 160, 161 |
| | | COCE (105–135 μm diameter) | ultrasoft optical fiber | refractive index, 1.51; modulus, 34 MPa; $T_g = 84$ $^\circ\text{C}$ | 173 |
| optical (section 2.2) | stretchable materials | Alg/PAAm (125 μm diameter) | hydrogel-based optical fiber | refractive index, 1.35; modulus, ~ 65 kPa; highly extensible up to 400% | 174 |
| | | PLLA (200 μm diameter) | optical fiber | refractive index, 1.47; bending stiffness, $1.5 \times 10^9 \text{ N/m}$; transparency, 90% at visible light | 178 |
| | | PLGA (150 μm diameter) | optical fiber | refractive index, 1.5 | 179 |
| | | ZnO (001) (20 \times 20 μm^2 size, 200 nm thick) | optoelectronics | peak wavelength, 500–650 nm | 182 |
| | | borosilicate (BS) probe (80 μm o.d., 50 μm i.d.) | minimally invasive probes | nanofluid infusion (single stroke volumes, < 3 nL) and sampling (< 100 nL/min) | 192 |
| | | PDMS (30 \times 30 μm^2 cross-sectional area, 200 μm thick) | stretchable microfluidic channel | Young's modulus, 3 MPa | 196 |
| | | PLA (encapsulant), PLGA (dielectric layer), Mg (electrode) and oxidized starch (reservoir) | bioresorbable electronic patch | <i>in vitro</i> degradation time, 10 weeks | 124 |
| | | PA (5 \times 5 \times 2 mm^3 size) | drug reservoirs | <i>in vitro</i> degradation time, 20 days (pH 7.4 at 85 $^\circ\text{C}$); resonance frequency, 5.14 MHz | 198 |
| | | Mg (2 \times 2 mm^2 size, 50 μm thick) | anode gate | | |
| | | Mg (12 mm diameter, 50 μm thick; 32 turns) | coil | | |
| pharmacological (section 2.3) | nano/microstructured materials | | | | |
| | stretchable materials | | | | |
| bioresorbable materials | | | | | |
| | | | | | |

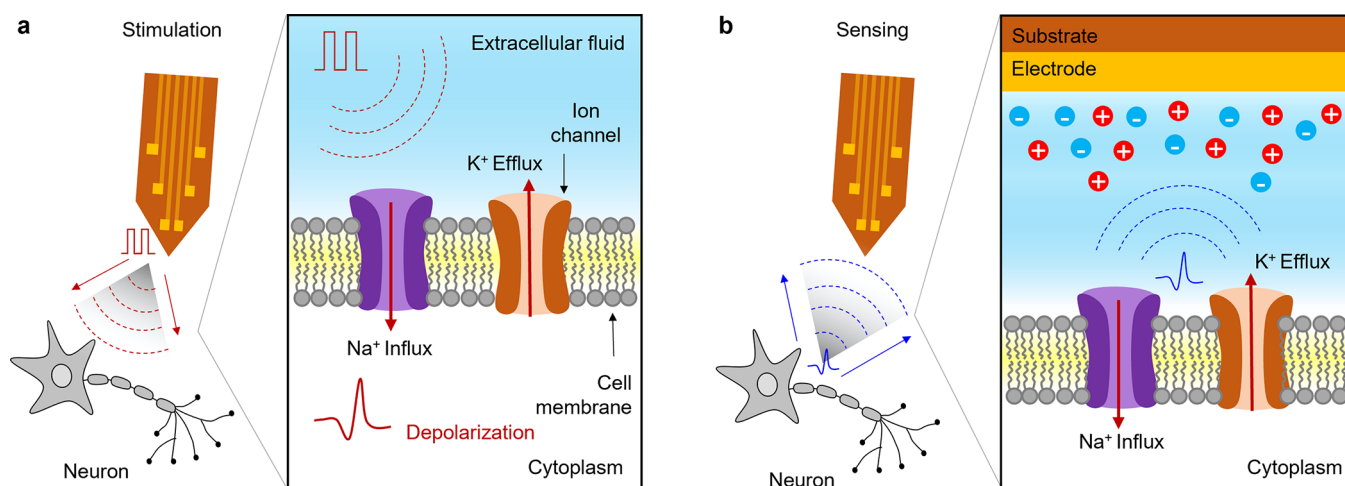


Figure 3. Schematic illustration of electrode-tissue interfaces. (a) Bioelectronic stimulation; electrodes modulate the distribution of ions surrounding the targeted neuron, resulting in evoked firing of an action potential through depolarization of the cellular membrane. (b) Bioelectronic sensing; electrically active neurons modulate the electric fields at the surfaces of the electrodes. Distribution of ionic species act as output signals through the extracellular media to allow for potential recording.

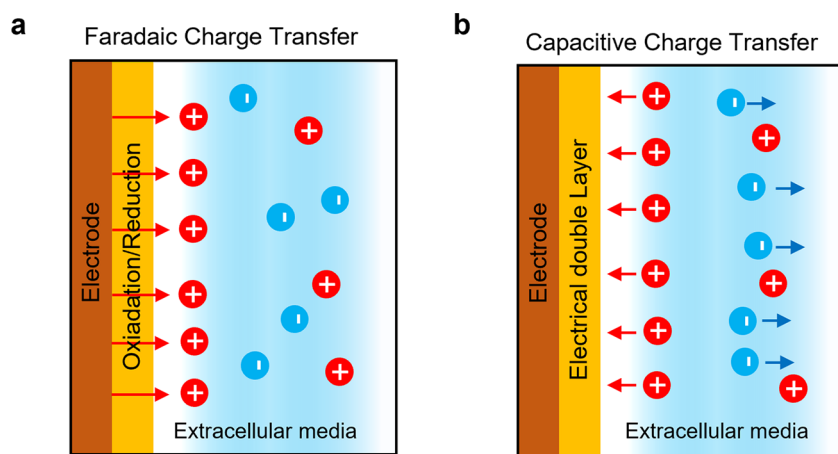


Figure 4. Schematic illustration of mechanisms for charge transfer. (a) Faradaic charge transfer relies on oxidation and reduction of surface-confined chemical species between the electrodes and the surrounding electrolytic media. (b) Capacitive charge transfer relies on charging and discharging of the electrical double layer on the electrode, without electrochemical reactions.

2.1. Electrical and Electrochemical Interfaces

Electrical neural interfaces can be exploited for stimulating and recording neural activity. Here, an understanding of the electrical and electrochemical mechanisms underlying the interactions between electrodes and neurons is important. As a common principle, electrodes mediate bidirectional conversion between the flow of electrons in conductive elements of electronic circuits and those of ions within the intra/extracellular matrixes of the neurons. For bioelectronic stimulation (Figure 3a), a bioelectrical signal (i.e., ionic current) that reaches the targeted axonal membrane and rises above a threshold magnitude can induce a temporary potential difference inside and outside the membrane, thereby firing an action potential. Such membranes contain voltage-gated ion channels that mediate transport of sodium (Na^+) and potassium (K^+) ions into and out of the cell, to regulate gradients in ion concentrations in response to changes in membrane potential. The resting membrane potential for an individual neuron is -70 mV. At a threshold level (typically -55 mV), inflow of Na^+ into the axon results in rapid ($\ll 1$ ms) depolarization ($+30$ to $+40$ mV), as a firing event. Repolarization and relaxation back to the

resting state occurs through release of K^+ from the axon, over a time scale of ~ 1 ms. Arrival of the action potential at the synapse causes release of neurotransmitters from the presynaptic axon to the postsynaptic neuron. These neurotransmitters combine with receptors in the downstream partner dendrite, where receptors convert these chemical signals into electrical signals. This process can repeat, propagating/modifying the initial signal throughout the neural circuitry of the brain.⁶⁵ For bioelectronic sensing (Figure 3b), electrically active neurons modulate electric fields at the surfaces of the electrodes through changes in the distributions of ionic species as output signals through the extracellular media.

The patch clamp, one of the most widely used neural interfaces and a standard method in the field of biological study, enables direct measurements of these potentials with high temporal resolution and signal-to-noise ratio (SNR). This method does not, however, provide straightforward paths to spatial mapping. Systems that include arrays of electrodes overcome this limitation, but as the sizes decrease to support increased densities, the corresponding interface impedances increase and lead to decreases in the SNR. Materials such as

platinum (Pt, specific impedance $4.0 \Omega \text{ cm}^2$ at 1 kHz), gold (Au, $6.84 \Omega \text{ cm}^2$), iridium (Ir, $5.86 \Omega \text{ cm}^2$), and indium tin oxide (ITO, $5.3 \Omega \text{ cm}^2$)⁶⁶ are widely used due to their biocompatibility and high corrosion resistance in biofluids.⁶⁶ Their impedances can, however, be prohibitively high for measurements that demand fine resolution, ultimately to scales defined by the dimensions of single cells. Materials strategies that increase the effective areas of the electrodes without increasing their geometrical sizes are useful in this context. Examples include metallic conductors (e.g., nanoporous Pt black, $0.15 \Omega \text{ cm}^2$) and conductive ceramics (nanotextured titanium nitride (TiN), $0.40 \Omega \text{ cm}^2$; specific impedance at 1 kHz calculated by projected area^{67,68}). As organic materials strategies, conducting polymers and sp^2 hybridized allotropes of carbon are attractive due to their intrinsic conduction mechanisms and their surface area enhancing porosities. Conducting polymers (e.g., poly(3,4-ethylenedioxythiophene) doped with polystyrenesulfonate (PEDOT:PSS), $0.02 \Omega \text{ cm}^2$; polypyrrole (PPy)/carbon nanotube (CNT), $0.77 \Omega \text{ cm}^2$)^{69,70} are of particular, growing interest because their mechanism of operation combines both ionic and electronic modes of conduction, resulting from ion infiltration into their networks and electron transport via conjugated π -electrons, respectively.^{71,72} Carbon-based nanomaterials (e.g., CNT fibers, $0.20 \Omega \text{ cm}^2$; porous graphene, $3.12 \Omega \text{ cm}^2$; 3D “fuzzy” graphene; $0.04 \Omega \text{ cm}^2$)^{73–76} have high conductivities due mainly to their delocalized π -electrons and densities of electronic states that allow them to conduct electrons in ways qualitatively similarly to metals.⁷⁷

Many of these same classes of materials can also be used for bioelectronic stimulation, via transfer of charge at the electrode–tissue interface^{66,78,79} through Faradaic and/or non-Faradaic (capacitive) processes. The former (Figure 4a) involves charge transfer through oxidation or reduction of surface-confined chemical species. In the latter (Figure 4b), ions in the electrolyte accumulate in a double layer on the electrode surface through electrostatic adsorption (charging) and ionic diffusion that extends from the surface (discharging).^{66,78,80} Methods for electrical modulation are well-established in research, and they serve as the basis for various implantable devices that interface onto the surfaces or into the depths of the brain to treat degenerative conditions such as Parkinson’s and Alzheimer’s and neurological disorders such as epilepsy. A key metric for the materials and electrodes in such cases is the charge injection capacity (CIC),⁶⁶ defined as the maximum deliverable charge per unit area. Materials, effective surface areas, geometries, and interface properties are factors that influence the CIC. As with sensing, spatiotemporal resolution is important, and high CIC values are essential for stimulation electrodes to operate effectively at small dimensions. Noble metals such as Pt, Au, Ir, and Pd have CICs in the range of 0.05 – 0.26 mC/cm^2 .^{66,76} Similar to sensing, high porosity metallic conductors and microstructured polymers increase the effective surface areas of the electrodes, leading to enhanced CIC.^{81,82} Superior options are in ceramics (TiN and IrOx),^{66,76} conductive polymers (PEDOT:PSS, PEDOT:CNT),^{76,83,84} and Pt black,⁸¹ where CICs typically lie between 1 and 3 mC/cm^2 , much larger than those of conventional metals.⁶⁶ In the cases of TiN (capacitive) and IrOx (Faradaic), these large CICs result from high surface roughnesses and fast, reversible Faradaic reactions due to reduction–oxidation (redox) reactions with the Ir^{3+} and Ir^{4+} oxidation states, respectively.^{66,78,79} For PEDOT:PSS and PEDOT:CNT (both Faradaic), the PSS allows for charge transfer that causes oxidation in the PEDOT,

resulting in high conductivity and CIC. The CNTs support a distinct and dense matrix structure, resulting in high porosity and improved stabilized performance compared to PEDOT:PSS.⁸⁵

Methods of analytical electrochemistry applied with these and other types of electrodes provide the basis for measuring dynamic fluctuations in the concentrations of biochemicals such as catecholamines (dopamine (DA), norepinephrine, serotonin), metabolites (glucose, glutamate, ethanol, lactate, etc.), and ions (Na^+ , K^+ , O^{2+} , H^+ , etc.). Catecholamines can be detected directly at bare electrodes by measuring their redox signals,^{86,87} while the potential difference between ion-selective electrodes (ISEs) and a reference electrode can be measured through potentiometry as electroactive analytes accumulate on the ISE surface.^{88,89} Amperometry and voltammetry are two of the most common electroanalytical techniques in neuroscience, each with advantages and disadvantages. For example, measurement of analyte-dependent oxidative current at a fixed voltage in amperometry is simple and allows for real-time monitoring of analytes. This scheme cannot, however, differentiate between different catecholamines. Voltammetry overcomes this issue by producing distinct analyte-dependent redox waveforms but requires complex electronics in the form of fast scan analyzers. Unlike amperometry, voltammetry cannot capture real-time transients, though high scan rates can enable near-real-time analysis. Electrodes and detection principles for catecholamine sensing can also be leveraged to monitor metabolites with an additional step of functionalizing the electrodes with specific enzymes that catalytically oxidize metabolites to produce electroactive byproducts. These byproducts can then be readily oxidized/reduced at the electrode for indirect quantification of the metabolites. Electrochemical field effect transistors (FETs) are another means for neurochemical sensing.⁹⁰ Here, a receptor-functionalized gate electrode interacts with the analyte to produce changes in the transconductance of the channel.

The main strategies for improving analytical sensitivity and/or selectivity for detecting neurotransmitters involve chemical surface modification schemes based on polymer coatings, self-assembled monolayers (SAMs), or nanomaterial deposits (nanocrystals, nanowires, nanoparticles, etc.) on the sensing interfaces.^{87,91} An example of the first exploits a layer of PEDOT on an oxide-free metal electrode (e.g., Au) to enable selective detection of catecholamines (e.g., DA) in the presence of biological endogenous interferents (e.g., ascorbic acid (AA) and uric acid (UA)). The PEDOT acts as a redox mediator responsible for oxidation catalysis with the analytical performance determined by voltammetry (oxidation potentials of -40 , 150 , and 280 mV for AA, DA, and UA, respectively).⁹² SAMs can be exploited as linkers to other biological species or nanomaterials. In one case, a SAM of 4-mercaptopyridine (4MPy) on an Au electrode covalently binds Au nanorods or nanoparticles for increased area of detection of neurotransmitters (e.g., DA, epinephrine (EPI), and noradrenaline (NA)) with the analytical performance determined by voltammetry (oxidation potentials of 265 , 350 , and 425 mV for DA, EPI, and NA, respectively).⁹³ As an example of a nanomaterial-based approach without the use of SAMs, hybrid nanocomposites (i.e., Prussian blue (PB) and electrochemically reduced graphene oxide (ERGO)) cast onto Au electrodes lead to enhanced performance in DA sensing compared to bare, RGO-modified, and PB-modified Au electrodes.⁹⁴ The ERGO/PB hybrid nanocomposite enhances the activity for electrocatalytic oxidation of DA with the analytical performance

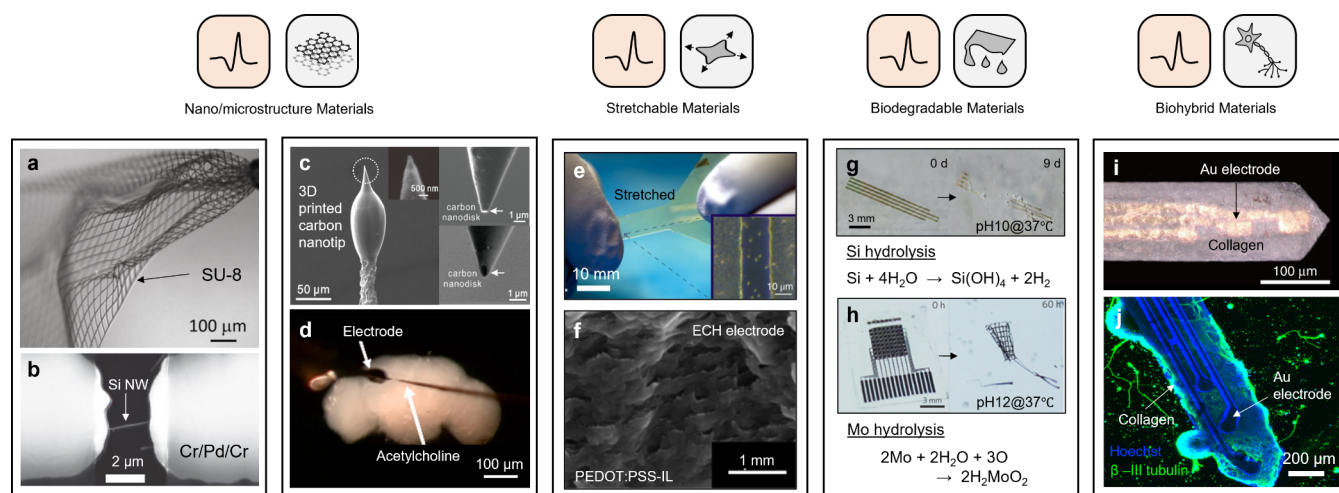


Figure 5. Electrical and electrochemical interfaces. (a–d) Nano/microstructured material systems. (a) Optical microscopic image of mesh electronics in PBS solution and (b) SEM image of a nanowire FET device in the mesh structure.⁹⁸ Reproduced with permission from ref 98. Copyright 2015 Springer Nature. (c) SEM images of a 3D-printed, carbon nanoelectrode with sharp conical geometry and (d) microscopic image of an adult fly brain with the 3D-printed nanoelectrode and a micropipet loaded with acetylcholine.¹⁰⁵ Reproduced from ref 105. Copyright 2020 American Chemical Society. (e, f) Stretchable material system. (e) PEDOT:PSS–ionic liquid based MECH electrode array under tensile stretching. Inset shows a magnified view of the MECH electrode without cracks. (f) Optical image of a hydrated electrically conductive hydrogel with continuous conductive pathway, originating from an interconnected polymer network in the hydrogel.¹¹² Reproduced with permission from ref 112. Copyright 2019 Springer Nature. (g, h) Bioresorbable multiplexed electrode array for transient neural recording. (g) Optical images of accelerated dissolution of an array with patterned SiNMs as neural interface electrodes with the corresponding dissolution chemistry of Si. (h) Mo as an electrical interconnection between multilayers with the hydrolysis reaction of Mo.¹²⁵ Reproduced with permission from ref 125. Copyright 2016 Springer Nature. (i, j) Tissue hybrid material systems. (i) ECM microelectrode integrated on an insertion probe. (j) Confocal fluorescent image showing expression of neuronal marker by cortical neurons grown on the electrodes encapsulated with collagen. Neuronal marker β -tubulin III (green) and nuclei-specific stain Hoechst (blue).¹³¹ Reproduced with permission from ref 131. Copyright 2018 Springer Nature.

determined by amperometry and voltammetry (oxidation potential, 350 mV; linear range, 0.01–10.0 mM; detection limit, 20 nM). As more general approaches, metal/conductive polymer hybrid nanoparticles (e.g., Pt, Fe, and PPy, polyaniline (PANI), and polythiophene (PT)) act as oxidation catalysts and as agents for accelerated electron accumulation on electrodes.⁹⁵

The following sections highlight some advances in materials chemistry that are relevant to electrodes and arrays for electrical and electrochemical sensing and stimulation, with a focus that spans nano/microstructured materials and associated 1D and 2D materials, to platforms that offer stretchable, morphable, and bioresorbable properties.

2.1.1. Nano/Microstructured Materials. In addition to the types of nanomaterials described above, recent work shows that deterministically defined nano/microstructures, such as thin membranes, flexible filaments, and open mesh architectures, offer unique possibilities for functional integration with biological systems. As an example, mesh electronic systems (350–400 nm thick; Figure 5a) that include fine conductive elements and, in some cases, integrated silicon nanowires (SiNWs; 80 nm diameter, 2 μ m length; Figure 5b) as the basis of field effect transistors (FETs)^{96,97} can be designed to interpenetrate 3D biological tissues for *in vivo* neural recording. One example describes the injection of such device structures into the brains of mice for electrophysiological recordings characteristic of single-cell action potentials with spatiotemporal mapping of hippocampal field activity. The nanoscale geometry yields certain physical properties that are similar to those of the neurons themselves, for improved long-term stability of operation.⁹⁸ A related system uses ultrathin, microscale electrode arrays (Au electrode; 500 \times 500 μ m² size and 145 nm thick) on polyimide (PI) mesh substrates (2.5 μ m thick) designed for placement on the surfaces of the brain using

dissolvable silk fibroin sheets as temporary supporting layers. Dissolution of the silk allows gentle, conformal contacts to form between the textured tissue surfaces and the neural interface platform, with minimal mechanical loading at points of contact. An *in vivo* study demonstrates successful mapping of neural activity from a feline animal for more than 4 weeks.⁹⁹

Additional examples of nanostructured materials strategies focus on increasing the effective area of the electrodes, such as nanowire-templated 3D fuzzy graphene (NT-3DFG). This type of construct reduces the neural interface impedance by 40 times compared to that of bare Au electrodes with the same projected area. Fabrication of NT-3DFG begins with preparation of SiNWs (30–160 nm diameter) through Au nanoparticle (NP) catalyzed vapor–liquid–solid growth and concludes with the formation of graphene by plasma enhanced chemical vapor deposition (PECVD). The effective area of NT-3DFG allows for geometric scaling of microelectrode sizes to dimensions as small as 2 \times 2 μ m², for *in vitro* electrical recording with high SNR from cardiomyocytes.⁷⁵

Interesting optical properties are also possible with nano/microstructured materials. For example, optically transparent microelectrode arrays can be constructed using bilayer nanomesh systems of Au and PEDOT:PSS (Au nanomesh; 25 nm thick with mesh widths of 70 nm and pitch values of 1 μ m; electroplated PEDOT:PSS; 85 nm thick), with 70% optical transmittance in the visible range and with electrical impedances comparable to those of standard nontransparent electrodes.¹⁰⁰ As additional material schemes, devices based on indium tin oxide (200 μ m diameter, 0.1 μ m thick)¹⁰¹ and single- or few-layer sheets of graphene (110 μ m diameter; 0.3 nm layer thick)¹⁰² exhibit transmittances of 70 and 90% with sheet resistances of 12 and 76 Ω /sq, respectively. Optical access enables simultaneous use of routine microscopy methods, as

well as emerging methods for optical stimulation and sensing, as described in subsequent sections.

In other applications, electrodes functionalized with nanomaterials allow detection of important biochemical species such as catecholamines, as previously described. As an example, a sulfonated tetrafluoroethylene based fluoropolymer–copolymer and PEDOT can be used as a composite electrode coating for enhanced performance in electrochemical sensing. Such composites formed by electropolymerization (100 nm thickness) on the surfaces of carbon fiber microelectrodes (40–80 μm length, 0.68 mm diameter) result in negatively charged electrodes with selectivity toward cations. Electrochemical sensors of this type exhibit sensitivities of 26 nA μM^{-1} and response times of 0.46 s for measurements of DA using voltammetry. Slow scan cyclic voltammetry (20 mV/s) as performed on solutions of 1.0 mM DA, 3,4-dihydroxyphenylacetic acid (DOPAC), and AA in 20 mM pH 7.4 phosphate-buffered saline (PBS) validates the selectivity of the coating against DOPAC and AA. The steady-state current for a 1.0 mM DA voltammogram is stable, while those for DOPAC and AA decrease, indicating that the coating is effective in preventing anion adsorption.¹⁰³

Another example of electrode functionalization uses enzymes to enable simultaneous *in vivo* recording of concentrations of glutamate and ascorbate. One reported structure involves a microsensor array with two pairs of side-by-side Pt sites (15 μm wide, 333 μm long) coated with glutamate oxidase. Measurements show the ability to monitor potassium-evoked glutamate release and reuptake in the hippocampus region of a rat model with a sensitivity of 5.3 pA μM^{-1} , a response time of 0.9 s, and high selectivity against major interferents.¹⁰⁴ Printing and focused ion beam approaches can yield nanoscale electrodes (tip sizes of 260–290 nm) capable of neurotransmitter detection by fast scan cyclic voltammetry (FSCV) in microorganisms (*Drosophila* with 10- μm -wide brain structures). After stimulation with acetylcholine (2 pmol), experiments show that DA can be detected in the brains of flies at the nanotips of carbon electrodes (300 nm disk; Figure 5c,d).¹⁰⁵

Another recent study reports six electrochemical ion selective electrodes embedded within a thermally drawn fiber (a process described in section 2.2) for pH and neurometabolic lactate sensing that combines nanomaterial and enzyme electrode functionalization.¹⁰⁶ The potentiometric pH sensor in this case consists of a 5% graphite and conductive polyethylene composite (gCPE) coated with iridium oxide (IrOx) to yield a sensitivity of -56.6 mV/pH. The lactate sensor uses lactate oxidase to oxidize lactate for amperometric measurements of hydrogen peroxide (H_2O_2) on a carbon electrode electroplated with Pt black. The sensitivity is 2.63 nA/mM, via electrodes that have active electrochemical areas of ~ 42 – 85 μm^2 . *In vivo* experiments in the frontal cortex of mouse models capture changes in lactate concentration in response to spreading depolarizations due to brain needle pricks.

2.1.2. Stretchable and Viscoplastic Materials. Because neural circuits distribute throughout soft, time-dynamic tissues, reliable electrical/electrochemical interfaces benefit from the use of compliant materials that can respond to these natural motions without constraint or damage, for interfaces with long-term stability. Although a certain level of such compliance can be achieved using nano/microstructured materials as described previously, these properties can be most directly realized through appropriate chemical designs of the constituent materials. Parylene and poly(dimethylsiloxane) (PDMS; typical

moduli between 3 and 0.05 MPa following mixing of cross-linker and PDMS) represent two polymer materials commonly used as bendable encapsulation layers and elastomeric substrates, respectively. Conducting polymers (e.g., polypyrrole/polycaprolactone-*block*-polytetrahydrofuran-*block*-polycaprolactone (PPy/PCTC)¹⁰⁷ and PEDOT:PSS¹⁰⁸) are attractive as electrodes and interconnects for these same reasons. These materials also have the advantage that they can be patterned using additive approaches, including methods in 3D printing, as described subsequently. Composites that consist of Pt microparticles,¹⁰⁹ Ag nanowires,¹¹⁰ or Au-coated TiO_2 nanowires embedded in PDMS matrixes¹⁰⁷ serve as the basis for electrical sensing interfaces that can not only bend but also stretch (strains $\gg 1\%$). Hydrogels represent an interesting additional class of materials that can offer similar and even more favorable mechanical properties (e.g., moduli as low as 10 kPa), with ionic modes of conduction.^{78,111}

One example of tissuelike stretchable electrical interfaces uses an electrically conductive hydrogel (ECH) formed by blending ionic liquid (4-(3-butyl-1-imidazolium)-1-butanedisulfonic acid triflate) into a solution of PEDOT:PSS to form an ion gel film with an aggregated PEDOT network (Figure 5e,f). Subsequent removal of the ionic liquid via water exchange transforms the ion gel into a hydrogel. ECH electrodes (200 nm thick) are mechanically and electrically stable under tensile strains of up to 20%.¹¹² Direct photolithographic patterning of hydrogels is generally not possible due to their porosity and high water content, but the ion gel can be processed using such techniques to create micropatterned electrically conductive hydrogels (MECH) through water exchange to yield desired structures in ECH (32 kPa Young's modulus, 1×0.5 mm² size). An elastomeric photoresist formed by mixing dimethacrylate-functionalized perfluoropolyether (PFPE-DMA) with a photoinitiator (bis(2,4,6-trimethylbenzoyl)-phenylphosphine oxide) serves as a photodefinable encapsulation layer. These strategies allow the formation of micropatterned functional layers of MECH with coatings of PFPE-DMA as the top and bottom encapsulation layers, all with stretchable and chemically stable characteristics. The resultant interfaces can be used for localized low-voltage electrical stimulation of the sciatic nerves in live mice.

Other chemical modifications can render PEDOT:PSS as a conducting polymer suitable for patterning by 3D printing through tailored rheological properties. The modifications focus on the formation and isolation of PEDOT:PSS nanofibrils from PEDOT:PSS solutions through lyophilization in cryogenic conditions and redispersion in a mixture of water and dimethyl sulfoxide (DMSO) (volume ratio, water:DMSO = 85:15). High-resolution 3D printing of this material yields electrodes (PEDOT:PSS; 1.1 MPa modulus, 30 μm diameter) within elastomeric encapsulation layers (PDMS) as neural probes with multiple PEDOT:PSS electrode channels suitable for high-quality biopotential recordings from the dorsal hippocampus regions of the brains of mice.¹⁰⁸ In other examples of 3D printing, conductive inks of Pt microparticles (0.2–1.8 μm diameter) dispersed in PDMS form the basis of stretchable implants in different geometries for studies with various animal models (rat spinal implant (55 mm long, four channels); cat spinal implant (65 mm long, eight channels); rat EcoG implant (31 mm long, nine channels); muscle nerve implant (15 mm long, one channel); all ~ 200 μm thick) to stimulate and record electrical activity from the brain, spinal cord, and peripheral nerves.¹⁰⁹

Another stretchable platform, known as electronic dura mater (e-dura) formed by soft lithographic techniques, involves a silicone substrate (PDMS, 120 μm thick) with Pt–PDMS composite electrodes (300 μm diameter) and microfluidic channels (100 \times 50 μm^2 cross-section area) as an electrical and chemical interface to the spinal cords of rodents. The system has an effective modulus of \sim 1.2 MPa and an elastic response to strain of up to 45%. Experimental demonstrations illustrate its ability to restore locomotion in paralyzed rodents after 5 weeks of implantation.¹¹³

Materials with extremely low modulus are also of interest. A recent report outlines an ultrasoft (10–100 kPa) and stretchable electrode array platform (6 \times 20 \times 0.250 mm³ dimensions) as an ECoG device constructed entirely out of viscoelastic materials designed to interface with the soft tissues of the heart and brain (electrodes with diameters of 700 μm and average impedances of 167 k Ω).¹¹⁴ The conductive layer consists of alginate doped with pyrene-modified graphene flakes and CNTs, while the encapsulation layer is based on self-healing PDMS (PDMS–methylenebis(phenyl isocyanate)–isophorone diisocyanate (PDMS–MPU–IU); 10 μm thick) physically entangled with amine-terminated PDMS (NH₂–PDMS–NH₂) to covalently bond to an alginate–acrylamide-based tough gel through carbodiimide chemistry. An ECoG device placed onto the dura of a transgenic rat expressing Thy1 records electrical signals in response to optical stimulation from the primary cortex. Placement over the auditory cortex of a wild-type rat allows recording of auditory evoked potentials in response to vocal stimulation from 1 to 10 kHz frequency.

As extensions of stretchable neural interfaces, related classes of materials can be designed to follow large-scale physical and dimensional changes associated with growth and morphogenesis. Here, the resulting spatially nonuniform distributions of stresses and strains can be much larger than those associated with movements. Interface technologies that maintain stable contacts throughout these processes can allow for sensing and modulation across the duration of these periods of growth and change. In such instances, significant and permanent alteration in dimensions/shapes of the neural interface materials must occur in a coordinated manner with the biological systems, often beyond the range of elastic responses. Viscoplastic materials such as PEDOT:PSS doped with glycerol or PDMS mixed with isophorone bisurea and 4,4′-methylenebis(phenyl urea) are attractive as the foundations for such types of morphing electronics (MorphE).¹¹⁵ One demonstration vehicle incorporates four electrodes (0.04 cm² area and 2 μm thick) as interfaces to peripheral nerves in growing, juvenile rats for periods of up to 8 weeks. Experiments show stable electrical interfaces for eliciting compound action potentials, with therapeutic benefits on the nerve in terms of effects on gait, behavior, nerve structure, and histology. Similar strategies may be applicable to the brain and other parts of the CNS.

Other types of deformable neural interfaces exploit tunability in stiffness to facilitate tissue penetration in a stiff state, with subsequent transition to a compliant state to minimize mechanical damage during use. One such probe uses PDMS as its structural material with Pt electrodes (40 \times 150 μm^2 area) for electrical/electrochemical interfaces and with microfluidic channels for drug delivery (15 \times 5 μm^2 cross-sectional area) and stiffening (104 \times 10 μm^2 cross-sectional area). Here, the liquid metal gallium (Ga) acts both as a stretchable electrical connection and as a material with tunable stiffness through a phase change process. Specifically, during deep brain

implantation, the temperature of the probe is controlled to ensure that the Ga is in its solid phase (under 30 °C) with a modulus of 205 kPa. After implantation, the Ga melts to eliminate its stiffening effect on the probe. In this system, Pt electrodes serve as the basis of enzymatic biosensors to detect glutamate. Electropolymerization of *m*-phenylenediamine yields a layer of poly(*m*-phenylenediamine) (PPD) to block common electroactive interferents in the rat striatum such as DA and AA. Following PPD deposition, enzyme immobilization occurs by applying a mixture of glutamate oxidase and bovine serum albumin, resulting in a stable, high-performance glutamate sensor (sensitivity, 8.2 pA/ μM ; detection limit, 0.39 μM ; and response time, \sim 1 s).¹¹⁶

2.1.3. Bioresorbable Materials. Temporary neural interfaces are of interest for applications that require only finite operating lifetimes, selected to match transient biological processes such as those related to neurotherapy, neuroregeneration, and/or recovery. Bioresorbable materials can enable platforms that harmlessly disappear, without the complications and risks associated with secondary surgeries that would otherwise be required for device retrieval after a period of need. Physical dissolution, biochemical degradation, and physical disintegration represent some of the mechanisms for resorption. As summarized in other reviews,^{117,118} materials ranging from Si nanomembranes (NMs) and zinc oxide (ZnO) thin films can serve as active semiconductor materials for such interfaces, in which the underlying chemistry of resorption involves hydrolysis reactions with surrounding biofluids. Similar reactions that occur with conductors and insulators such as silicon (Si), magnesium (Mg), zinc (Zn), molybdenum (Mo), and tungsten (W) allow for their use as electrodes and interconnects;^{118–121} with silicon dioxide (SiO₂), magnesium oxide (MgO), and silicon nitride (SiN_x) as gate and interlayer dielectrics;^{118,120,122,123} and with poly(lactic-co-glycolic) acid (PLGA), polylactic acid (PLA),⁶⁵ poly(vinyl alcohol) (PVA),¹²⁴ polycaprolactone (PCL), collagen, and silk fibroin as substrates.^{118–120,123} These and other related materials can be cleared from the body through metabolic processes, without harmful biological effects.

Examples of bioresorbable electrical sensing interfaces include passively and actively addressed arrays of doped SiNM electrodes and Mo electrodes, with demonstrations of electrophysiological mapping of neural activity on the cortex of rat models (Figure 5g,h).¹²⁵ Stable recordings are possible for many days, and complete resorption occurs within several weeks. Such devices can, in many cases, also be used for neural stimulation, as demonstrated by a wireless, temporary interface designed to accelerate processes of neuroregeneration in damaged peripheral nerves.¹²⁶ The device in this case consists of a radio frequency (RF) power harvester that includes a Mg receiver coil and a rectifying diode based on a SiNM that connects to a pair of Mg or Mo electrodes as cuff interfaces to the nerve, all supported and encapsulated by PLGA. *In vivo* experiments on rat models demonstrate advantages of repeated stimulation with devices of this type over a period of 1 week, compared to current standards of care based on a single stimulation process performed during the intraoperative period.

Bioresorbable materials can also be used as chemical sensing interfaces. For example, iron (Fe) NPs can serve as catalytic oxidizing agents of dopamine. An example of a bioresorbable electrochemical sensor constructed on this basis consists of a SiNM (300 nm thick) heavily doped with boron (\sim 10²⁰ cm⁻³) and coated with a hybrid catalyst of Fe-decorated carboxylated

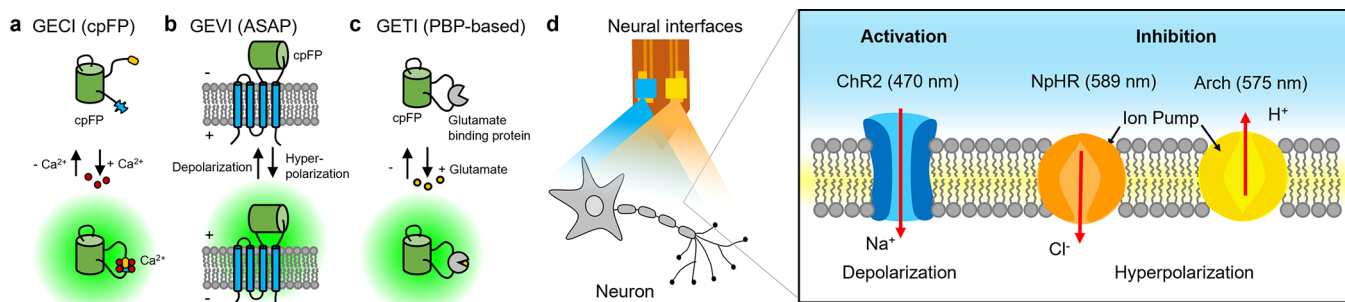


Figure 6. Schematic illustration of mechanisms for optical sensing and modulation. (a) Illustration of a genetically encoded Ca^{2+} indicator (GECI), where binding to calcium ions enhances its fluorescence upon excitation with 473 nm light. (b) Genetically encoded voltage indicator (GEVI) based on cpFPs inserted between S3 and S4 of a voltage-sensing domain. Hyperpolarization leads to an increase in fluorescence. (c) Penicillin-binding protein (PBP) based genetically encoded transmitter indicator (GETI) relies on cpFPs inserted into the glutamate binding protein. Upon binding, the change in conformation leads to an increase in fluorescence. (d) Integrated optoelectronic devices as neural interfaces illuminate light onto photosensitive cells. Blue light (470 nm wavelength) opens the cation ChR2 channel and induces an influx of sodium and calcium ions into the intracellular media. Exposure to yellow and orange light (575 and 589 nm wavelength) can activate the Arch and NpHR ion pumps, allowing expulsion of hydrogen ions and introduction of chloride ions, resulting in hyperpolarization.

polypyrrole NPs (Fe_CPPy NPs, 5 and 100 nm sizes) as functionalized electrodes, Mg as interconnects (200 nm thick), SiO_2 as the interlayer dielectric (150 nm thick), and PCL (100 μm thick) as the substrate and encapsulation. When dopamine molecules adsorb onto the CPPy surface of the hybrid NPs, the six-membered benzene rings in the dopamine molecules fuse to nitrogen-containing rings of CPPy via π - π interactions. Fe-NPs catalyze the accumulated dopamine to its oxidized form (i.e., dopamine-*o*-quinone), thereby generating electrons that transfer to the SiNM electrodes. The resultant electrochemical responses encompass a wide range of dopamine concentrations, as low as picomolar values *in vitro* and with resorbable characteristics demonstrated under accelerated conditions in phosphate-buffered saline (PBS, pH 11 at 37 $^\circ\text{C}$).¹²³

Real-time monitoring of nitric oxide (NO) levels in physiological environments can be important for sensing neural activity due to the regulatory role this compound plays in the release of neurotransmitters.¹²⁷ A recently reported bioresorbable electrochemical sensor enables NO detection (detection limit, ~ 4 nM), over a wide range (0.01–100 μM) and with high temporal resolution (< 350 ms). The device consists of poly(L-lactic acid) and poly(trimethylene carbonate) (PLLA-PTMC, 400 μm thick) as the substrate, ultrathin AuNM (32 nm thick) as electrodes, and a poly(eugenol) film (~ 16 nm thick) as the selective membrane to promote selectivity and specificity toward NO.¹²⁸ The AuNMs are bioresorbable not through conventional chemical processes but instead through phagocytosis and metabolic clearance. The electrochemical sensing mechanism involves the oxidation of NO to NO^+ (nitrosonium ion) through the removal of one unpaired electron on the AuNM surface, followed by a subsequent conversion to NO^{2-} in the solution. The resulting redox current can be measured to detect the concentration of NO. The device can monitor not only at cellular and organ levels in real time but also in a live rabbit model for 5 days with a wireless system.

2.1.4. Biohybrid Materials. An interesting additional direction in materials for electronic/electrochemical interfaces combines living cells with electrodes, substrates, encapsulating layers, and other supporting materials. The concept, initially described decades ago and currently a topic of growing research activity, involves two main strategies: seeding cells onto the electrodes by coating them with ECM proteins (e.g., collagens I and IV, fibronectin, and laminin) or allowing cells to grow

through the electrodes to yield “living electrodes” in the form of microtissue engineered neural networks (microTENN).^{129–132}

Here, natural growth of the cellular component can lead to intimate, dynamic integration into a host biological system, to form electrically active neurite bridges. The interest in this living, natural electronic interface is in its potential to reduce or eliminate foreign body reactions while maintaining recording or modulating capabilities. The ECM probes, shown in Figure S1j, not only operate with minimal immune response but also act as implanted electrical hybrid interfaces to monitor evoked neural activities from rat models. Probes based on microelectrodes (Au electrodes and conductive traces, 100 nm thick; parylene as top and bottom encapsulation layers, 5 μm thick; and overall dimensions of 100 $\mu\text{m} \times 30 \mu\text{m} \times 5$ mm ($W \times H \times L$)) coated with ECM proteins, excluding collagen I, show higher cell viability compared to those without the proteins.¹³¹ In other work, microTENN are neuronal cultures with functional axonal tracts seeded within agarose–collagen hydrogels and molded into cylindrical microcolumns to grow toward target tissue. Different types of neurons can be used in these constructs to stimulate and inhibit neural activity (excitatory and inhibitory neurons, respectively). The diameters of such probes are in the range of several hundred micrometers and with lengths of 5–10 cm to reach deep layers of the brain.^{132,133} Transfection of the neurons in these living electrodes with optogenetic proteins enables optical modulation and evoked neural activity in the host brain as monitored through calcium imaging of the living electrodes,¹³⁴ via mechanisms described in section 2.2.

2.2. Optical Techniques

Optical techniques represent powerful approaches that complement electrical methods for monitoring and modulating neural activity. These schemes are of particular interest for their ability to address volumes of tissues through the use of projection optics, without the invasiveness of electrical probes, and for their capacity to operate with cell type specificity. Although optical monitoring can track intrinsic hemodynamic effects related to neuronal activity including variations in blood flow and concentrations of oxy-/deoxyhemoglobin,^{135,136} the most powerful schemes exploit genetically encoded proteins with fluorescence that varies according to changes in intracellular calcium ion (Ca^{2+}) concentration, membrane voltages, or neurotransmitters.¹³⁷ The mechanisms often involve modulations in the fluorescence efficiency via energy transfer from one

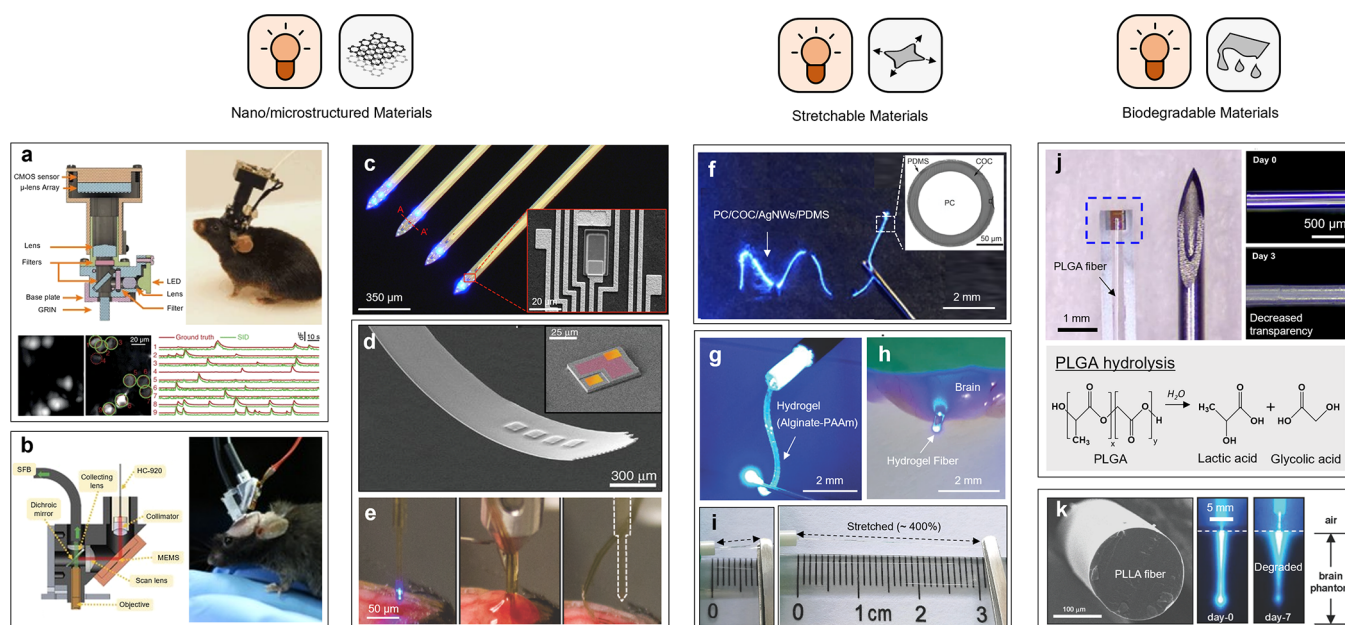


Figure 7. Optical interfaces. (a–e) Nano/microstructured materials. (a) Illustration of the miniature light field microscope (MiniLFM) consisting of CMOS sensor, microlens array, lens, base plate, LED, and graded index (GRIN) lenses (top left), photograph of a MiniLFM mounted mouse, and comparison of representative neuron positions and activity traces as obtained from two photon microscopy recording (red circles and traces) and from seeded iterative demixing (SID) analysis (green circles and traces) of a simultaneous MiniLFM recording of the same region.¹⁵⁶ Reproduced with permission from ref 156. Copyright 2018 Springer Nature. (b) Illustration of a 2D MEMS scanner consisting of supply fiber bundle (SFB); dichroic mirror; collecting, scanning, and objective lenses; collimator; and hollow-core photonic crystal fiber (left) and photographs of an FHIRM-TPM on a fingertip and mounted on the head of a mouse (right).¹⁵⁷ Reproduced with permission from ref 157. Copyright 2017 Springer Nature. (c) Optical microscopic and SEM (inset) images of four silicon optical probes and μ -ILEDs on an array of probes.¹⁶¹ Reproduced with permission from ref 161. Copyright 2015 Elsevier. (d) SEM images of an ultrathin probe and (inset) single GaN-based μ -ILED. (e) Process of injection and release of the microneedle; insertion (left), dissolving the external silk-based adhesive (center), and removing the microneedle to leave the device components in the brain (right).¹⁶² Reproduced with permission from ref 162. Copyright 2013 American Association for the Advancement of Science. (f–i) Stretchable materials. (f) Photograph of a fiber (PC/COC coated with Ag NWs/PDMS) for optoelectronic probing. Cross-sectional image of the fiber probe (inset).¹⁷³ Reproduced with permission from ref 173. Copyright 2017 American Association for the Advancement of Science. (g) Optical image of an Alg/PAAm hydrogel optical fiber and demonstrations of light passing into a mouse brain (h) and fiber stretchability (i).¹⁷⁴ Reproduced with permission from ref 174. Copyright 2018 Wiley-VCH Verlag GmbH & Co. KGaA. (j, k) Bioresorbable materials. (j) PLGA-based bioresorbable optical fiber for characterization of neural activity (top right). PLGA fibers lose their function as time passes (bottom right).¹⁷⁹ Reproduced with permission from ref 179. Copyright 2019 Springer Nature. Chemical reaction associated with PLGA hydrolysis (bottom). (k) SEM image of PLLA-based bioresorbable optical fiber (left) and optical characteristics in a brain phantom over time (right).¹⁷⁸ Reproduced with permission from ref 178. Copyright 2018 Wiley-VCH Verlag GmbH & Co. KGaA.

donor fluorophore to another through intermolecular dipole–dipole interactions^{138,139} in a Förster resonance energy transfer (FRET) process. Here, binding events alter the molecular conformations and, thus, the efficiency of FRET. Genetically encoded calcium indicators (GECIs, Figure 6a) are of particular importance due to their widespread use. Some of the most common GECIs include fusions of green fluorescent protein (GFP), the calcium-binding protein calmodulin (CaM), and the M13 fragment of myosin light chain kinase to yield the GCaMP family of Ca^{2+} indicators.¹⁴⁰ These sensors exploit circularly permuted fluorescent proteins (cpFPs) that undergo conformational changes upon Ca^{2+} binding, to yield fluorescence modulation speeds that approach the scale of naturally occurring transients, faster than those possible using FRET-based approaches, as extensively reviewed elsewhere.^{137,141}

While Ca^{2+} concentrations are important, they represent indirect measures of neuronal activity. Genetically encoded voltage indicators (GEVIs, Figure 6b) enable direct visualization of neuronal action potentials.^{137,142} GEVIs span a wide variety of designs and mechanisms, with functional limitations that follow from generally low response amplitudes and relatively slow kinetics. Continued improvements with GEVIs, with examples such as accelerated sensor of action potentials 3 (ASAP3),¹⁴³

SomArchon,¹⁴⁴ and Voltron,¹⁴⁵ are beginning to address these limitations, as reported and reviewed elsewhere.¹³⁷ Lastly, because neurotransmitters are key biochemicals involved in neuronal signaling processes, genetically encoded transmitter indicators (GETIs, Figure 6c) are of interest as a third form of species for optical monitoring of presynaptic or postsynaptic neurotransmission. Advances in the development of cpFP biochemistry allow detection of various types of neurotransmitters (e.g., GABA,¹⁴⁶ dopamine,^{147–149} and glutamate¹⁵⁰).

Related genetic techniques support optical modulation of neural activity, using light with wavelengths spanning from infrared (IR) through the visible spectrum, at high spatiotemporal precision and with cell-type specificity. These methods, known collectively as optogenetics,^{151,152} exploit genetically encoded light-sensitive ion channels or pumps that express in the membranes of targeted neurons for activation or inhibition (Figure 6d). In one common example of activation, illumination with blue light (470 nm wavelength) opens a cation channel (e.g., channelrhodopsin-2 (ChR2)) to allow an influx of Na^+ or Ca^{2+} ions, resulting in neural activation by depolarizing the membrane potential. As an example of inhibition, illumination with yellow or orange light (575 and 589 nm wavelength,

respectively) activates pumps based on archaerhodopsin-3 (Arch) or halorhodopsin (NpHR) to expel hydrogen ions or introduce chloride ions, respectively, thereby inhibiting neural activity by hyperpolarizing the membrane.^{65,153,154} As described in the following, advances in materials chemistry and engineering serve as the basis for devices capable of introducing and detecting light to support these optical techniques in neural sensing and modulation.

2.2.1. Nano/Microstructured Materials. Optical recording methods that use optical fiber probes and genetically encoded indicators can provide powerful insights into neuronal activity, but they can be limited to local brain regions, ultimately hindering the potential to visualize networked brain activity.¹⁵⁵ High spatiotemporal resolution can be achieved with lenses and imaging systems arranged into compact platforms to capture volumetric neuronal behavior.¹⁵⁴ One study (Figure 7a) exploits a single-photon, wide field fluorescence microscope to enable neuronal recordings of Ca²⁺ transients within a 700 × 600 × 360 μm³ volume, across 810 neurons with nearly single-cell resolution in the hippocampus of freely moving mice expressing GCaMP6f at high sampling rates (16 Hz) and fine resolution (~15 μm).¹⁵⁶ Miniaturized two-photon microscopes (FHIRM-TPMs) allow recordings in freely moving mice expressing GCaMP6f with high spatiotemporal resolution (0.64 μm laterally, 3.35 μm axially, 40 Hz sampling rate for an area of 130 × 130 μm²).¹⁵⁷ These systems include photonic crystal fibers (~400 μm total diameter) consisting of silica cores (8–9 μm diameter) and acrylate coatings (255 μm diameter) that deliver 920 nm femtosecond laser pulses, with microelectromechanical systems (MEMS) as scanners for imaging capabilities (Figure 7b).

Standard fiber optics technologies adapted from the telecommunications industry are also useful, but rigid (~50–90 GPa) glass probes or waveguides of such types are strongly mechanically mismatched with soft neural tissues (~1–10 kPa), thereby limiting stability in long-term *in vivo* experiments.¹⁵⁴ Tapered fibers (TFs) can reduce this sort of tissue damage, and microstructured features patterned along their lengths can enable multisite illumination and photon collection.¹⁵⁸ An example involves a single-core optical fiber (50 μm core diameter; 125 μm total diameter) with a 3–6° taper angle formed by glass pulling and IR laser shaping, to create a 600 nm tip that facilitates insertion into the brain. A gold coating near the tip of the fiber acts as a reflector to prevent optical loss. Seven selected sites along the fiber serve as 25 × 25 μm² “windows” spaced 100 μm apart, formed by focused ion beam milling with a gallium ion (Ga⁺) beam. These windows allow light to escape at different depths, thus enabling stimulation of multiple brain regions with a single fiber. In one case, implantation of such a microstructured fiber into the striatum of transgenic mice expressing ChR2 allows for optogenetic stimulation and inhibition of neuronal activity with site selection achieved by adjusting the angle of the incident light onto the fiber.

An alternative approach involves silicon-based implantable nanophotonic probes (emitter pixels (E-pixels)) that exploit wavelength division multiplexing (WDM).¹⁵⁹ The probes are 90 μm wide and 18 μm thick, tapering to a width of 20 μm near wedge-shaped tips (radius of curvature, ~1 μm), supporting an optical stack with a 200-nm-thick layer of Si₃N₄ deposited by low-pressure chemical vapor deposition (LPCVD) encapsulated by layers of thermally grown SiO₂ (1.5 μm bottom, 1 μm top thickness). These devices employed *in vivo* allow patterned optogenetic stimulation in transgenic mice expressing ChR2.

Other strategies in nano/microstructured materials exploit ultrathin (6.45 μm thick), gallium nitride (GaN) based microscale inorganic light emitting diodes (μ-ILEDs) as the basis for flexible, penetrating probes that allow local delivery of light without the need for fiber optics and external light sources.¹⁶⁰ The fabrication process involves epitaxially grown GaN stacks on sapphire (Al₂O₃) wafers consisting of undoped GaN (3.8 μm thick), n-type GaN (3.2 μm thick), multiple quantum wells (MQW; 0.14 μm thick, peak wavelength 447 nm at 1 mA), and 0.2 μm of p-type GaN (0.2 μm thick) with a nickel (Ni)/Au bilayer (15 nm thick each) formed into an L-shaped current spreading layer with top (p-contact) and recessed bottom (n-contact) pads in the corners (25 × 25 μm² area; Cr/Au 15/300 nm thick). These light emitting diodes transfer to carrier Si wafers through laser liftoff (LLO) induced by passage of krypton fluoride (KrF) or yttrium aluminum garnet:neodymium (YAG:Nd) laser light through the sapphire growth wafer. Contact with stamps of PDMS (vertical pillars; 3 μm diameter, 1.2 μm height, 5 μm spacing) removes the devices from the carrier wafer for subsequent transfer printing onto other substrates of interest. These methods provide access to GaN μ-ILEDs with a range of lateral dimensions (1 × 1 mm² to 25 × 25 μm²) and thicknesses (micrometers or less) that are significantly smaller than those possible with wafer dicing techniques.

Different types of neural probes and interfaces can be used to deliver these microscale light sources into soft tissues. In one example, the probes involve micromachined silicon substrates that support GaN-based μ-ILEDs,¹⁶¹ as shown in Figure 7c for the case of four shanks (30 μm total thickness, 70 mm width, 5 mm length), each with three μ-ILEDs (10 × 15 μm² in emission area) and eight recording electrodes (Ti/Pt/Ir; 10/50/50 nm thick, 11 × 13 μm² area, 1 MΩ impedance at 1 kHz). This device can be deployed into the hippocampus regions of transgenic mice expressing ChR2 for optical stimulation and electrical recording. A disadvantage is that these probes are rigid and fragile.

An earlier report describes an alternative approach that uses cellular-scale μ-ILEDs integrated onto ultrathin polymeric injection microneedles (Figure 7d),¹⁶² in a four μ-ILED array that is part of a multifunctional system formed by transfer printing techniques.¹⁶⁰ The patterned polyester substrate (2.5 μm thick) includes interconnect traces of Cr/Au (15/300 nm thick) encapsulated with a layer of photodefinable epoxy (SU-8; 2 μm thick). Separately fabricated layers that include microscale inorganic photodetectors (μ-IPDs; 200 × 200 μm² lateral dimensions, 1.25 μm thick), thermal sensors, and electrophysiological sensors on 6-μm-thick polyester substrates bonded together in a stacked configuration using ultrathin films (~500 nm thick) of an epoxy polymer to yield complete systems (~20 μm total thickness). To enhance the bending rigidity for delivery into targeted regions of the brain, a thin bioresorbable adhesive layer (~100 nm thick) of 7 wt % purified silk fibroin joins the system onto a removable microneedle (Figure 7e) fabricated with photodefinable epoxy (SU-8; 250 μm thick). A wireless delivery and control system operates these components in transgenic mouse models expressing ChR2 to drive optogenetically modulated place preference in structured Y mazes, as a demonstration of programmed behavioral control over freely moving animals.

In related battery-powered wireless devices, 3D-printed optogenetic probes (3D-POPs)¹⁶³ formed using photopolymers support transfer-printed GaN-based μ-ILEDs (220 × 270 μm²

lateral dimensions) and PDMS/parylene-C (1/6 μm thick) encapsulation layers as thin, mechanically compliant optical interfaces (60 μm total thickness) with various rapidly customizable design layouts for scalable studies in various potential animal models. Additional wireless schemes to remove tethers that can potentially influence animal behavior use epitaxially released GaN-based μ -ILEDs (180 \times 125 μm^2 lateral dimensions, 7 μm thick) on flexible probes (copper (Cu)/PI/Cu; 18/25/18 μm thick) encapsulated with polyisobutylene/PDMS (7/30 μm thick) with battery-powered electronics for optical modulation of the behaviors of mice.¹⁶⁴

Despite the capabilities of such devices as tether-free optical neural interfaces, fully implantable, battery-free alternatives represent the most powerful platforms due to their efficient, lightweight, and miniaturized designs. One of the earliest examples exploits capacitive coupling between neighboring serpentine traces for RF power harvesting via miniaturized, stretchable antennas operating at 2.34 GHz.¹⁶⁵ When interfaced to the sciatic nerves and spinal cords of transgenic mice expressing ChR2, these interfaces allow activation of peripheral and spinal pain circuitry with 470 and 465 nm wavelength GaN μ -ILEDs, respectively. Other battery-free, fully implantable devices wirelessly operate through inductive coupling at 13.56 MHz, using near-field-communication (NFC) hardware schemes found in common electronic appliances.¹⁶⁶ This platform builds upon previous work^{167,168} for inductively coupled NFC-capable optoelectronic devices and incorporates Cu interconnects and active components on a PI substrate (75 μm thick) with a bilayer encapsulation of parylene/PDMS (5 $\mu\text{m}/0.5$ –300 μm thick) for a total maximum thickness of 1.3 mm. A key feature is an injectable microneedle (350 μm wide, \sim 80–130 μm thick) that incorporates a μ -ILED (470 nm emission wavelength) connected to circular Cu coil (eight turn traces of 60 μm width, 80 μm spaces, 18 μm thick, 9.8 mm total diameter) through a serpentine structure that allows freedom of motion. An *in vivo* implementation with this lightweight miniaturized optical modulator (9.8 mm diameter, 30 mg weight) coupled to the ventral tegmental area and nucleus accumbens of ChR2-expressing transgenic mice optically stimulates a neural circuit known to facilitate reward and positive reinforcement.

One of the most advanced technologies of this type includes support for intensity-regulated operation of multiple μ -ILEDs with real-time programmability.¹⁶⁹ These systems offer control over the optical intensity, pulse duration, and stimulation frequency as useful tools for optogenetic studies in freely moving animals. Devices in the form of head-mounted (HM) and back-mounted (BM) designs with multiple, separately controlled probes, allows optogenetic control of individual and social behaviors in groups of mice, with demonstrations in the formation and elimination of bonding behaviors by synchronized and desynchronized stimulation.¹⁷⁰

2.2.2. Stretchable and Compliant Materials. As with electronic/electrochemical interfaces, low-modulus materials for optical interfaces can reduce mechanically induced damage to surrounding soft neural tissues (\sim 1–10 kPa).¹⁷¹ Compliant polymers for flexible optical fibers represent one set of examples. Thermal drawing techniques can be used to create multi-material, flexible fibers of this general type. Here, a structured cylindrical preform serves as a precursor to the final desired fiber. Heating to roughly 50–100 $^{\circ}\text{C}$ above the glass transition temperature (T_g) of the constituent materials in a furnace softens them and causes necking to allow for laminar flow as the

preform is pulled with a weight, resulting in a continuous fiber without defects or breaks.¹⁷² One report uses a cyclic olefin copolymer elastomer (COCE; refractive index (n) = 1.51, modulus = 34 MPa, T_g = 84 $^{\circ}\text{C}$) coated with a flexible, biocompatible PDMS encapsulation layer (n = 1.47, 5 μm thick) that reduces direct contact of the fiber with tissue while allowing bending and stretching deformations during deployment and subsequent use (Figure 7f).¹⁷³ The thermal drawing process for these highly stretchable (up to 230% strain) fibers (105–135 μm total diameter) reduces the initial fiber dimensions by up to 200 times while producing hundreds of meters of fiber in a single draw. Demonstrations that use transgenic mice expressing ChR2 support the potential for use in neuroscience studies. Similar processes also provide options for including tin (Sn) microwires (4.75 μm diameter) encapsulated in poly(etherimide) (PEI; 80 μm diameter). The surfaces of the fibers can be functionalized with primary amines to promote robust covalent bonding with alginate (Alg) via carbodiimide chemistry, such that dip-coating into an Alg–polyacrylamide (PAAm) hydrogel pregel solution forms a 25- μm -thick hydrogel layer. Implantation into the ventral hippocampus of mice enables optogenetic modulation and electrophysiological monitoring.¹⁷¹

Low-modulus (\sim 65 kPa) and highly extensible (over 400%) hydrogels can also be used to form optical fibers (125 μm diameter, n = 1.35), using Alg and PAAm. These fibers result from polymerization of the Alg–PAAm precursor in a silicone tube (300 μm diameter; Figure 7g–i).¹⁷⁴ Optogenetic studies with mice indicate improved tissue responses and neuronal survival rates compared to those observed with conventional silica optical fibers.¹⁷⁵ Different classes of soft materials can be combined, as in the example of polymer-based fiber probes that embed into soft Alg–PAAm hydrogel matrixes (5.5 kPa shear modulus) to yield highly flexible fibers (7 N/m bending stiffness; 106 μm diameter) that incorporate a polycarbonate (PC) core and COC cladding.

2.2.3. Bioresorbable Materials. As described previously, bioresorbable materials are attractive for neural interfaces due to their ability to act as temporary implants. Transparent bioresorbable materials such as silk fibroin,¹⁷⁶ citrate-based polymeric elastomers,¹⁷⁷ PLLA,¹⁷⁸ and PLGA¹⁷⁹ are attractive as materials for optical waveguides and fibers for the purpose of neural modulation or monitoring based on mechanisms described previously.¹¹⁸ These materials either contain or form ester bonds that are cleavable by hydrolysis as the basis for their degradability in biofluids. For silk fibroin, the peptide bonds themselves are water-soluble via hydrolysis. One example uses PLGA optical fibers (150 μm diameter, n = 1.5) with thin bioresorbable encapsulation layers of SiO₂ (50 nm thick, n = 1.45) to augment light confinement for monitoring of neural activity (Figure 7j).¹⁷⁹ The optical transparency of the PLGA fiber gradually decreases when it is exposed to physiological conditions, and the fiber disappears without a trace as it dissolves into lactide and glycolide, species that subsequently metabolize and clear from the body. Additional bioresorbable optical components include tricolor photodetectors based on SiNMs (1.5 μm thick) with n- and p-doped regions (10^{18} cm⁻³ doping concentrations) and aligned optical filters based on alternating stacks of SiO_x (54 nm thick) and SiN_y (85 nm thick). SiO_x and SiN_y dissolve by hydrolysis according to SiO₂ + H₂O \rightarrow Si(OH)₄ and Si₃N₄ + 6H₂O \rightarrow 3SiO₂ + 4NH₃ respectively.¹¹⁸

In related demonstrations, strands of PLLA (n = 1.47) formed by thermal drawing yield highly flexible (1.5×10^4 N/m bending stiffness) and transparent (over 90% at visible light) types of

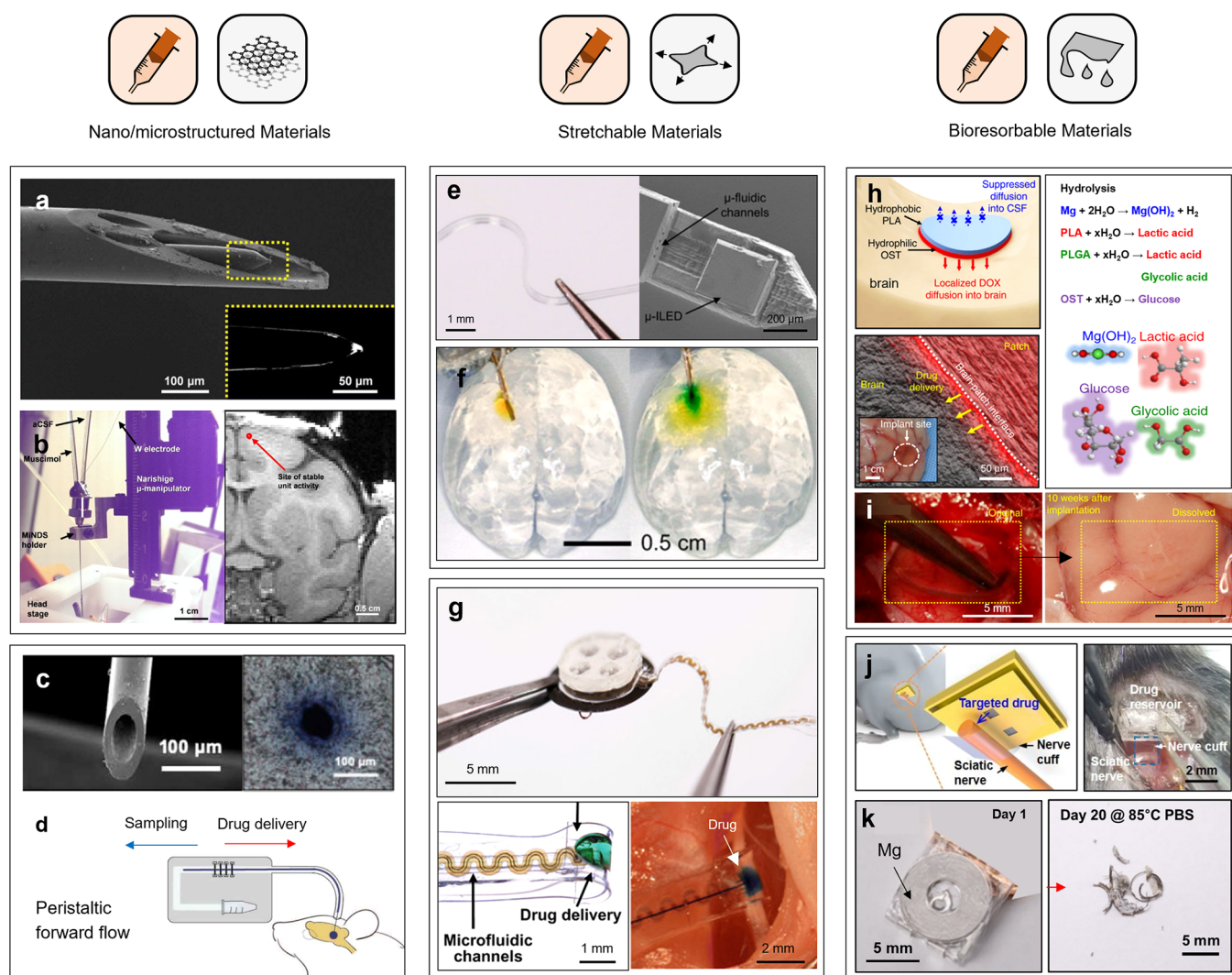


Figure 8. Pharmacological interfaces. (a–d) Nano/microstructured materials. (a) SEM image of a capillary with a W electrode and two BS channels. Magnified view of the tip (right inset). (b) Experimental setup integrated with a head stage for a nonhuman primate (left) and magnetic resonance image (MRI) indicating the location of the capillary for infusion and recording (right).¹⁹³ Reproduced with permission from ref 193. Copyright 2018 American Association for the Advancement of Science. (c) SEM image of a BS capillary (left) to collect samples of ISF and *ex vivo* histological tissue slice derived from a rodent brain showing infusion of trypan blue (right).¹⁹² Reproduced with permission from ref 192. Copyright 2020 American Association for the Advancement of Science. (d) Schematic illustration of a membrane-free biochemical sampling platform designed to interface with the rodent brain.¹⁹² Reproduced with permission from ref 192. Copyright 2020 American Association for the Advancement of Science. (e–g) Stretchable materials. (e) Optical (left) and SEM (right) images of a soft, compliant probe with microfluidic channels. (f) First (yellow) and second (green) release of drugs into a brain phantom, demonstrating the ability to refill and reuse the system.¹⁹⁶ Reproduced with permission from ref 196. Copyright 2019 National Academy of Sciences. (g) Optical image of an optofluidic cuff system for wireless optogenetic and pharmacological neuromodulation of peripheral nerves (top). Magnified image of microfluidic drug delivery (bottom left) and demonstration of integration onto the sciatic nerve (bottom right).¹⁹⁷ Reproduced with permission from ref 197. Copyright 2019 American Association for the Advancement of Science. (h–k) Bioresorbable materials. (h) Illustration of a bifacial, BEP conformally adhered on the brain surface (left; top) and diffusion of drug from the BEP (left; bottom). Constituent materials of the BEP and their hydrolysis products associated with bioresorbability (right). (i) Surgery for intracranial BEP implantation (left) and at 10 weeks after implantation (right).¹²⁴ Reproduced with permission from ref 124. Copyright 2019 Springer Nature. (j) Illustration of a wirelessly controlled drug delivery system built with Mg and polyanhydride for pharmacological release at a targeted site (left) and a photograph showing the implantation procedure of the system (right). (k) Sequential images of dissolution of an entire system immersed in PBS.¹⁹⁸ Reproduced with permission from ref 198. Copyright 2020 American Association for the Advancement of Science.

optical fibers (200 μm diameter). During hydrolysis, cleavage of ester bonds yields lactic acid, which is abundant in the body and is cleared by the tricarboxylic acid cycle.^{118,180} In studies that involve monitoring of neural activity by measuring fluorescence in the brain of a rodent model, these implanted PLLA fibers completely resorb after 60 days (Figure 7k).¹⁷⁸

In addition to thermal drawing, 3D printing techniques can form relevant bioresorbable optical structures. In one case, extrusion based 3D printing yields optical waveguides of

poly(D,L-lactide-co-caprolactone) (PLA-co-PCL; $n = 1.46$, 300 μm diameter)¹⁸¹ that support 10 and 20 cm penetration depths for light with wavelengths of 405 and 520 nm, respectively. An *in vitro* experiment demonstrates the ability of such waveguides to deliver 405 nm light within porcine tissue (8 cm thick).

Recent work also illustrates the possibility for bioresorbable LEDs, as alternatives to the nonresorbable light sources described previously.¹⁸² Specifically, n-type ZnO(001) films (200 nm thick) grown on Si substrates through pulsed laser

deposition (PLD) form the active semiconducting and light emitting components of the devices. The ZnO directly degrades into water-soluble Zn^{2+} through hydrolysis ($\text{ZnO} + \text{H}_2\text{O} \rightarrow \text{Zn}(\text{OH})_2$ or $\text{ZnO} + \text{H}_2\text{O} \rightarrow \text{Zn}^{2+} + 2\text{OH}^-$).¹¹⁸ Thin (15 nm thick) insulating layers of SiO_2 deposited onto the ZnO expose a $20 \times 20 \mu\text{m}^2$ active area. Deposition of a transparent Mo electrode on one side (8 nm thick) and a W electrode on the other (100 nm thick) yields complete devices. Interference effects associated with SiNMs form the basis of optical filters with thicknesses of 85, 62, and 42 nm to allow for selective emission of red, green, and blue light from these LEDs, respectively. This type of bioresorbable device may serve as the basis for temporary optical interface modulators for various experiments that use optogenetic methods or genetically encoded indicators.

2.3. Pharmacological Techniques

Pharmacological techniques represent some of the oldest approaches to neuromodulation, with applications that range from controlling seizures, pain responses, and depression to inducing deep brain stimulation.^{183,184} These methods enhance or moderate activities at targeted chemical junctions in endogenous systems through oral, intravenous, or intramuscular methods. Traditional pharmacologic approaches depend on systemic drug administration, resulting in broad drug distribution through the body with consequently increased risk for undesired outcomes and side effects such as off-target cellular or tissue responses.

Platforms capable of targeting subpopulations of neural circuits within sub cubic millimeter volumes are of interest for spatially precise pharmacological delivery, using small, controlled dosing strategies.¹⁸⁵ To meet these needs, recent work focuses on the development of miniaturized, microfluidic neural probes^{186,187} and implantable drug chambers.¹⁸⁸ When combined with wirelessly programmable control modules, such systems have strong potential not only as neural interfaces but also as advanced treatment protocols for hormonal imbalances, diabetic conditions, cancers, and others.^{189,190}

A complementary use of related technologies focuses on the collection of brain interstitial fluid (ISF) for neurochemical sampling and analysis to assess neurological function. Microdialysis can be implemented with microfluidic channels for analysis of composition, concentration, and distribution of neurochemicals.^{191,192} The following approaches highlight progress in these injectable or implantable types of devices (i.e., microfluidic probes or miniaturized drug reservoirs) with an emphasis on the essential roles of the categories of materials outlined in previous sections.

2.3.1. Nano/Microstructured Materials. Nano/microprobes enable local intracerebral drug injection with minimized invasiveness ($200 \mu\text{m}$ diameter). One such platform enables delivery into the deep brain for modulating behavioral and acute electrophysiological effects in small (rodent) and large (nonhuman primate) animal models, with capabilities in simultaneous recording of EEG activity through a W electrode ($75 \mu\text{m}$ diameter).¹⁹³ Here, a stainless steel (SS) needle ($200 \mu\text{m}$ outer diameter (o.d.), $150 \mu\text{m}$ inner diameter (i.d.)), integrated with two borosilicate (BS) channels ($20 \mu\text{m}$ i.d.), and a W electrode ($75 \mu\text{m}$ diameter) support pharmacological drug delivery and neural activity recording, respectively (Figure 8a,b). As implanted into the brain, this system allows remotely controlled, on-demand drug infusion (muscimol, $100 \text{ nL}/\text{min}$) to the substantia nigra through an externally connected wireless pump,

causing Parkinsonian behavior (e.g., preferential ipsilateral rotation) in freely behaving, awake rats. Eliminating the needle (PI shell $160 \mu\text{m}$ o.d., $130 \mu\text{m}$ i.d., two BS channels inside), reduces the thickness and increases the flexibility (critical buckling loads (P_{cr}) of SS = 1.785 N , P_{cr} of PI = 31.2 mN), as demonstrated by dosing drugs into brain microstructures to modulate behavioral effects in a volume-dependent manner.¹⁹⁴ This type of microprobe can be independently inserted into areas such as the substantia nigra, with multiple fluidic lumens in a submillimeter footprint, thereby controlling the dynamics of deep brain infusions as well as the distinct diffusion kinetics of three different chemicals: unbound radioactive copper-64, ^{64}Cu functionalized with polyethylene glycol (PEG- ^{64}Cu), and 2-deoxy-2-(^{18}F)fluoro-D-glucose (FDG). A similar platform based on a BS capillary ($60 \mu\text{m}$ o.d., $20 \mu\text{m}$ i.d.) with an asymmetric tip geometry improves the accuracy and reliability of implantation by incorporating steering capabilities.¹⁹⁵ The polished capillary tip offers a large bevel angle (50° , 30° in general for effortless insertion¹⁹³), to yield a net lateral force on the needle that is proportional to the sine of this angle. This force produces a curved trajectory upon insertion into soft media, allowing for guided insertion to specific locations without the need for guide tubes.

Emerging work in microfluidic neural interfaces exploits microdialysis techniques for neurochemical sampling as well as drug delivery into specific brain regions, while minimizing large-scale tissue damage and immune responses. Recently reported nanofluidic platforms with extremely fine probes can reduce extraction losses during sampling from brain tissues.¹⁹² In one case the probe consists of a borosilicate capillary ($80 \mu\text{m}$ o.d., $50 \mu\text{m}$ i.d.) directly inserted into a styrene ethylene butylene styrene (SEBS) pumping tube (1 mm o.d., $100 \mu\text{m}$ i.d.; Figure 8c), driving bidirectional fluid flow in both infusion (single stroke volumes, $<3 \text{ nL}$) and sampling modes ($<100 \text{ nL}/\text{min}$; Figure 8d). This platform samples electroneutral neurochemicals with minimal dead volume ($<30 \text{ nL}$).

2.3.2. Stretchable and Compliant Materials. Sharp and stiff platforms such as those described in section 2.3.1 provide spatially accurate delivery for drugs to the targeting areas, but with disadvantages (i.e., chronic inflammation, neuronal necrosis) similar to those highlighted in discussions of electrical/electrochemical and optical interfaces due to the modulus mismatch with surrounding tissues. Compliant materials as microfluidic interfaces and stretchable pharmacological vehicles as optofluidic platforms are relevant in this context.

Figure 8e shows the design of a battery-free, lightweight (0.29 g) optofluidic device that incorporates a thin ($\sim 100 \mu\text{m}$ thick) and soft ($\sim 3 \text{ MPa}$ in modulus) microfluidic probe fabricated by soft lithography in the form of two thin, narrow pieces of PDMS that define a set of microchannels ($\sim 30 \times 30 \mu\text{m}^2$ cross-sectional area).¹⁹⁶ The system consists of a micropumping chamber with interdigitated electrodes (Au/Cu; $\sim 50 \mu\text{m}$ width, $200 \text{ nm}/18 \mu\text{m}$ thick, $\sim 50 \mu\text{m}$ spacing) and a drug reservoir, both milled from a block of cyclic olefin polymer (1 mm thick), selected for low water absorption ($<0.01\%$), water vapor permeability ($0.045 \text{ g}\cdot\text{mm}/\text{m}^2\cdot\text{day}$), and resistance to various solvents. An expandable membrane of polystyrene-*block*-polybutadiene-*block*-polystyrene (SBS; $\sim 150 \mu\text{m}$ thick) with a combination of soft mechanical characteristics ($\sim 13 \text{ MPa}$ modulus) and effective barrier properties (water permeability; $8.52 \times 10^{-8} \text{ g}\cdot\text{m}/\text{m}^2\cdot\text{h}\cdot\text{Pa}$) locates between the reservoir (top) and the electrochemical micropump (bottom). Pressure induced by

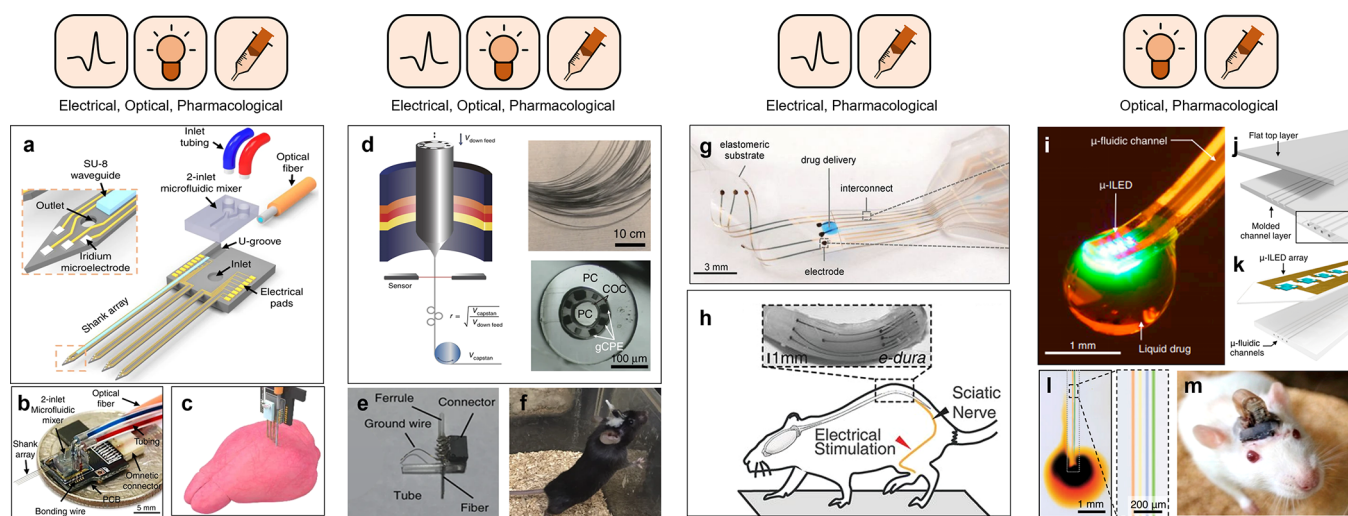


Figure 9. Multimodal interfaces. (a–c) Electrical sensing and optofluidic modulation system. (a) Schematic diagram and (b) optical image of the components including a shank array, microfluidic mixer and inlet, and optical fiber before device assembly. The inset shows the probe tip with outlet, waveguide, and microelectrodes. (c) Schematic image of a multifunctional multishank MEMS neural probe inserted into the hippocampus of mice.²⁰⁰ Reproduced with permission from ref 200. Copyright 2019 Springer Nature. (d–f) Flexible electrical sensing and optical and pharmacological modulating interface. (d) Illustration of the fiber drawing process (left). Optical image of a bundle of fiber (top right). Cross-sectional microscopic image of the multimodal fiber consisting of graphite as electrodes, polycarbonate (PC) as a waveguide, and microchannels (bottom right).²⁰¹ Reproduced with permission from ref 201. Copyright 2017 Springer Nature. (e) Photograph of a multimodal fiber probe fitted with an optical ferrule, electrical connector, and an injection tube. (f) Mouse implanted with a multifunctional probe.²⁰² Reproduced with permission from ref 202. Copyright 2015 Springer Nature. (g, h) Soft, electrical sensing and pharmacological modulating interface. (g) Optical image of an e-dura implant consisting of elastomeric PDMS substrate, microfluidic channel for drug delivery, Au film as interconnect, and Pt microparticle–PDMS composite electrodes. (h) Schematic illustration and optical image of a rat with e-dura on the spinal cord.¹¹³ Reproduced with permission from ref 113. Copyright 2015 American Association for the Advancement of Science. (i–m) Wireless optofluidic system. (i) Soft, compliant device integrated with multiple μ -ILEDs and μ -fluidic channels. (j) Schematic diagram of the assembly of a soft microfluidic probe consisting of thin, molded (bottom), and unmolded (top) layers of PDMS and resultant four separately addressable microfluidic channels. (k) Schematic diagram of the integration of a soft microfluidic probe with a flexible array of μ -ILEDs and metal interconnect traces on a film of PET. (l) Optical images that show delivery of different liquids (aqueous solutions with red, yellow, blue, and green dyes) through four individual microfluidic channels with magnified view. (m) Images of a wireless optofluidic device implanted in a freely behaving rat.²⁰³ Reproduced with permission from ref 203. Copyright 2015 Elsevier.

remotely controlled electrolysis (i.e., release of oxygen and hydrogen gas) deforms the membrane, thereby driving the flow of pharmacological agents out of the reservoir to the targeted area through the microchannel. Multiple refilling ports on the sides of the reservoirs allow sequential releasing events of drugs (Figure 8f) such as the μ (mu) opioid receptor agonist (D-Ala²,NMe-Phe⁴,Gly-ol⁵)-enkephalin (DAMGO) and the N-methyl-D-aspartate (NMDA) receptor antagonist (2R)-amino-5-phosphonovaleric acid (APS).

A related system involves a stretchable neural cuff with microfluidic channels and associated battery-free operated optoelectronics as a combined optical and pharmacological interface (Figure 8g).¹⁹⁷ The microchannels (~ 3 MPa modulus, 200 μm thick, $\sim 30 \times 30 \mu\text{m}^2$ cross-sectional area) connect to drug reservoirs on one side and terminate at an outlet integrated into a cuff structure on the other. The system minimizes effects on nerve health through materials that have mechanical properties comparable to those of peripheral nerve tissue (sciatic nerve modulus, ~ 7 MPa). The serpentine shape of the PI filament that connects the cuff to the reservoirs enables mechanical stretching (~ 15 – 20%) to accommodate natural tissue movements. These soft and stretchable devices remain in position without signs of damage to the nerves for 10 weeks post implantation in freely moving animals.

2.3.3. Bioresorbable Materials. Progress in bioresorbable platforms creates opportunities in the development of on-demand release systems that disappear by resorption after depletion of the drug reservoirs. Advanced platforms allow for

programmable, wireless control. In one case, a flexible, tacky, and bioresorbable electronic patch (BEP) integrated with wireless electronics enables controlled intracranial drug delivery to brain tumors through mild thermic actuation.¹²⁴ This drug loaded BEP uses fully hydrolytic materials such as PLA (encapsulant), PLGA (dielectric layer), Mg (electrode) and oxidized starch (OST; reservoir) stacked into three functional layers to form a wireless temperature sensor (top), a wireless heater (middle), and a drug reservoir (bottom) for doxorubicin (Figure 8h). Application of an RF field to the heater wirelessly initiates drug release from the reservoir, thereby accelerating intercellular drug diffusion and enhancing the drug penetration depth. The flexibility of the BEP enables conformal adhesion to the curved surface of the brain, minimizing neurological side effects caused by rigid intracranial implants.¹⁷¹ In addition, the bifacial design of the hydrophilic bottom (i.e., OST) and hydrophobic top (i.e., PLA) regions provides strong adhesion between the BEP and brain surface due to the imine conjugation resulting in low drug leakage to other regions and highly efficient drug delivery. Implantation of the device in a canine brain demonstrates dissolution without any debris or clinical side effects within 10 weeks (Figure 8i), corresponding to the entire duration of *in vivo* drug release.

A recent study describes an advanced system that consists of a wirelessly programmable bioresorbable device for controlled release across multiple, independent drug chambers.¹⁹⁸ The platform consists of a UV-curable, bioresorbable polyhydride (PA) containment vessel for one or multiple different types of

drugs, two Mg electrodes assembled within the PA housing as valves that can be opened through electrochemical crevice corrosion, and a wireless power harvester based on a Mg coil and a Si rectifying diode (Figure 8j). The delivery process initiates through an overpotential (bias) from the harvester that generates a bias between the electrodes (anode (gate) and cathode) and subsequent irreversible Faradaic reactions in the anode during exposure to surrounding biofluids. This reaction (i.e., $\text{Mg} \rightarrow \text{Mg}^{2+} + 2\text{e}^-$) opens the valves and results in the release of drugs (e.g., lidocaine, insulin) from the reservoirs (Figure 8k). Exploiting this scheme (i.e., crevice corrosion) using metal gates with various shapes and sizes allows the delivery of effective doses to target tissues with desired kinetics. In one demonstration as a neural interface, programmed release allows for directional and localized pharmacological delivery of lidocaine to the sciatic nerve for local pain relief.¹⁹⁹ The entire system disappears completely and naturally in the body without residues through hydrolysis. As an alternative to the PA-based containment vessel, a similar type of bioresorbable electronic implant uses lipid membranes as a drug reservoir. The lipid membranes embedded with multiple types of drugs (parathyroid hormone (1–34), dextran, and doxorubicin) exhibit negligible leakage in the off state and release drugs on demand through externally triggered thermal actuation via Joule heating of 15- μm -thick Mo-based serpentine resistors over the transition temperature of the lipid membranes (41 °C).⁶³

2.4. Multimodal Interfaces

The various materials and structures outlined in the previous sections can be combined into multimodal neural interfaces. For instance, the multishank microelectromechanical system (MEMS) probe in Figure 9a–c represents an example that supports optical and pharmacological modulation with electrophysiological sensing. The system integrates an optical waveguide structure fabricated by using photodefinable epoxy (40 \times 15 μm^2 cross-sectional area, $n = 1.54$) and three microfluidic channels (10 \times 12 μm^2 cross-sectional area), along with 32 Ir microelectrodes (four shanks, eight electrodes each; average impedance, 0.665 M Ω at 1 kHz). As an illustration, the probe can implant into transgenic mouse models expressing ChR2 in a recognized trisynaptic circuit in the hippocampus known as the CA3–CA1 region to investigate the functional connectivity in the intact brain. Blue light (473 nm, 1 Hz with a 50% duty cycle, 167 mW/mm² with a total power of 100 μW) delivered through the optical waveguide modulates CA3 neurons, while simultaneous recordings of neural signals from the 32 electrodes reveal optically evoked CA3 and CA1 spikes synchronized with the CA3 signals. Chemical modulation includes the delivery of the α -amino-3-hydroxy-5-methyl-4-isoxazolepropionic acid (AMPA) receptor antagonist cyanquinoxaline (CNQX) and the NMDA receptor antagonist AP5 through the microchannels to CA1 neurons. The antagonists block the synaptic transmission even as CA3 neurons are optically stimulated, thereby demonstrating suppressed neural activity and the system's multimodality.²⁰⁰

As examples of mechanically flexible multimodal neural interfaces, extensions of the previously described thermal drawing process can create complex, multimaterial fibers for monitoring electrical activity and for simultaneous optical and pharmacological modulation.^{201,202} In one case, PC ($n = 1.586$, glass transition temperature (T_g) = 150 °C), COC ($n = 1.53$, T_g = 158 °C), and a customized graphite composite comprised of conductive polyethylene (CPE) and 5% graphite (sheet

resistance = 0.8 k Ω /sq, melting temperature (T_m) \sim 123 °C) combine into a preform to yield fibers after drawing (Figure 9d–f). The resultant flexible (bending stiffness = 76.1–83.5 N/m) fibers incorporate low-impedance electrodes (0.6 M Ω impedance at 1 kHz, 20–25 μm size), a microfluidic channel (\sim 15 μm diameter), and an optical waveguide (\sim 68 μm diameter). Implantation into the medial prefrontal cortex (mPFC) of mouse models allows monitoring of electrical activity and controlled pharmacological and optogenetic modulation of the brains of mice. The integrated microfluidic channels deliver an adeno-associated virus (AAV, serotype 5) carrying the gene for ChR2 fused to the enhanced yellow fluorescent protein (eYFP) under the excitatory neuronal promoter calmodulin kinase II α -subunit (AAV5-CaMKII α ::ChR2-eYFP), resulting in robust ChR2 expression in the mPFC during optical stimulation (473 nm). Eleven days after virus injection, electrophysiological signals recorded following optogenetic modulation (10 Hz, 8.6 mW/mm², 5 ms pulse width) indicate that the amplitude and expression periods of optically evoked signals increase at larger optical powers.²⁰¹

A soft and stretchable platform for sensing and modulating, known as electronic dura mater (e-dura, Figure 9g,h) as introduced previously, uses a silicone substrate (PDMS, 120 μm thick, 3 MPa), Pt–PDMS composite electrodes (300 μm diameter, 5 k Ω at 1 kHz), stretchable gold interconnects (35 nm thick), and microfluidic channels (100 \times 50 μm^2 cross-sectional area) as an electrical and pharmacological interface to the brains and spinal cords of rodents. The system has an effective modulus of \sim 1.2 MPa and an elastic response to strain of up to 45%. A 3 \times 3 e-dura electrode array exhibits its electrical sensing capability by optically monitoring evoked electrical activity from the motor cortex of mice expressing ChR2. E-dura chronically implanted over spinal tissues in mice with electrical and pharmacological modulation functions restore locomotion after spinal cord injury. Injecting serotonergic replacement therapy (5HT_{1A/7} and 5HT₂ agonists) and applying continuous electrical stimulation on the lateral aspect of L2 and S1 segments (40 Hz, 0.2 ms, 50–150 μA) enables paralyzed rats to walk.¹¹³

In addition to these tethered, flexible and stretchable modulating systems, wireless and fully implantable neural interfaces can be realized, for unconstrained freedom of movement in animal models. Minimizing the influence of devices on motion in animal studies can enhance experimental reproducibility and reduce unintentional interactions with surrounding environments. Figure 9i–m outlines an *in vivo* implementation of a wireless optofluidic modulation system of this type. Here, ultrathin (\sim 50 μm thick) and mechanically soft (\sim 1 MPa modulus; 13–18 N/m bending stiffness) PDMS structures define multiple channels as the basis of an implantable neural probe integrated with a wireless communication system in a compact, head-mounted device. A key feature is a soft microfluidic structure formed with thin pieces of PDMS bonded together to form a set of four channels (10 \times 10 μm^2 cross-sectional area; Figure 9j). Each channel connects to a separate reservoir, and drug delivery occurs by wirelessly activating microscale Joule heating elements (serpentine traces of Au 250 nm thick, 125 Ω in resistance) up to 80 °C, resulting in pressure changes in the reservoir induced by rapid volume expansion of expandable hollow microspheres (Expancel 980 DU 120) that encapsulate hydrocarbon gas. This optoelectronic technology integrates μ -ILEDs (100 \times 100 μm^2 dimensions and 6.54 μm thick) to provide spatially and temporally precise delivery of light adjacent to the outlets of the microfluidic channels. The

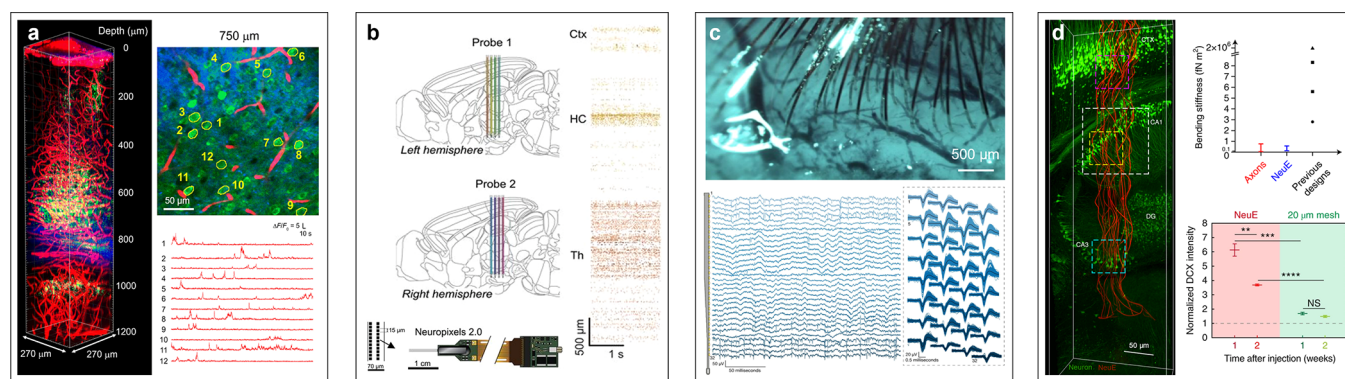


Figure 10. Examples of 3D neural interfaces to the brain. (a) Multicolor three-photon fluorescence imaging deep in the mouse brain. GCaMP6s-labeled neurons (green), Texas Red labeled blood vessels (red), and THG (blue) upon 1340 nm excitation. (left) Z-stack images down to 1200 μm from the brain surface. The images correspond to locations into the depth at 4 μm steps. (top right) Activity recording site at 750 μm beneath the dura. (bottom right) Spontaneous brain activity traces recorded in an awake mouse from the labeled neurons.²⁰⁹ Reproduced with permission from ref 209. Copyright 2021 American Association for the Advancement of Science. (b) Miniaturized high-density probe with 10 240 recording sites. (top) Schematic illustration of two implanted Neuropixel 2.0 probes at the right and left hemispheres of mouse brain and representative raster plots showing spikes recorded on 6144 of the 10 240 sites at the depth along the probe. (bottom) Schematic illustration of Neuropixel 2.0 probe.²¹² Reproduced with permission from ref 212. Copyright 2021 American Association for the Advancement of Science. (c) Robot assisted brain–machine interface with thousands of channels. (top) Optical image of the cortical surface with implanted threads. (bottom left) Representative neural signals from a single channel and (bottom right) superimposed waveforms from a rat.²¹³ From ref 213. CC BY 4.0. (d) Bioinspired neuronlike electronics (NeuE). (left) Fluorescence image of a neuron (green) and polymer layer (red) 6 weeks postimplantation into a mouse. (top right) Bending stiffness of axons, NeuE and previously reported mesh electronics. (bottom right) Normalized DCX+ levels indicative of newborn neuron intensity at 0–20 μm near the NeuE or 20 μm mesh (normalized against baseline values remote to the probe).²¹⁴ Reproduced with permission from ref 214. Copyright 2019 Springer Nature.

system offers stable, long-term operation in various behavioral experiments when implanted into rats.²⁰³

Another wirelessly operated multimodal interface includes optogenetic modulation as its basic function, but it can be configured with an electrochemical sensor²⁰⁴ or photodiode²⁰⁵ as additional functionalities for detecting optically evoked catecholamines or monitoring fluorescence, respectively. When implanted into freely moving transgenic mice expressing ChR2, these devices offer various multimodal functions. A PEDOT:PSS-based amperometric electrochemical sensor monitors dopamine fluctuations induced by optical modulation (detection sensitivity of $\sim 0.06 \text{ nA}/\mu\text{M}$) with a constant forward bias of 0.6 V, while the reference electrode (RE) and the counter electrode (CE) use standard Ag/AgCl wires and SS screws, respectively.²⁰⁴ The interface incorporates μ -ILEDs (470 nm wavelength) matched to a fluorescence excitation source compatible with many GECIs and a gallium arsenide (GaAs) based μ -IPD with a narrow band molecular absorber based optical filter (photon absorption from 465 to 490 nm). The system captures Ca^{2+} transients corresponding to dynamic neural activity in deep brain structures in freely moving animals expressing GCaMP6 (maximum fluorescence emission wavelength 520 nm).²⁰⁵ This device is battery-powered and weighs $\sim 1.8 \text{ g}$.²⁰³ Eliminating the battery and related components can reduce the total weight of the system to a small fraction of a gram ($\sim 0.2 \text{ g}$) to thereby decrease the behavioral constraints associated with the weight of the battery.¹⁹⁶ As advanced wireless systems, magnetic resonant coupling schemes at 13.56 MHz described previously provide wireless sources of power for pharmacological and optogenetic modulation *in vivo*.

The most sophisticated demonstrations of these ideas in lightweight, wireless systems are in fully implantable closed-loop devices that control organ function. A recent report describes a multimodal technology that monitors the filling of the bladder with a strain gauge and optically modulates its behavior through optogenetic mechanisms as needed to eliminate overactivity.⁶⁴

This system uses a thin layer of silicone elastomer doped with carbon black (15 μm thick, 0.3 $\text{M}\Omega$ in impedance) as a resistive strain gauge to identify signs of abnormal activity by monitoring the time dependent changes in the radius of the bladder of a mouse model. Upon detection of abnormal voiding events, the system initiates optical stimulation using green μ -ILEDs (540 nm wavelength) to modulate transgenic bladder cells via optogenetics to restore normal function. Many examples of closed-loop control based on electrophysiological sensing include deep brain stimulation (DBS) with feedback that relies on measurements of electrical activity of the brain.²¹

3. THREE-DIMENSIONAL NEURAL INTERFACES

One of the most active frontier areas in neural interfaces focuses on exploiting the advanced materials and approaches described previously in systems that have 3D architectures. The results offer the potential for functional integration over volumetric spaces, as opposed to surfaces, via sheets or cylindrical cuffs, or at isolated depths, via penetrating probes. Two-photon^{206,207} or three-photon^{208,209} optical stimulation and imaging techniques are powerful options in this context, as illustrated in the 3D image of a mouse brain with GCaMP6s-stained neurons, blood vessels (Texas Red), and third harmonic generation (THG; representing red blood cells and myelin) upon 1340 nm excitation, in Figure 10a. These optical setups can probe and modulate neural activity at desired positions beneath the dura *in vivo*, down to 1200 μm from the brain surface.²⁰⁹ Such methods are important, but they cannot provide the full range of electrical, electrochemical, optical, and microfluidic options provided by interfaces that use materials and physical structures.

Certain schemes for 3D integration use scaled versions of penetrating probes, like those introduced in previous sections, such as bundled arrays of microwire-based electrode probes connected to CMOS electronics.^{210,211} For example, the latest multisite silicon probes (Figure 10b; Neuropixels 2.0 probe)

Methods

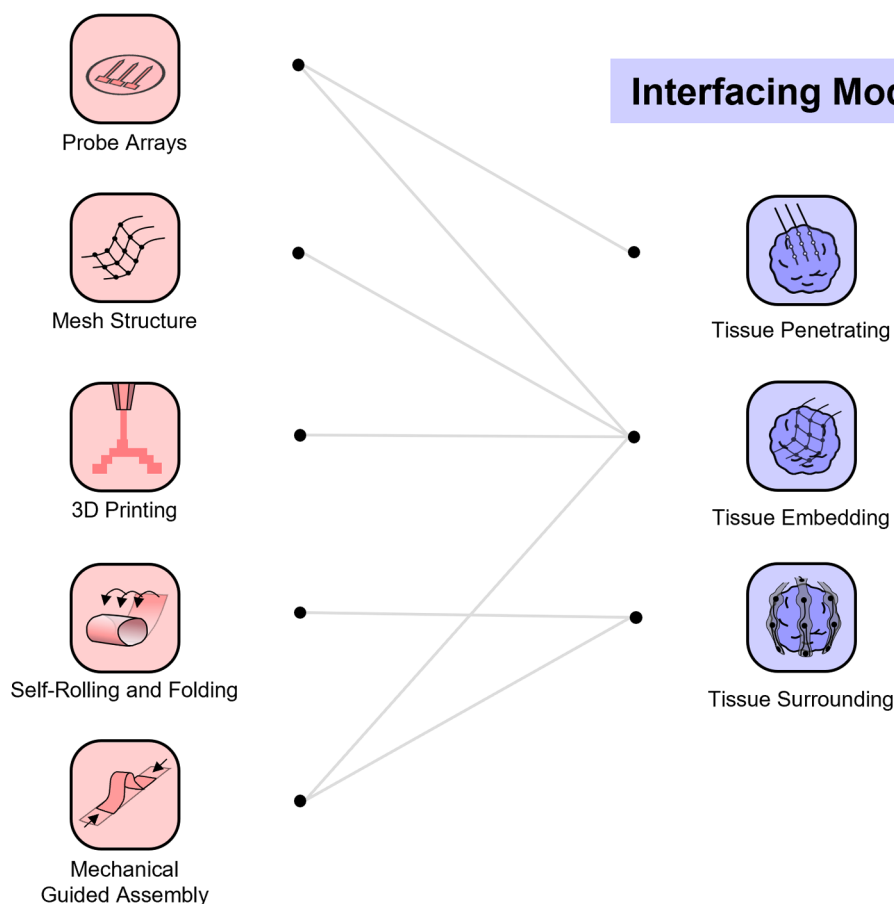


Figure 11. Three-dimensional assembly methods and associated neural interfacing modes. Network diagram highlighting the relationship between various assembly methods and associated interfacing modes. Probe arrays, mesh structure, 3D printing, self-rolled or self-folded, and mechanically guided assembly serve as diverse approaches to build sensing and modulation interfaces in tissue penetrating, embedding, and surrounding modes of interfacing to neural tissues.

offer 1280 recording sites (TiN electrodes, each $12 \times 12 \mu\text{m}^2$ area; impedance, $148 \text{ k}\Omega$ at 1 kHz) distributed along the length of a single probe, with supporting complementary metal oxide semiconductor (CMOS) electronics and with long-term (8 weeks), stable operation *in vivo*.²¹² Simultaneous use of multiple probes of these types begins to achieve some level of 3D integration. In one example, a linearized collection of four probes mounted on a single planar substrate (each 10 mm long, $70 \times 24 \mu\text{m}^2$ cross-sectional area) can, with a miniaturized, lightweight (1.1 g) headstage, record from over 5000 sites in freely moving animals. A pair of such systems allows simultaneous sampling of activity from the right and left hemispheres of the brains of mouse models, with 5120 sites from each hemisphere, for a total of 10 240.

Related approaches exploit arrays of passive electrodes on flexible, filamentary polymeric probes ($4\text{--}6 \mu\text{m}$ thick; 20 mm long; 32 electrodes per thread), as illustrated in Figure 10c. An automated surgical robot inserts each probe into locations that avoid damage to blood vessels, at scales that allow monitoring from up to 3000 channels with Au electrodes coated with PEDOT:PSS ($14 \times 25 \mu\text{m}^2$ area; average impedance, $37 \text{ k}\Omega$ at 1 kHz) in freely moving rats.²¹³ Further scaled versions of this type

of approach involve probes with subcellular structural features and mechanical properties that resemble those of neurons. These bioinspired neuronlike electronics (NeuE) induce minimal neuronal loss and neuroinflammation while exhibiting structurally (bending stiffness, $2.0 \times 10^{-9} \text{ N m}^2$) and functionally (Pt electrodes; impedance, $0.6 \text{ M}\Omega$ at 1 kHz) stable interfaces for more than 3 months (Figure 10d).²¹⁴ Although these platforms have demonstrated important modes of use and their utility can, in principle, extend beyond electrical interfaces, they support only limited levels of 3D integration. Ideas that allow functionality to be distributed in arbitrary ways across a 3D space to capture the networked activity of the brain are, in general, preferred.

Opportunities in 3D neural interfaces extend beyond animal models to include human patients as well, although additional work is necessary to address the many risk factors. In this respect, 3D neural interfaces to 3D cultures of hiPSCs, sometimes known as organoids, are important. Recent advances in hiPSC development and tissue engineering establish routes to 3D biological constructs with anatomical and functional characteristics approaching those of human organs and with features that cannot be observed with animal models. As

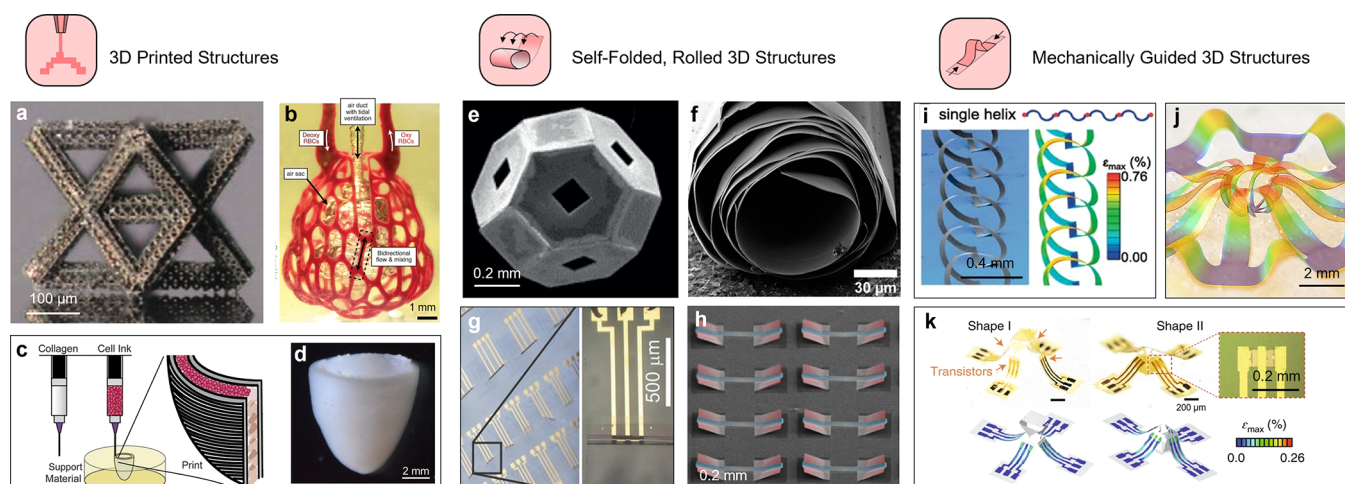


Figure 12. Examples of 3D assembly methods. (a–d) Three-dimensionally printed complex 3D architectures. (a) Microscale metamaterials prepared by large area projection microstereolithography.²⁴⁰ Reproduced with permission from ref 240. Copyright 2016 Springer Nature. (b) Optical image of a 3D-printed hydrogel-based distal lung subunit.²⁴³ Reproduced with permission from ref 243. Copyright 2019 American Association for the Advancement of Science. (c) Schematic illustration of dual-material printing using a collagen ink and a cell ink. (d) Optical image of a 3D-printed ventricle.²⁵⁷ Reproduced with permission from ref 257. Copyright 2019 American Association for the Advancement of Science. (e–h) Self-folded and self-rolled 3D structures. (e) Self-folded microstructure connected by solder hinges.²⁵⁹ Reproduced with permission from ref 259. Copyright 2011 National Academy of Sciences. (f) SEM image of the cross-sectional area of the Si–Ge microbattery.²⁶¹ Reproduced with permission from ref 261. Copyright 2020 Wiley-VCH Verlag GmbH & Co. KGaA. (g) Array of self-assembled IGZO transistors, logic elements, and amplifiers (left). Magnified image (right) of self-rolled electronics.²⁶⁹ Reproduced with permission from ref 269. Copyright 2015 Wiley-VCH Verlag GmbH & Co. KGaA. (h) Array of self-rolled 3D microstructures.²⁶⁰ Reproduced with permission from ref 260. Copyright 2021 Springer Nature. (i–k) Deterministic mechanically guided complex 3D architectures. (i) Three-dimensional single-helical silicon coil (left) and corresponding FEA prediction (right).²⁸¹ Reproduced with permission from ref 281. Copyright 2015 American Association for the Advancement of Science. (j) Compliant 3D mesostructures to precisely evaluate the mechanical characteristics of organoids.²⁹³ Reproduced with permission from ref 293. Copyright 2021 Wiley-VCH Verlag GmbH & Co. KGaA. (k) Two configurations of 3D microelectronic devices by multistable buckling mechanics.²⁹⁴ Reproduced with permission from ref 294. Copyright 2018 Springer Nature.

explained in the **Introduction**, conventional *in vitro* neural interfaces such as patch clamps,^{35,36} probe shanks,^{40,215} and multielectrode arrays (MEAs)^{33,34} have limited functional applicability to such 3D culture systems due to their 2D formats. The most important historical example of *in vitro* neural interfaces involves the patch clamp system²¹⁶ for monitoring individual cells. Advanced platforms that use CMOS technologies as the basis for high resolution MEAs²¹⁷ offer important capabilities in recording subcellular neural activity and associated networks that form in cultures of cortical neurons. Recent form factors in MEAs include vertical nanowire electrode arrays (VNEAs) to allow for intracellular neural recordings from cells cultured on top.^{218–220} Exploiting these and other advances in 3D architectures defines an important future in neural interface development, as outlined in the following sections.

3.1. Advanced Routes to 3D Structures

The network diagram in **Figure 11** summarizes emerging technologies that form neural interfaces with 3D geometries. For instance, microfabricated filamentary probes in rigid or soft formats can penetrate the brains of animal models, as described in the examples of the previous section. These types of probes can, in principle, be used as supports for μ -ILEDs, microfluidic channels, or electrochemical sensors for multifunctional platforms. Other schemes involve culturing 2D sheets of stem cells onto open mesh nanoelectronic structures, to yield electrodes embedded directly into 3D tissues as organoids self-assemble through organogenesis. Three-dimensional printing allows for precise layer-by-layer arrangements of combinations of biocompatible polymers, composite metamaterials, and even living cells into volumetric structures. Folding and rolling deformations that leverage effects such as strain mismatch between

disparate layers can serve as a form of origami inspired 3D self-assembly for biointegration. Here, soft tissues can be placed onto 2D precursors that then roll, fold, or otherwise deform to wrap the technology around these tissues. One of the most sophisticated approaches uses mechanically guided assembly for precisely controlled 3D transformations to access geometries beyond cylinders and conical shapes. Here, the 2D precursors move into 3D shapes via the action of stresses imposed on them by an elastomeric substrate. The following sections introduce these schemes and the latest results that exploit them in 3D neural interfaces for biological systems, including 3D cell cultures and engineered tissues.

3.1.1. Three-Dimensional Printing. Three-dimensional printing can create diverse structures in a variety of polymers, ceramics, metals, and other classes of materials.^{221–223} For applications directly relevant to biointerfaces, biomaterial resins (bioresins) and inks (bioinks) comprised of combinations of biocompatible synthetic polymers (e.g., PEG, silicone elastomers, PCL) with natural polymers/proteins (e.g., alginate, collagen, fibrinogen, agarose, gelatin, growth factors) and living cells²²⁴ are particularly important. Known as 3D bioprinting, these techniques and materials provide access to 3D constructs as bionic organ models,^{225–230} bioprosthetics,^{231,232} tissue-engineered bones,^{233,234} and vascular networks,^{235,236} among others. Three-dimensional printing methods can be broadly divided into light- and ink-based approaches, described in the following.

Light projection or laser scanning techniques offer the highest resolution, typically with photocurable resins (stereolithography (SLA), two-photon/multiphoton polymerization (TPP), xolography²³⁷). SLA involves a bath of photoactive monomers,

oligomers, and catalysts that undergo local photopolymerization and cross-linking across a near-surface region. Sequential application of this process yields desired 3D structures. The latest versions of this method use digital light processors (DLPs)²³⁸ and gas-permeable windows to prevent curing at the exposure interface, thereby allowing monomers to fill across the windows as the cured parts move away in a continuous fashion as part of the 3D fabrication process, known as continuous liquid interface production (CLIP).²³⁹ The resulting polymeric structures can serve as scaffolds or as sacrificial templates for other materials. A combination of SLA and DLP techniques, known as large area projection microstereolithography (LAP μ SL), can yield hierarchical metamaterials with high-resolution (50–700 nm thick) nanotubes as the base units (Figure 12a).²⁴⁰ These tubes can also act as the basis for 3D fluidics platforms that exploit capillary driven flow through convoluted, branched lattice networks with deterministic control over multiphase flow, transport, and reaction processes.²⁴¹ As examples of projection-based bioprinting of biointerfaces, recent reports describe rapid formation of complex tissue-like constructs (10 s/layer) by projecting 2D patterns of light (405 nm wavelength) into a rotating cell-laden bioresin container consisting of gelatin methacryloyl (gelMA) and lithium phenyl-2,4,6-trimethylbenzoyl-phosphine (LAP) as the photoinitiator for free-radical polymerization of the methacryloyl moieties to print bone models in 12.5 s.²⁴²

Other forms of projection SLA allow for complex 3D structures such as vascular networks integrated into lunglike (alveolar) models and hydrogel carriers for liver cells.²⁴³ Bioresins composed of PEGDA (6 kDa, 20 wt %), LAP as the photoinitiator, tartrazine as the photoabsorber, and human lung epithelial cells and fibroblasts (10×10^6 cells/mL) can be photopatterned using projection SLA to form alveolar models based on a Weaire–Phelan 3D tessellation with convex polyhedral base units. The tessellation can be smoothed and reduced in size into fusions of spheres that resemble native alveolar air sacs.²⁴⁴ Another meshlike tessellation structure formed by removing the faces of the polyhedra yields a highly vascularized, branched vessel network (185 vessel segments, 13 fluidic branch points) reminiscent of the capillaries surrounding the lung (Figure 12b). The efficiency of intervascular interstitial transport can be assessed by measuring the delivery of oxygen from a source vessel to perfused human red blood cells. Bioprinted vascularized microchannel networks can be seeded with human umbilical vein endothelial cells (HUVECs; 10 million cells/mL) and hepatic aggregates (rat primary hepatocytes, dermal fibroblasts; 45 000 aggregates/mL) suspended within a fibrin hydrogel for implantation into rodent models with chronic liver injury.²⁴³

Alternative photocuring processes use short-pulsed laser scanning and TPP to yield structures with exceptionally high spatial resolution (as high as 30 nm), although typically over relatively small volumes (~ 1 cm³).²⁴⁵ Large-area, multibeam forms of TPP seek to overcome this limitation by use of diffractive optical elements that split a single excitation beam into nine beamlets to print, in a parallel fashion, 9×9 arrays of microstructures ($450 \times 450 \mu\text{m}^2$ total area) simultaneously, with examples of towers (30 μm height) spaced 50 μm apart stitched together with walls (27 μm height) as cell scaffolds for HeLa immortalized cells.²⁴⁶

In general, light-based methods offer exceptional capabilities in 3D nano/microfabrication, but with stringent materials requirements in the form of photopolymerizable resins resulting

in thermoset polymers. Thus, overall, SLA-based 3D printing methods have outstanding potential to rapidly produce high-resolution constructs, but in terms of bioprinting, challenges in cell viability (nutrition, oxygen supply), bioresin properties (structural/printing fidelity), and difficulties with multimaterial printing processes limit sophisticated examples of biointerface platforms.^{247,248}

Three-dimensional printing methods that use nozzles and inks bypass these material constraints. The inks in these cases span polymeric or particulate species tailored with rheological properties (viscosity, surface tension, shear yield stress, shear elastic and loss moduli) optimized for either droplet-based or filament-based schemes.^{221,222} Droplet-based methods, such as direct inkjet printing, rely on thermal or acoustic actuation to create and direct low-viscosity liquid droplets toward a substrate from a printhead. Sequentially repeating this process can yield 3D structures. By contrast, methods that continuously extrude soft materials as filaments from fine nozzles provide direct routes to 3D structures of relevance to biointerfaces, across a wide variety of compatible materials. Examples range from thermoplastic polymers (e.g., acrylonitrile–butadiene–styrene (ABS), PLA, PC) in techniques that use heating to facilitate the extrusion, known as fused deposition modeling (FDM), to viscoelastic materials that undergo shear thinning, for direct ink writing (DIW). This latter method is particularly attractive due to its versatility with materials classes,²⁴⁹ multimaterial printing methods (embedded 3D printing,²⁵⁰ multimaterial–multinozzle 3D printing²⁵¹), and direct customization with processing methods (UV LEDs, heaters²⁵²) to form 3D freestanding structures.²⁵³ The wide compatibility of a range of materials is important, where ink formulations can be selected for high structural fidelity, biocompatibility, cell viability, and host tissue engraftment, as reviewed in further detail elsewhere.^{224,254,255}

As some recent examples that foreshadow opportunities in neural interfaces, one study describes 3D-printed cardiac patches and heart models with bioinks engineered from human or porcine adipose tissue samples.²³¹ The fatty tissue is decellularized to form a personalized hydrogel with collagenous nanofibers while the cellular components are reprogrammed into cardiomyocytes and endothelial cells and mixed into bioinks that are used to print cardiac patches (2 mm thick) for transplantation into rodent models. A cellularized and vascularized heart model (20 mm height, 13 mm diameter) formed by bioink-based printing exploits a support medium (alginate microparticles embedded in extracellular polysaccharide gum) that can be safely enzymatically or chemically degraded for extraction (Figure 12c).

A similar 3D bioprinting technique, referred to as free-form reversible embedding of suspended hydrogels (FRESH), offers the possibility of depositing biological hydrogel precursor inks (e.g., alginate, fibrin, collagen I) into a thermoreversible support bath consisting of a slurry of gelatin microparticles (65 μm average diameter) formed by mechanically blending a gelatin block that melts away at 37 °C.²⁵⁶ A recent extension of this method, coined FRESH v2.0, can form components of the heart (ventricle, trileaflet valve, neonatal scale heart model) with a gelatin slurry support bath created through a coacervation method to produce microparticles (25 μm average diameter) that enhance the collagen printing resolution from 200 to 20 μm diameter filaments. The result allows for biomimetic models of the heart (Figure 12d), such as a contractile ventricle model designed as an ellipsoidal shell (6.6 mm maximum outer

diameter, 8 mm height) FRESH printed with a collagen bioink and a high-density cellular bioink consisting of human embryonic stem cell derived cardiomyocytes (hESC-CMs) and 2% cardiac fibroblasts.²⁵⁷

3.1.2. Self-Folding and Self-Rolling Assembly. As complements to these schemes for direct patterning, rolling and/or folding mechanisms allow formation of certain types of 3D architectures from 2D precursors, where transformation occurs by the action of engineered stresses in thin cantilevers or sheets. The required forces can arise from three main sources: capillarity,^{258–260} thin-film residual stresses,^{261–265} and active (i.e., stimuli-responsive) materials.^{221,266–269} As an example of the first, heating of a metal solder (e.g., Sn, Pb–Sn) patterned along lines above its melting point leads to a change of shape to minimize its surface energy, resulting in folding or locking processes.^{270,271} Figure 12e presents a submillimeter-scale polyhedron created by this type of self-folding assembly with an algorithmic design.²⁵⁹ Melting of electrodeposited solders (Pb–Sn; melting temperature 183 °C) on polygonal Ni panels moves hinges for each panel and results in self-folding at the edges of the 2D nets to create a self-assembled 3D geometry (1 mm height for the smallest feature). Similarly, water droplets or liquid polymers can also act as a source of capillary force to lift 2D sheets of SiNMs (1.25 μm thick) into 3D single crystalline assemblies of various geometries (e.g., tetrahedral pyramid, sphere).²⁵⁹

Three-dimensional assembly induced by thin-film residual stresses uses mismatches in mechanical strains of stacked thin films (e.g., Si_xN_y, ZnO, TiO₂, Al₂O₃, GaAs, Cr, vanadium dioxide (VO₂), germanium (Ge)).^{221,260,272} Such multilayers can be prepared on substrates with sacrificial layers that, upon their removal, lead to self-rolling to form tubular, scroll-like, or polyhedral geometries. This process can transform microfabricated 2D electronic structures into 3D geometries for various applications (e.g., energy,^{261,262} optoelectronics,^{263,273} electronics,^{261,263–265} biological studies^{274–277}). Thin, tubular SiNM-based photodetectors exhibit 1000 times enhancements in photoresponsivity compared to 2D devices due to light-trapping effects. One such type of photodetector consists of two Cr electrodes (25 nm thick) on an SiNM (20 nm thick) with 20-μm-wide Si channels (20 nm thick) microfabricated on an SiO₂ sacrificial layer.²⁷³ Microbatteries that exploit Si–Ge compound rolls in spiral configurations as anodes (60 and 20 nm thick, respectively with a PAAm supporting layer) are also possible. In a specific device, a planar Si–Ge layer with a footprint of 24.7 mm² transforms into a 3D roll (~1.1 mm² footprint) to create a high mass loading (21-fold) of cathode materials (LiMn₂O₄ powders) and short charge transfer pathways (Figure 12f).²⁶¹ As a biological application, self-rolled microtubes (4–5 μm diameter) allow for aligned growth of hippocampal neurites, with the ability to construct deterministic neural circuits.²⁷⁵ Although not yet fully explored in neural interfaces, these types of devices offer interesting possibilities as electrically active axonal or dendritic conduits.

Structures consisting of bilayer or multilayer heterogeneous designs can transform into 3D geometries with external stimulation (e.g., exposure to water, heat) to induce mismatched strains. The resultant structures can reversibly morph their shapes (from 2D to 3D or vice versa) in response to changes in environmental conditions. Representative constituent materials include hydrogels,^{269,277} phase-transition materials,²⁶⁰ and shape-memory polymers (SMPs).²⁷⁸ Figure 12g shows a hydrogel cuff implant with integrated microelectronic compo-

nents including signal amplifiers and logic circuitry based on indium gallium zinc oxide (IGZO) transistors.²⁶⁹ The platform includes a strained bilayer consisting of active electronic devices on a PI layer capped with a stimuli-responsive hydrogel based on *N*-(2-hydroxyethyl)acrylamide (HEAA) and poly(ethylene-*alt*-maleic anhydride) (PEMA) in *N,N*-dimethylacetamide (DMAc) (1 μm thick). Changes in solution chemistry or pH can alter the swelling state of the hydrogel, thereby changing the overall geometry through rolling. Introduction of isopropanol (IPA) reverses the process by cleaving the hydrogen bonds in the hydrogel network, leading to dehydration. The resulting shrinkage causes the device to unroll, eventually transforming it back into its planar configuration, in a reversible manner. This chemical transformation forms the basis of tunable microtubes ranging from 50 μm to 1 mm in diameter.²⁷⁹

A temperature-responsive alternative involves narrow strips of Cr (30 nm thick) and thin films of VO₂ (~20 nm thick) on a Si substrate with a SiO₂ sacrificial layer. Selective etching of the SiO₂ layer with hydrofluoric acid releases the Cr/VO₂ bilayer resulting in self-folding into a bent configuration or rolling into a tubular shape (<30 μm diameter; Figure 12h). The resultant rolled shape can rapidly (within ~5 μs) transform into a folded shape through a thermally induced metal–insulator phase transition of VO₂.²⁶⁰ Similar transformations can be achieved by stretching or deforming thin films of SMPs at temperatures above their characteristic transition, followed by cooling and release of the applied force.²⁷⁸

3.1.3. Mechanically Guided Assembly. Figure 12i–k summarizes a relatively recent scheme to create 3D frameworks through mechanically guided assembly initiated by forces imparted through a prestrained elastomer substrate. This method begins with fabrication of a thin 2D precursor structure on a carrier substrate, followed by release and patterned chemical functionalization of selected regions on the backside. Transfer to a prestretched elastomeric substrate leads, upon contact, to strong chemical bonds at these regions (bonding sites) and weak, nonspecific adhesion interactions at others. Relaxing the substrate induces compressive buckling that leads to geometric transformation into an engineered 3D configuration through spatially dependent deformations and in-plane and out-of-plane translational and rotational motions. Computational models guide the selection of 2D precursor geometries, bonding site layouts, and prestrain distributions to realize desired 3D architectures.

Three-dimensional structures formed in this way can have diverse functions depending on the layouts and materials in the 2D precursor. The feature sizes can range from the nanoscale to the macroscale^{280–282} with materials such as polymers,^{280,283} metals,²⁸⁴ and semiconductors,^{281,284,285} either permanent or bioresorbable.²⁸⁶ Complex circuit traces and associated active²⁸⁷ and passive^{285,288} components can be combined in complex, flexible 3D devices with broad relevance in energy,²⁸⁹ biological,^{52,290} and biomedical systems.^{288,291,292} The compressive forces applied by the elastomeric substrate maintain the 3D geometry; specialized materials (e.g., shape memory polymers (SMPs)²⁸³) and approaches that use mechanical interlocking designs²⁸⁶ allow these 3D structures to be released from the substrate as freestanding objects.

Figure 12i shows finite element analysis (FEA) simulations and SEM images of a single helical coil of device-grade monocrystalline silicon supported by photodefinable epoxy (SiNM/SU-8, 100 nm/1.2 μm thick), as the potential basis of a 3D electrical neural interface.²⁸¹ Figure 12j features an optical

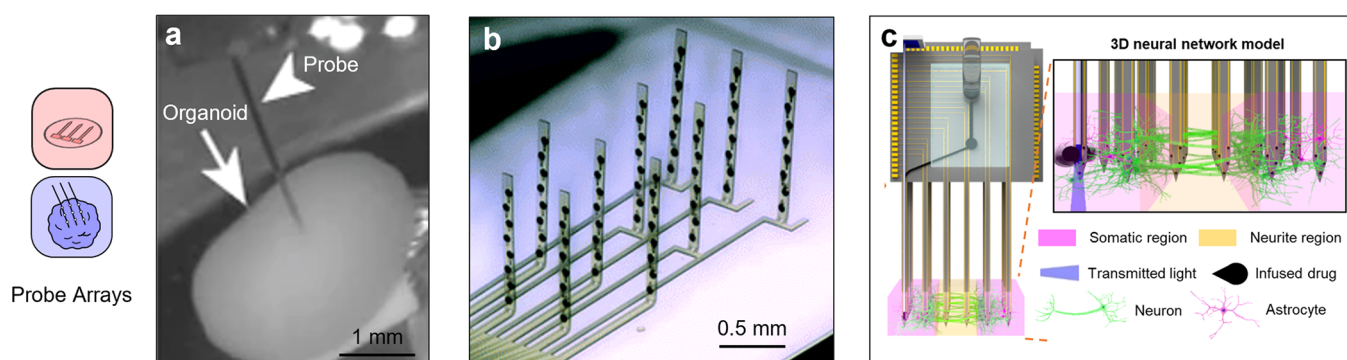


Figure 13. Probe array structures as 3D interfaces. (a) Probe shank implanted into a brain organoid for electrophysiology.⁴⁰ Reproduced with permission from ref 40. Copyright 2017 Springer Nature. (b) Actuated flexible array of multielectrode probes for *in vitro* studies.²⁹⁷ Reproduced with permission from ref 297. Copyright 2020 The Royal Society of Chemistry. (c). Schematic illustration of an assembled 3D multifunctional MEA with an optofluidic interface implanted into engineered brain tissue compartmentalized with somatic and neurite regions.⁵⁵ Reproduced with permission from ref 55. Copyright 2021 Springer Nature.

image of 3D mesoscale frameworks and corresponding computed geometries, as an illustration of the utility of computationally guided design approaches. These structures use parylene-C as transparent, biocompatible enclosures to facilitate probing of the mechanical characteristics of cerebral organoids (~ 2 mm diameter) through nanoindentation,²⁹³ the results of which show systematic variations in elastic modulus with age (1.5–2 kPa, for 60–100 days; 2–2.5 kPa, for over 100 days). These enclosures can be opened and closed reversibly by stretching and releasing the elastomer substrate. Such manipulations allow complex, morphable 3D electronic devices, as shown in Figure 12k. This example includes an array of four silicon n-channel metal–oxide–semiconductor field-effect transistors (n-MOSFETs) with Au electrodes (150 nm thick) on a PI substrate (2 μm thick) in a 3D tower-shaped structure with four supporting struts.

The morphing process can convert this shape into a recessed well configuration,²⁹⁴ as the basis for platforms that can change dynamically to follow or induce similar dynamic changes in surrounding biological tissues. As an early example, multiple hydrogel filaments (poly(*N*-isopropylacrylamide) (pNIPAM) and poly(2-hydroxyethyl methacrylate) (pHEMA)) coated onto 2D precursors transform into 3D geometries to demonstrate helical 3D ECM models.²⁹⁵ In addition, cellular migration behaviors, temporal dependencies, and contact guidance occur after seeding cell cultures (NIH 3T3 fibroblast and primary rat dorsal root ganglia (DRG)) around microscale open or complex 3D frameworks.²⁹⁵ Integration of electronics on this 3D structure enables monitoring of electrical activity from DRG cells.²⁹⁶ Of note is that other, less well controlled, changes in the shape of a substrate can induce geometrical transformations of 2D precursors, as described subsequently where the substrate itself is a living, growing tissue.

3.2. Implementation of 3D Neural Interfaces

The 3D systems described in the preceding sections have great potential as 3D neural interfaces when integrated with electronic circuits, optoelectronic components, microfluidic elements, and others. Three-dimensional bioprinting of functional materials integrated with interconnected collections of active elements is of particular interest. Three-dimensional assembly methods that exploit 2D-to-3D transformation (e.g., self-rolling and folding, and mechanically guided assembly) can create complex, and multifunctional forms of 3D bioelectronics aligned with capabilities from the semiconductor industry, as tissue

embedding or tissue surrounding interfaces. The following sections highlight some of the most recent examples, starting with arrays of penetrating probes and then with 2D tissues cultured on mesh-type electronics that transform into 3D by processes of organogenesis. Other 3D demonstrations rely on self-rolled arrays of multielectrodes that surround cells or 3D tissues. A final set of illustrations exploits various complex 3D frameworks. The examples in some cases involve interfaces to cardiac tissues that likely have neural applicability.

3.2.1. Probe Arrays. Arrays of multicomponent probes represent one of the most straightforward approaches to 3D interfaces. Conceptually similar to the “Neuropixel”²¹² platforms described previously, recent work shows that collections of 64 microelectrodes integrated onto penetrating probes (35–60 μm tapered width, 15 μm thick) can capture intercellular interactions within millimeter-scale 8-month-old organoids *in vitro*, as demonstrated by observations of suppressed neural activity of photosensitive neurons (four out of the 10 8-month-old organoids) due to illumination of 530 nm light (Figure 13a).⁴⁰ Figure 13b outlines another example, consisting of an array of 10 probes (1100 \times 90 μm^2 area, ~ 15 μm thick) each with 80 electrodes (Pt black; 37 k Ω at 1 kHz; 50 μm diameter), formed in 2D layouts but designed with polymeric hinges that can irreversibly deform to create an array of vertical posts. Such platforms can be used to monitor the neural activity of iPSC derived neurons and astrocytes embedded in ECM–collagen hydrogel matrixes (Neucyte; 70:30 glutamate-sensitive to GABA-responsive neurons, 75:25 neurons to astrocytes ratio) during growth of neuronal processes.²⁹⁷ Multifunctional probes (17 recording shanks) with three or four recording microelectrodes (Pt black; 20 \times 20 μm^2 area; 15 k Ω at 1 kHz), an optical fiber (60 μm diameter, GIF50, Thorlabs), and pharmacological modulating microfluidic systems (10 \times 12 μm^2 cross-sectional area) embedded into engineered neural tissue can precisely monitor and modulate neural activities. Particularly, interfaces to engineered brain tissue (2.5 \times 1.5 \times 0.5 mm³) compartmentalized into two somatic and neurite regions (middle) allow for monitoring of the temporal evolution of neural network dynamics during neural development (Figure 13c).⁵⁵

3.2.2. Transformable Mesh Structures. Two-dimensional mesh structures can form 3D interfaces, as organogenesis induces the 2D-to-3D transition during growth from 2D sheets of embryonic cells. Figure 14a shows a 3D neural interface that

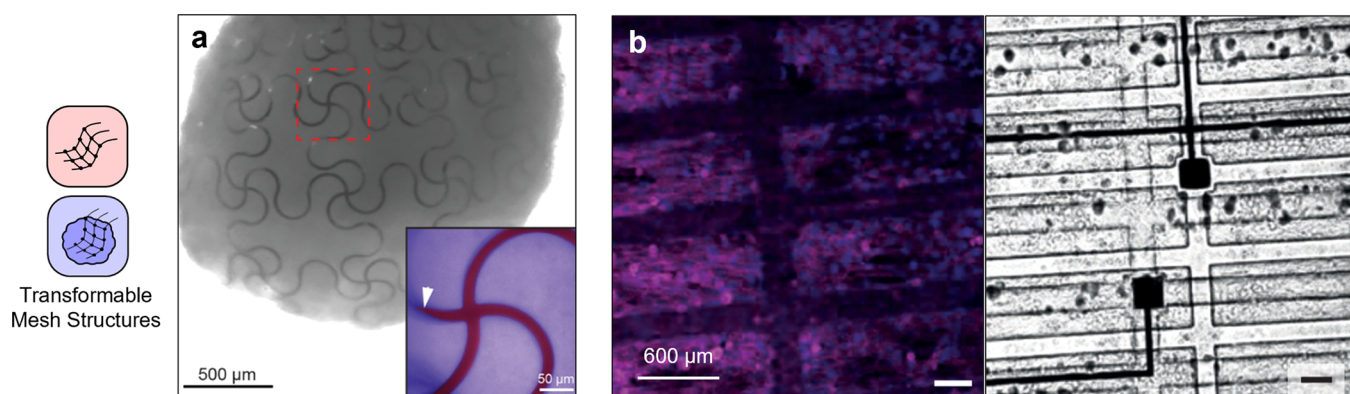


Figure 14. Transformable mesh structures as 3D interfaces. (a) Tissue embedding nanoelectronics via organogenesis for electrophysiological study.⁵⁰ Reproduced from ref 50. Copyright 2019 American Chemical Society. (b) Confocal microscopic image (left) and bright field optical images (right) of cardiac tissue within a 3D bioelectronic scaffold (sarcomeric actinin is in pink, nuclei are in blue (Hoechst 33258)).⁵¹ Reproduced with permission from ref 51. Copyright 2016 Springer Nature.

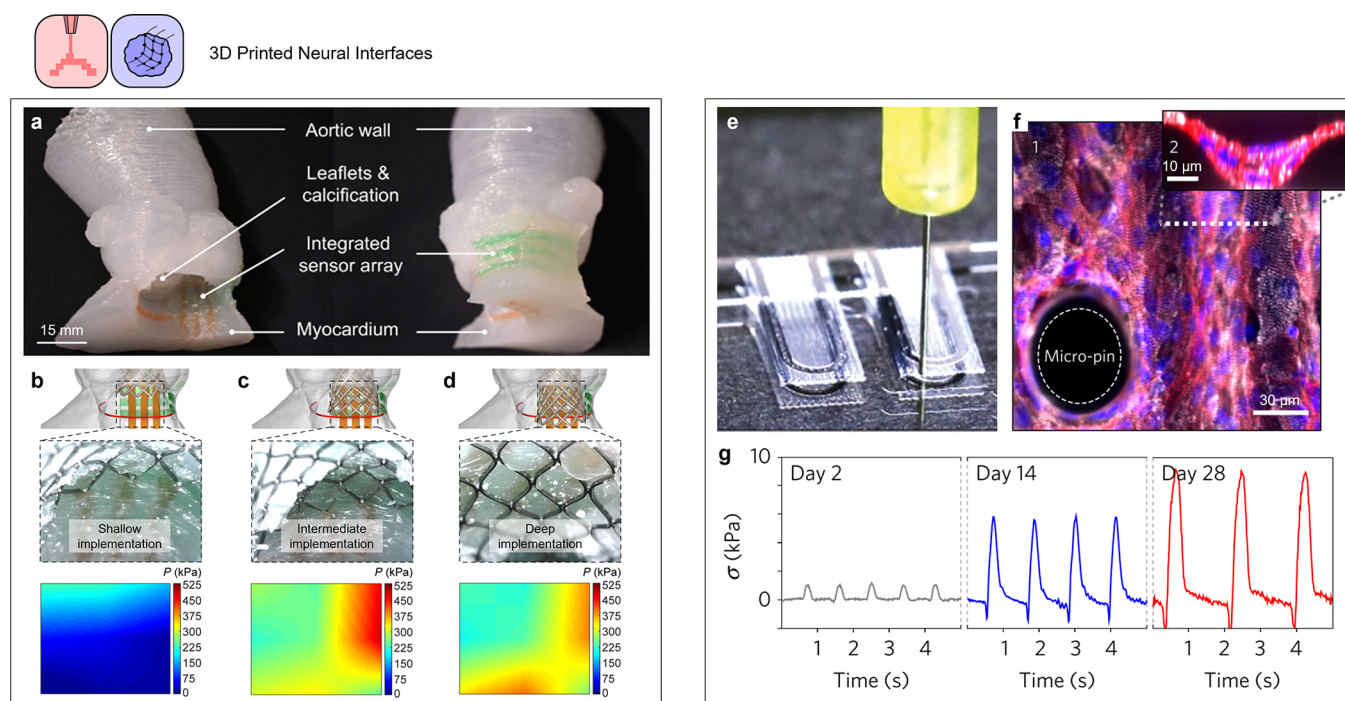


Figure 15. Three-dimensional printed structures as 3D interfaces. (a–d) Three-dimensional printed aortic root model with internal sensor arrays and visualization of applied pressures after valve implantation. (a) Three-dimensional printed aortic root model with internally integrated sensor array. Implantation of the 29 mm Evolut R TAVR valve frame at a shallow height (b), an intermediate height (c), and a deep height (d).³⁰⁴ Reproduced with permission from ref 304. Copyright 2020 American Association for the Advancement of Science. (e–g) Multimaterial 3D-printed instrumented cardiac device. (e) Automated printing process. (f) Laminar tissue on the surface of a cantilever with micro-pin and cross-sectional image (inset) of thicker laminar tissue in grooves (scale bar, 10 μm) with DAPI nuclei stain (blue), α -actinin (white), and actin (red). (g) Representative traces of contractile twitching of cardiac laminar tissue measured with a 3D-printed device after 2, 14, and 28 days.³⁰⁷ Reproduced with permission from ref 307. Copyright 2017 Springer Nature.

exploits this concept to distribute stretchable meshlike arrays of electrodes ($0.5 \times 1 \text{ mm}^2$ area; PEDOT on 50 nm Pt electrode; 20 μm diameter, 70 k Ω at 1 kHz) throughout a 3D organoid ($\sim 1 \text{ mm}$). Here, hiPSC derived cardiac progenitor cells seeded on a platform of mesh electronics with serpentine layouts and a filling ratio of less than 11% (20 μm /0.8 nm width and thickness of ribbon) undergo 3D self-organization via organogenesis to form a millimeter-scale spherical shape with integrated electronics. Electrophysiological monitoring finds synchronized local field potential propagation across the cardiac organoid.⁵⁰

In a conceptually similar manner but in technology with additional capabilities in modulation, Figure 14b shows an electronic mesh embedded in a cardiac tissue as a multifunctional (electrical sensing and pharmacological modulation) patch. Here, a platform of 2D mesh electronics ($\sim 5 \times 20 \text{ mm}^2$ size) seeded with cardiomyocytes is manually manipulated into a 3D shape such that, after continued growth, the electrodes (TiN, 50 \times 50 μm^2 size, $\sim 0.1 \text{ k}\Omega$ at 1 kHz) are dispersed throughout the 3D cellular network. The system can detect electrophysiology throughout the 3D scaffold, and it can also electrically stimulate the cardiac tissue with the electrodes,

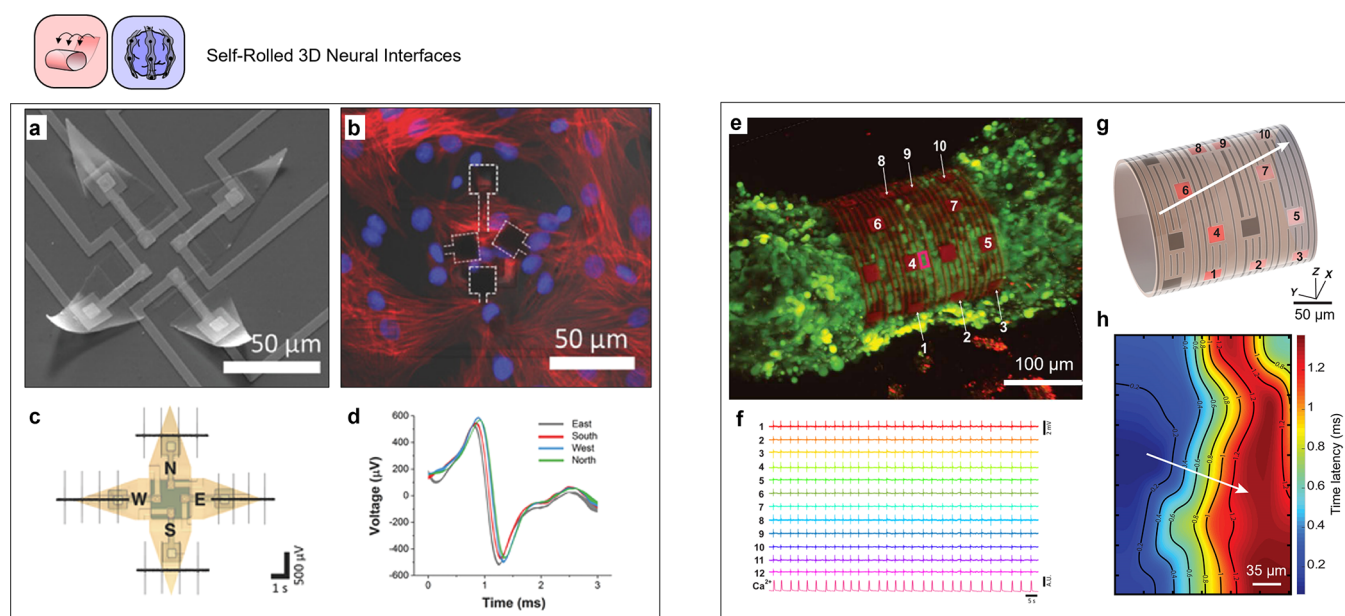


Figure 16. Self-rolled structures as 3D interfaces. (a–d) Microfabricated self-folded multielectrode shell. (a) SEM image of a half-closed shell structure. (b) Confocal microscopic images showing actin filaments (red) and cell nuclei (blue) with multiple electrodes wrapped around the cells (dashed white lines). (c) Measured extracellular recordings from individual electrodes of the 3D electronic shell. (d) Overlay of averaged action potentials recorded by each of the four electrodes.⁵² Reproduced with permission from ref 52. Copyright 2018 Wiley-VCH Verlag GmbH & Co. KGaA. (e–h) Self-rolled 3D biosensor array for cardiac spheroids. (e) Confocal microscopic image of a 3D cardiac spheroid labeled with Ca^{2+} indicator dye (Fluo-4, green) enclosed with bioelectronics. (f) Representative field potential traces recorded from individual electrodes with simultaneously recorded Ca^{2+} fluorescence intensity. (g) Three-dimensional rendered demonstration of signal propagation at $t = 22.7$ ms. Scale bar, $50 \mu\text{m}$. (h) Two-dimensional representation of the isochronal map of time latencies. Scale bar, $35 \mu\text{m}$. The white arrows in (g) and (h) represent the direction of the average conduction velocity.⁵³ Reproduced with permission from ref 53. Copyright 2019 American Association for the Advancement of Science.

causing visible synchronous contractions. As forms of pharmacological modulation, biomolecules and pharmacological agents such as lysozyme, stromal cell derived factor-1 (SDF-1), insulin-like growth factor 1 (IGF-1), vascular endothelial growth factor (VEGF), and dexamethasone (DEX) can be loaded into the tortuous pores of the hydrogel component of the platform, for release upon electrical stimulation to the gel.⁵¹

3.2.3. Three-Dimensional Printing. The materials and 3D structure geometries that can be realized by 3D printing provide vast opportunities in biointegration, many of which are demonstrative or suggestive of applications in neural interfaces. Three-dimensional bioprinting is particularly attractive for structural components such as supercapacitors,²⁹⁸ photodetectors,²⁹⁹ neural regeneration devices,³⁰⁰ microfluidic platforms,³⁰¹ and soft actuators,³⁰² with ongoing efforts for functional device integration as reviewed and reported elsewhere.^{247,248} In some cases, the process of 3D printing can be conducted directly onto living organs *in situ*.³⁰³

As an example of some possibilities, one study describes a 3D-printed patient-specific aortic root model integrated with internal capacitive pressure sensors (3×3 array) as a platform for transcatheter aortic valve replacement (TAVR) preprocedural planning and also as a bench-top tool for clinicians to mitigate risks associated with TAVR.³⁰⁴ The design of the aortic root model (Figure 15a) follows computed tomography scans of patient cardiac anatomy and is printed with an acetoxysilicone sealant as the active agent and a silicone grease as the bulking agent. Each sensing element consists of two layers of conductive electrodes based on ionic hydrogels (acrylamide monomer dissolved in lithium chloride with N,N' -methylenebis(acrylamide) cross-linking agent and 2-hydroxy-2-methylpro-

piophenone photoinitiator) separated by a silicone dielectric, embedded into the walls of the model. The devices transduce capacitance changes as a result of deformations of the dielectric layer to changes in pressure, calibrated to map the pressures imposed by a TAVR valve implanted into the aortic root model (Figure 15b–d).

As an example of an instrumented microphysiological device, Figure 15e presents a 3D-printed structure fabricated via DIW seeded with neonatal rat ventricular myocytes (NRVMs; 1.40×10^5 cells/ cm^2 seeding density) in 10% fetal bovine serum and human induced pluripotent stem cell derived cardiomyocytes (hiPS-CMs) to form cardiac laminar tissue (Figure 15e,f). A key feature is a multilayer cantilever composed of thin individual layers (0.5 – $6.5 \mu\text{m}$ thick) of highly dilute polymer-based inks with properties that complement the range of stresses generated by laminar cardiac tissue (1 – 15 kPa ^{305,306}). The cantilevers are printed with a water-soluble sacrificial release layer (dextran ink; $0.5 \mu\text{m}$ thick), a base layer (thermoplastic polyurethane (TPU) ink; 1.6 MPa modulus, $3 \mu\text{m}$ thick), strain gauge wires (TPU doped with 25 wt % carbon black nanoparticles (CB:TPU) ink; 8.8 MPa modulus, $1.19 \Omega \text{ cm}$ resistivity, $6.5 \mu\text{m}$ thick), wire cover layers (TPU ink; $1.5 \mu\text{m}$ thick), a tissue-guiding filament layer (PDMS ink; 1.28 MPa modulus, $60 \mu\text{m}$ wide, $2 \mu\text{m}$ tall), electrical interconnect/contact pads (polyamide ink doped with Ag particles, $6.6 \times 10^{-5} \Omega \text{ cm}$ resistivity), and a PDMS encapsulation layer. Grooved filamentary microstructures on the tissue-guiding layer cause the NRVM to assemble into laminar cardiac tissue. The contractile development of the cardiac tissue can be monitored over 28 days, to track maturation of the tissue through increases in longitudinal contractile stresses (Figure 15g).³⁰⁷

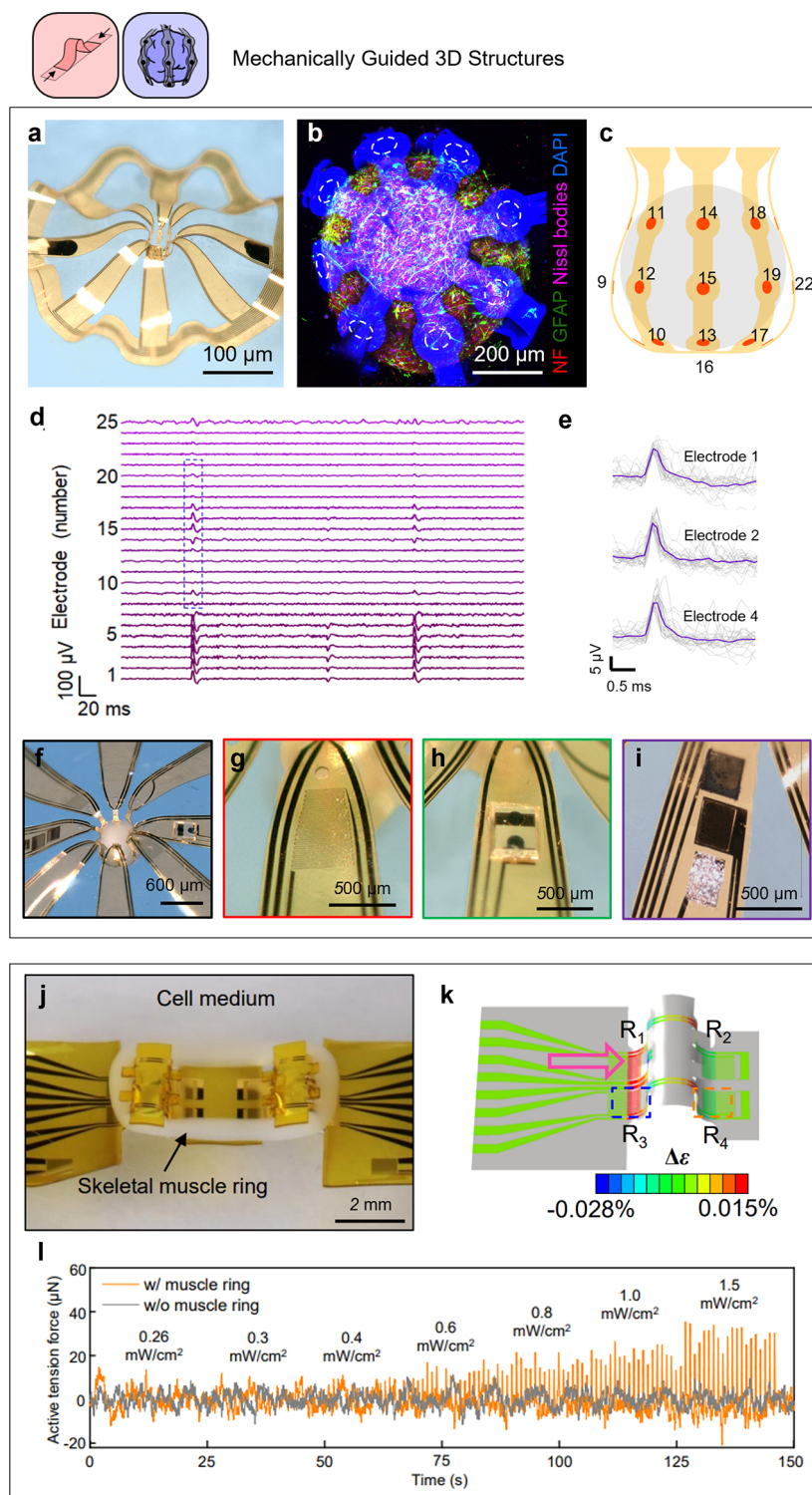


Figure 17. Mechanically guided multifunctional 3D frameworks as 3D interfaces. (a) Optical image of 3D bioelectronic device. Confocal fluorescence microscopic image of (b) cortical spheroid and (c) assembloid of two spheroids labeled with neurofilament (red), glial fibrillary acidic protein (green), Nissl bodies 797 (magenta), and DAPI nuclear stain (blue) enclosed in a 3D MMF labeled with an autofluorescence of the parylene-C (blue) (bottom left). (d) Representative field potential trace recorded by 25 microelectrodes. (e) Bright field microscopic images and raster plots for assembloids before and after transection. (f) Optical microscopic images of 3D MMF with magnified views of various components (from left to right): (g) serpentine traces for temperature sensing and thermal modulation, (h) microscale light emitting diode for optogenetic stimulation, and (i) three-electrode system as an electrochemical sensor.⁵⁴ Reproduced with permission from ref 54. Copyright 2021 American Association for the Advancement of Science. (j) Optical image of the integration of a skeletal muscle ring with 3D framework. (k) Computed change in strain in response to an indentation displacement of 10 μm from one side of a post. (l) Active tension forces with and without integration with an optogenetic skeletal muscle ring, in response to optical stimulation at intensities from 0.26 to 1.5 mW/cm^2 with 1 Hz pulse frequency and 50 ms pulse width.³⁰⁹ Reproduced with permission from ref 309. Copyright 2021 National Academy of Sciences.

Another 3D bioprinted structure with characteristics of interest to neural interfaces consists of a cardiac patch embedded with stretchable electronics.³⁰⁸ Here, a cellular bioink forms an engineered tissue of an ECM-based hydrogel (decellularized porcine fatty tissue) mixed with neonatal rat ventricular cardiac cells (2×10^8 cells/mL); a conductive bioink composed of graphite flakes ($14.5 \mu\text{m}$ average diameter) suspended in liquid PDMS forms the electrodes for signal recording and stimulation. A dielectric bioink consisting of liquid PDMS and nonionic surfactant (sorbitan oleate) serves as a passivation layer for the electrodes. A $20 \times 15 \times 2 \text{ mm}^3$ patch includes eight serpentine electrodes, six of which are passivated ($\sim 200 \mu\text{m}$ diameter) for point sensing and stimulation while the two outer electrodes are exposed for field stimulation of the entire tissue construct. The system can record electrophysiology from four different locations and can pace the engineered tissue via 50 ms pulses of 7 V electrical stimulation.

3.2.4. Self-Rolling and Folding. Self-rolling and folding methods naturally offer high levels of sophistication in the electronic components and related active devices through the use of materials and fabrication techniques that are commonplace in the semiconductor industry. In one example of a 3D neural interface formed in this manner, tubular microstructures act as microscavolds for human mesenchymal stem cells (hMSCs).²⁷⁶ The tubes consist of Ti alloys (Ti and 45 wt % Nb; 20–50 nm thick) as the residually strained layers relax to cylindrical shapes (12–30 μm diameter) upon removal of an underlying sacrificial layer (Ge, 20 nm thick) with a solution of H_2O_2 . A similar strategy yields an impedimetric microfluidic sensor in a tube for single-cell (CD14+ monocytes) characterization.²⁷⁷ The multilayer precursor includes poly(ethylene-*alt*-maleic anhydride) and *N*-(2-hydroxyethyl)methacrylate as a hydrogel swelling layer, Pt electrodes for electrochemical impedance spectroscopy (EIS), and PI as a support layer. Swelling of the hydrogel layer induces differential strain between the hydrogel and PI layers to self-roll the 2D multilayer into microtubular channels ($\sim 25 \mu\text{m}$ diameter) with Pt electrodes. As monocytes pass through the self-assembled polymeric channel, electrical signals can be captured from the cells and the flux of ions (Na^+ , K^+ , Ca^{2+} , Cl^- , and CH_3COO^-) can be recorded in the surrounding media by EIS.

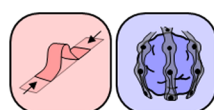
Three-dimensional neural interfaces that can gently enclose 3D biological tissues are also of interest, as multifunctional shells (Figure 16a–d) that form by similar effects in residual stresses. One such structure involves four “arms” ($170 \times 170 \mu\text{m}^2$ area), each of which supports an electrode ($12 \times 12 \mu\text{m}^2$ area) to monitor electrical activity of an individual neonatal rat ventricular cardiomyocyte seeded onto the device in its planar form. Residual strain associated with a SiO/SiO₂ (10/15 nm thick) bilayer on the four arms induces self-folding of the structure to enclose the cells. Measurements reveal extracellular action potentials from each of the four panels (Figure 16c,d) and the propagation of signals within each shell.⁵²

In a related case, hiPSC derived cardiac spheroids can be enclosed by self-rolled cylindrical structures with arrays of electrodes (12 electrodes; PEDOT:PSS, $25 \times 25 \mu\text{m}^2$ area, 250 k Ω at 1 kHz) for electrophysiological monitoring of the behavior of cardiac spheroids in 3D (Figure 16e–h). The 2D precursor consists of photodefined epoxy (100–180 nm thick) as a substrate, a bilayer of Cr/Au (10/75 nm thick) as electrodes, and a trilayer of Cr/Pd/Cr (1/50/25 nm thick) as interconnects. Self-rolling of the prestressed metal/polymer occurs upon removal of a 200-nm-thick Ge sacrificial layer to enclose a

cardiac spheroid (50–200 μm diameter) in a tube with an inner diameter of 160 μm . The high spatial resolution of the arrays provides information on neural activities from individual cells of the spheroid in a 3D cylindrical geometry.⁵³

3.2.5. Mechanically Guided 3D Assembly. The 3D assembly schemes described previously provide access to wide-ranging classes of 3D architectures, beyond cylinders, scrolls, and related shapes. Figure 17a–i highlights a 3D multifunctional mesoscale framework (3D MMF) formed from compressive buckling from a 2D precursor (PI/Au/PI; 4/0.2/4 μm). This 3D MMF includes a flexible, pouch-shaped “cage” structure designed specifically to enclose hiPSC derived cortical spheroids as multimodal neural interfaces across the 3D surfaces of these small tissue constructs. High-resolution, high-efficiency recording and stimulation can be achieved, as illustrated by the field potential recordings in Figure 17d,e. Various microelectronic components for thermal, optical, and electrochemical sensing and modulation can be included in a straightforward manner by exploiting traditional techniques in 2D nano/microfabrication (Figure 17f). Demonstrated examples include resistive Joule heaters (Au trace; 150 nm thick, 3 μm width, and 3 μm spacing, 300 Ω resistance, Figure 17g), blue μ -ILEDs (wavelength 470 nm, Figure 17h), and oxygen sensors (Pt black, $250 \times 300 \mu\text{m}^2$ area, $\sim 4 \mu\text{m}$ thick as the working electrode (WE); Au, $250 \times 300 \mu\text{m}^2$ area, 150 nm thick as CE; Ag/AgCl laminated electrode, $250 \times 300 \mu\text{m}^2$ area as RE, Figure 17i). As a demonstration of electrical modulation, applied voltage pulses (5–50 mV; 5 μs duration time) can modulate the electrophysiological behaviors of these cortical spheroids. As the amplitude of the potential increases from 0.3 mV ($V_{\text{app}} = 5 \text{ mV}$) to 1.3 mV ($V_{\text{app}} = 50 \text{ mV}$), the number of microelectrodes that respond to electrical stimulation increases from 13 electrodes to all of 24 electrodes in this platform. Fine Au serpentine features located on both sides of the cage structure can serve as thermal actuators and temperature sensors to activate or inhibit neural activity in a controlled manner. Increasing the temperature of the spheroid (43 $^\circ\text{C}$, $\Delta T = 6 \text{ }^\circ\text{C}$; 5 min) depresses cortical activity. Demonstrations of optogenetic control use integrated μ -ILEDs and hiPSC cortical spheroids 10 days after transfection of a channelrhodopsin actuator (ChR64). Optically (8.35 mW/mm²; 2 ms duration) evoked responses can be observed from all 25 electrodes across the surface of the spheroid with expected field potential traces. The potentiometric oxygen sensor monitors the concentration of oxygen (from 0 to 15%) in culture media surrounding the spheroid.⁵⁴

Mechanical measurements, of particular interest for the study of neuromuscular junctions, can also be important. As an example of a 3D interface capable of contractile force measurements, Figure 17j–l shows a 3D framework embedded with highly sensitive, microscale strain gauges (Cr/Au serpentine trace; 5 μm width; 10/100 nm thick) to quantify the contractile forces (up to 100 μN) in optogenetic skeletal muscle tissue (optogenetic C2C12 myoblasts; mixed with 30% Matrigel, thrombin, and fibrinogen). The ChR2-expressing transgenic muscle tissue manually integrates onto the 3D framework to allow measurements of the contractions in response to optical stimulation. Figure 17l, for instance, shows how the sensor readings increase in amplitude (from 30 to 80 μN) as the intensity of the optical stimulation increases (465 nm; from 1.5 to 11.5 mW/cm²). In addition, the active tensile force of the muscle ring is modulated with the addition of drugs (e.g., acetylcholine chloride, caffeine, and dantrolene) with the sensor readings monitoring those changes.³⁰⁹ Applications of



Mechanically Guided 3D Structures

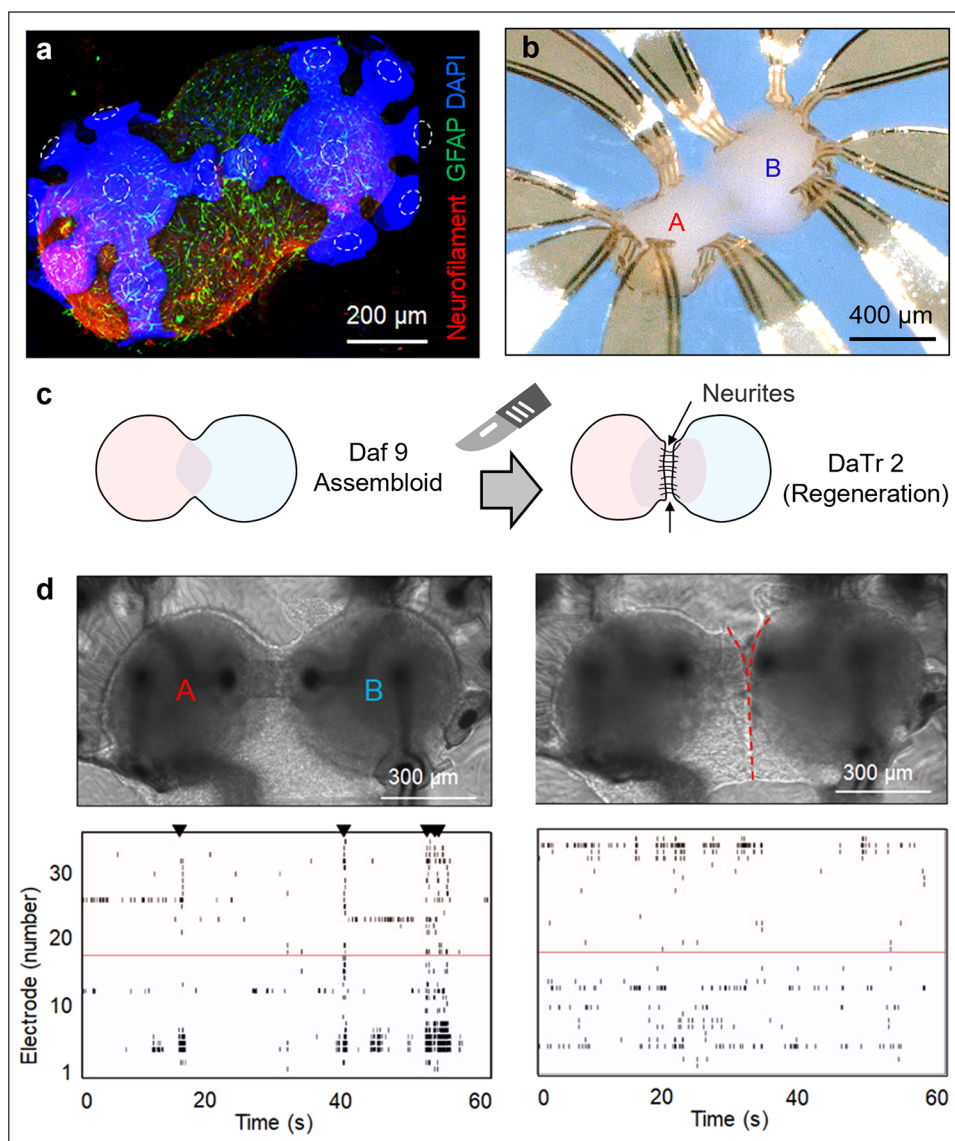


Figure 18. Mechanically guided multifunctional 3D framework for study of neuroregeneration. Confocal fluorescence microscopic image (a) and optical image (b) of an assembloid of two spheroids labeled with neurofilament (red), glial fibrillary acidic protein (green), Nissl bodies 797 (magenta), and DAPI nuclear stain (blue) enclosed in a 3D MMF labeled with an autofluorescence of the parylene-C (blue). (d) Illustrations, optical images, and raster plots before (left) and after transection (right) of the neurite bridge that joins the spheroids of this assembloid on day after fusion 9 (Daf 9) and recovery after transection on 2 days after transection 2 (DaTr 2).⁵⁴ Reproduced with permission from ref 54. Copyright 2021 American Association for the Advancement of Science.

related concepts to 3D tissue cultures using such device principles as neuromuscular organoids or engineered assembloids to model neuromuscular junctions are also of interest.

As an illustration of capabilities in creating and probing assembloids, 3D MMFs can be designed as frameworks to form deterministic, interconnected collections of spheroids, as in Figure 18, for the case of a model of neural injury and regeneration. Here, a complex 3D structure holds a pair of spheroids adjacent to one another to reveal processes associated with growth, transection, and regrowth of the neurite bridge that forms between them. Electrophysiological measurements using integrated electrodes show time-synchronized bursting behaviors as evidenced by raster plots between the two spheroids 2

days after fusion and functional neurite bridge formation. Just after transection, each part of the assembloid shows only its own individual, asynchronous neural activity. Two days after transection, however, synchronous firing and bursting resume with time frames similar to those associated with the initial formation of the bridge.⁵⁴ Combinations of this and previously introduced 3D neural interfaces have strong potential to provide access to unusual paradigms for *in vitro* human-related studies.

4. ADDITIONAL OPPORTUNITIES

As outlined in the preceding sections, organoids are 3D cultivated tissue models formed through schemes in stem cell and tissue engineering. Interest in these systems is in their ability

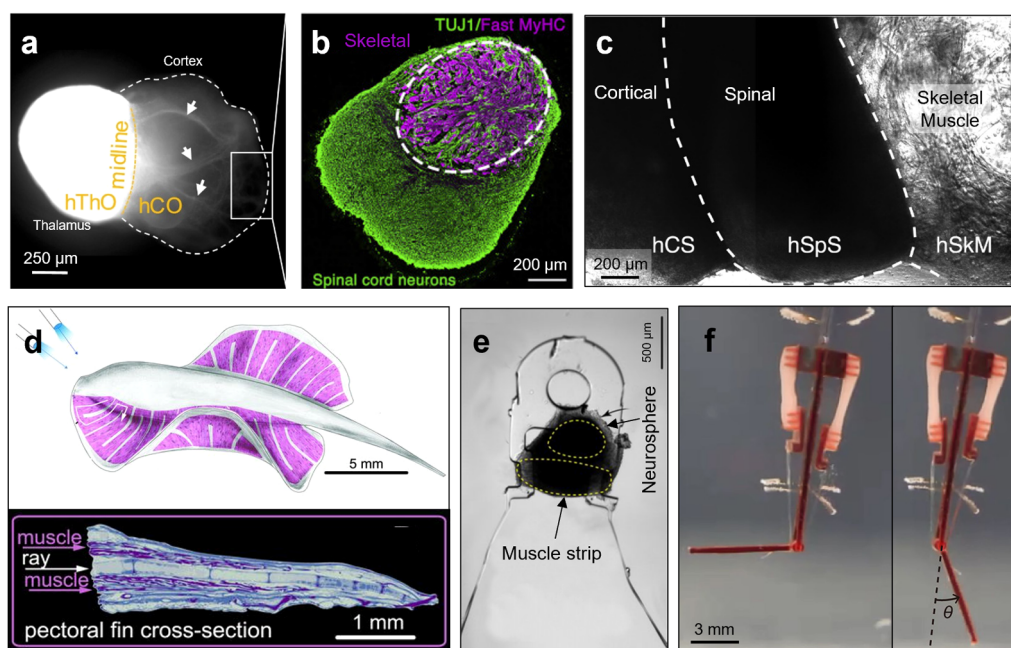


Figure 19. Three-dimensional multifunctional modulating and sensing interfaces for biohybrid robotic systems. (a) Epifluorescence image of thalamocortical assembloid with corticothalamic projections (hThCO generated from mCherry+ hThO and GFP+ hCO).³¹⁴ Reproduced with permission from ref 314. Copyright 2017 Elsevier. (b) Confocal fluorescence microscopic image of neuromuscular organoid showing the presence of neurons (TUJ1+ cells) that project axons into the organized skeletal muscle region labeled with myosin skeletal fast (Fast MyHC).³¹⁵ Reproduced with permission from ref 315. Copyright 2020 Elsevier. (c) Bright field image of cortico-spinal-muscle assembloid.³¹³ Reproduced with permission from ref 313. Copyright 2020 Elsevier. (d) Tissue-engineered soft-robotic manta ray (top) and musculoskeletal architecture of a robotic ray (bottom).³²² Reproduced with permission from ref 322. Copyright 2016 American Association for the Advancement of Science. (e) Bright field image of flagellum swimmer with neurosphere and muscle strip.³²³ Reproduced with permission from ref 323. Copyright 2019 National Academy of Sciences. (f) Biohybrid robot powered by an antagonistic pair of skeletal muscle tissues (left) and its contractile motion after applying electrical pulses (right).³²⁴ Reproduced with permission from ref 324. Copyright 2018 American Association for the Advancement of Science.

to express the characteristics of various human organs, at individual patient levels of specificity.³¹⁰ Particular emphasis is on brain organoids due to the diverse types of neurodevelopmental and neurodegenerative disease models that can be examined with region-specific prototypes (e.g., dorsal forebrain,⁴⁷ midbrain,³¹¹ hypothalamus,^{14,38} cerebellum³¹²). Assembloids, as described above, follow either from fusing multiple organoids based on specific brain regions known to functionally interact during development (e.g., dorsal forebrain with ventral forebrain^{38,313}) or from directly mixing multiple cell types to serve as biomimetic, physiologically relevant models of human tissues and organs^{314,315} (Figure 19a–c). As an important complement to purely optical methods, advances in materials approaches and 3D assembly techniques highlighted in this review allow for electrophysiological monitoring and neuromodulation to study the basic biology of these complex, heterogeneous 3D cultures.

An additional frontier area to complement such research activities focuses on engineering these 3D systems as soft robotic platforms with biohybrid control. Here, musculoskeletal architectures of tissue-engineered cardiac^{316–318} and skeletal^{319–321} engineered muscles integrate with elastomeric body structures that can support various other man-made structures and devices. Electrical or optical stimulation methods serve as the basis for programmable control of locomotion. Examples span various bioinspired designs (jellyfish,³¹⁷ manta ray,³²² and flagella³²³) that support steering and turning maneuvers (Figure 19d,e). In other cases, related strategies actuate the joints of robotic fingers, where multiple tissues integrate with a rigid framework and actuation occurs by selective contractions of

skeletal muscle tissues (Figure 19f).³²⁴ In these and other published strategies, control typically exploits far field illumination by external light sources^{322,323} or electric fields applied using remote electrodes,³²⁴ although with many constraints due to rough control options associated with far field modulation and limitations in terms of hydrolysis that can occur at the electrode that can interfere with the interface to the biosystem. The materials, devices, and structures summarized in previous sections, particularly those with 3D layouts, may form the basis for sophisticated sensing and modulating hardware for such biohybrid robotic systems.

5. CONCLUSIONS

A detailed understanding of the human body's complex central and peripheral nervous systems and associated metabolic processes is essential to identifying causes of neurological disease and in developing effective treatment approaches. Neural interfaces that can sense and modulate the behavior of cellular networks across a broad base of modalities, from electrical/electrochemical and optical to pharmacological, are essential enabling technologies for research in this area. When combined with 3D fabrication and assembly methods, these materials interfaces can engage with functional tissues over volumetric spaces in animal models or in hiPSC-based 3D biological systems such as spheroids, organoids, and engineered tissues. These platforms provide methodological advances for research purposes, and they also offer strong potential as the engineering basis for treating diseases and disorders.

In all cases, materials chemistry is critically important. Examples highlighted in this review span a remarkably wide

range, defined by (i) the mode of engagement at the neural interface, from electrical and electrochemical to optical and pharmacological; (ii) the structural properties, in terms of nano/microscale textures, features, and geometries; (iii) the physical properties, from flexible and stretchable to morphable; (iv) the chemical properties, from surface functionality to reactivity with surrounding biofluids, including mechanisms for bioresorption; and (v) the synergistic interaction with living cells, as biohybrids. The specific materials span carbon-based nanomaterials to conductive polymers, from elastomers to viscoelastic or viscoplastic materials, from noble metals to bioresorbable materials, semiconductors, nano/microstructures, functional hydrogels, and others. Assembly of these various materials into active devices and systems represents an additional aspect of neural interface engineering where chemistry in general, and interface chemistry in particular, is essential.

A particularly exciting area of emerging interest is in 3D structures formed using innovative approaches in ink/light-based 3D printing, self-rolling or folding induced by the residual stress between thin-film multilayers, and mechanically guided assembly based on compressive forces imparted by an elastomeric substrate. A broad diversity of examples appears in the recent literature, from arrays of filamentary penetrating probes to tissue-embedding electronics in open-mesh geometries, to 3D-printed, multimaterial frameworks, to self-rolled bioelectronics constructs and mechanically guided 3D architectures that support electrical, optical, chemical, and thermal interfaces for sensing and modulation.

While this review focuses primarily on the central nervous system, many of these same materials and techniques can support functional interfaces to the peripheral nervous system, as reported and reviewed elsewhere.^{325–328} In particular, cufflike interfaces that wrap around the sciatic or peroneal nerves as extraneural interfaces can be realized by methods of self-locking,³²⁹ self-rolling,²⁶⁹ self-healing,³³⁰ and morphing¹¹⁵ functions, while penetrating probes^{331,332} can act as interfascicular interfaces. Such interfaces demonstrated in animal models enable not only electrical monitoring³³³ and stimulation capabilities for nerve regeneration^{126,334} but also optogenetic stimulating functions^{197,333} and microfluidic channels for drug delivery,¹⁹⁷ as examples of multifunctionality.

Another set of interesting topics that lies outside of the scope of this review focuses on the use of the materials themselves, rather than materials in structures and devices, as neural interfaces. Here, nanoparticles, nanorods, and other forms of materials provide, when coupled with externally delivered sources of power based on magnetic fields, light, or ultrasound, various forms of neuromodulation. Examples include nanoparticles designed to support magnetothermal/optothermal mechanisms^{56,57} and sono-optical schemes.^{58,59} Powerful synergies may emerge from work in these directions and research on the approaches describes in this review, with particular promise in the context of 3D interfaces.

Despite much progress, challenges remain in translating these advances into the clinic for widespread use with human patients. Organs as complex as the brain require increased electrode density and resolution to engage with the level of sophistication that may be necessary to study and treat neurological disorders. Increasing the number of programmable sites for monitoring and modulating neural activity demands innovative engineering approaches and creative solutions in materials chemistry to minimize the invasiveness and maximize the stable operating lifetime. Managing foreign body responses represents one of the

most significant hurdles. Reactions of the immune system can lead to health risks, and biofouling can degrade signal quality and interface impedances, both with implications on long-term device viability. Miniaturized neuronlike interfacing modalities with nano/microstructured constituent materials that offer soft, tissue-compatible physical properties offer some promise in stable biotic–abiotic integration. Biohybrids could also have utility in this context. Optical interfaces may bypass some of the most daunting difficulties by physically separating the devices from the neural tissues. Bioresorbable platforms avoid long-term risks through natural elimination of engineering systems after a relevant operational time frame. Exploring these options in neural interface technology, particularly those that support 3D integration, sets a compelling direction for materials chemistry in service of efforts to reveal the secrets of the human brain, one of the most profound topics in modern scientific research.

AUTHOR INFORMATION

Corresponding Author

John A. Rogers — *Querrey Simpson Institute for Bioelectronics, Department of Biomedical Engineering, Department of Electrical Engineering and Computer Science, Department of Chemistry, Department of Mechanical Engineering, and Department of Neurological Surgery, Northwestern University, Evanston, Illinois 60208, United States; Department of Materials Science and Engineering, Northwestern University, Evanston, Illinois 60208, United States; orcid.org/0000-0002-2980-3961; Email: jrogers@northwestern.edu*

Authors

Yoonseok Park — *Querrey Simpson Institute for Bioelectronics, Northwestern University, Evanston, Illinois 60208, United States; orcid.org/0000-0002-1702-0986*

Ted S. Chung — *Querrey Simpson Institute for Bioelectronics and Department of Biomedical Engineering, Northwestern University, Evanston, Illinois 60208, United States*

Geumbee Lee — *Querrey Simpson Institute for Bioelectronics, Northwestern University, Evanston, Illinois 60208, United States*

Complete contact information is available at:
<https://pubs.acs.org/10.1021/acs.chemrev.1c00639>

Author Contributions

[○]Y.P., T.S.C., and G.L. contributed equally to this work.

Notes

The authors declare the following competing financial interest(s): J.A.R. is a co-founder of a company, NeuroLux, that builds patented wireless neurotechnology for the neuroscience research community.

Biographies

Yoonseok Park obtained a B.S. degree in 2006 and an M.S. degree in 2008 from Sungkyunkwan University and Seoul National University in materials sciences and engineering. From 2008 to 2013, he was a research engineer at LG Displays in South Korea. After 5 years in industry, he joined the Dresden Integrated center for Applied Physics and Photonic materials (IAPP) at Technische Universität Dresden in Germany and obtained his Ph.D. in physics in 2017. In 2018, he joined the Querrey Simpson Institute for Bioelectronics at Northwestern University as a postdoctoral research fellow supported by the German Research Foundation (DFG) with the aim of developing three-dimensional neural interfaces.

Ted S. Chung recently received his B.S. degree in 2021 from Northwestern University in biomedical engineering. He has been working as an undergraduate research associate at the Querrey Simpson Institute for Bioelectronics since 2018 and has been involved in projects regarding three-dimensional neural interfaces and sensors. He will be starting graduate school at Columbia University as a Guggenheim Fellow to explore electronic devices and systems based on two-dimensional materials.

Geumbee Lee received her B.S. degree in 2012 from Duksung Women's University in chemistry and her Ph.D. in 2019 from Korea University in nano-bio-information technology. She is currently a postdoctoral research fellow within the Querrey Simpson Institute for Bioelectronics at Northwestern University. Her research interests include wearable and implantable systems for energy and biomedical applications.

John A. Rogers obtained B.A. and B.S. degrees in chemistry and physics from the University of Texas—Austin, in 1989. From MIT, he received S.M. degrees in physics and in chemistry in 1992 and his Ph.D. degree in physical chemistry in 1995. From 1995 to 1997, Rogers was a Junior Fellow in the Harvard University Society of Fellows. He joined Bell Laboratories as a member of technical staff in the Condensed Matter Physics Research Department in 1997 and served as director of this department from the end of 2000 to 2002. He then spent 13 years on the faculty at University of Illinois, most recently as the Swanlund Chair Professor and Director of the Seitz Materials Research Laboratory. In 2016, he joined Northwestern University as the Louis Simpson and Kimberly Querrey Professor of Materials Science and Engineering, Biomedical Engineering, and Medicine, with affiliate appointments in Mechanical Engineering, Electrical and Computer Engineering, and Chemistry, where he is also Director of the Querrey Simpson Institute for Bioelectronics.

ACKNOWLEDGMENTS

This work was supported by the Querrey Simpson Institute for Bioelectronics at Northwestern University. Y.P. acknowledges support from the German Research Foundation (PA 3154/1-1). We thank Amay J. Bandodkar for insightful discussions.

REFERENCES

- (1) Williams, S. M.; White, L. E. *Neuroscience*, 6th ed.; Purves, D., Augustine, G. J., Fitzpatrick, D., Hall, W. C., LaMantia, A.-S., Mooney, R. D., Platt, M. L., White, L. E., Eds.; Oxford University Press: New York, 2013.
- (2) Silverthorn, D. *Human Physiology*, 5th ed.; Pearson: 2010.
- (3) Cosgrove, K. P.; Mazure, C. M.; Staley, J. K. Evolving Knowledge of Sex Differences in Brain Structure, Function, and Chemistry. *Biol. Psychiatry* **2007**, *62*, 847–855.
- (4) Poewe, W.; Seppi, K.; Tanner, C. M.; Halliday, G. M.; Brundin, P.; Volkman, J.; Schrag, A. E.; Lang, A. E. Parkinson Disease. *Nat. Rev. Dis. Prim.* **2017**, *3*, 1–21.
- (5) Hickey, P.; Stacy, M. Deep Brain Stimulation: A Paradigm Shifting Approach to Treat Parkinson's Disease. *Front. Neurosci.* **2016**, *10*, 173.
- (6) Kim, H.; Park, H. J. H. H. J.; Choi, H.; Chang, Y.; Park, H. J. H. H. J.; Shin, J.; Kim, J. J. J.; Lengner, C. J.; Lee, Y. K.; Kim, J. J. J. Modeling G2019S-LRRK2 Sporadic Parkinson's Disease in 3D Midbrain Organoids. *Stem Cell Rep.* **2019**, *12*, 518–531.
- (7) Soikkeli, R.; Partanen, J.; Soininen, H.; Pääkkönen, A.; Riekkinen, P. Slowing of EEG in Parkinson's Disease. *Electroencephalogr. Clin. Neurophysiol.* **1991**, *79*, 159–165.
- (8) Han, C. X.; Wang, J.; Yi, G. S.; Che, Y. Q. Investigation of EEG Abnormalities in the Early Stage of Parkinson's Disease. *Cogn. Neurodyn.* **2013**, *7*, 351–359.
- (9) Smith, M. A. ALZHEIMER DISEASE. *Int. Rev. Neurobiol.* **1998**, *42*, 1–54.

- (10) Cairns, D. M.; Rouleau, N.; Parker, R. N.; Walsh, K. G.; Gehrke, L.; Kaplan, D. L. A 3D Human Brain-like Tissue Model of Herpes-Induced Alzheimer's Disease. *Sci. Adv.* **2020**, *6*, eaay8828.
- (11) Lin, Y. T.; Seo, J.; Gao, F.; Feldman, H. M.; Wen, H. L.; Penney, J.; Cam, H. P.; Gjonneska, E.; Raja, W. K.; Cheng, J.; et al. APOE4 Causes Widespread Molecular and Cellular Alterations Associated with Alzheimer's Disease Phenotypes in Human iPSC-Derived Brain Cell Types. *Neuron* **2018**, *98*, 1141–1154.e7.
- (12) Cugola, F. R.; Fernandes, I. R.; Russo, F. B.; Freitas, B. C.; Dias, J. L. M.; Guimarães, K. P.; Benazzato, C.; Almeida, N.; Pignatari, G. C.; Romero, S.; et al. The Brazilian Zika Virus Strain Causes Birth Defects in Experimental Models. *Nature* **2016**, *534*, 267–271.
- (13) Garcez, P. P.; Loiola, E. C.; Madeiro da Costa, R.; Higa, L. M.; Trindade, P.; Delvecchio, R.; Nascimento, J. M.; Brindeiro, R.; Tanuri, A.; Rehen, S. K. Zika Virus Impairs Growth in Human Neurospheres and Brain Organoids. *Science* **2016**, *352*, 816–818.
- (14) Qian, X.; Nguyen, H. N. N.; Song, M. M. M.; Hadiono, C.; Ogden, S. C. C.; Hammack, C.; Yao, B.; Hamersky, G. R. R.; Jacob, F.; Zhong, C.; et al. Brain-Region-Specific Organoids Using Mini-Bioreactors for Modeling ZIKV Exposure. *Cell* **2016**, *165*, 1238–1254.
- (15) Carvalho, M. D. C. G.; Miranda-Filho, D. B.; van der Linden, V.; Sobral, P. F.; Ramos, R. C. F.; Rocha, M. A. W.; Cordeiro, M. T.; Alencar, S. P.; Nunes, M. L. Sleep EEG Patterns in Infants with Congenital Zika Virus Syndrome. *Clin. Neurophysiol.* **2017**, *128*, 204–214.
- (16) Ahn, S.; Jo, S.; Jun, S. B.; Lee, H. W.; Lee, S. Prediction of the Seizure Suppression Effect by Electrical Stimulation via a Computational Modeling Approach. *Front. Comput. Neurosci.* **2017**, *11*, 39.
- (17) Pun, R. Y. K.; Rolle, I. J.; LaSarge, C. L.; Hosford, B. E.; Rosen, J. M.; Uhl, J. D.; Schmeltzer, S. N.; Faulkner, C.; Bronson, S. L.; Murphy, B. L.; et al. Excessive Activation of MTOR in Postnatally Generated Granule Cells Is Sufficient to Cause Epilepsy. *Neuron* **2012**, *75*, 1022–1034.
- (18) Pfurtscheller, G.; Müller-Putz, G. R.; Scherer, R.; Neuper, C. Rehabilitation with Brain-Computer Interface Systems. *Computer (Long Beach, Calif.)* **2008**, *41*, 58–65.
- (19) Kuiken, T. A.; Miller, L. A.; Lipschutz, R. D.; Lock, B. A.; Stubblefield, K.; Marasco, P. D.; Zhou, P.; Dumanian, G. A. Targeted Reinnervation for Enhanced Prosthetic Arm Function in a Woman with a Proximal Amputation: A Case Study. *Lancet* **2007**, *369*, 371–380.
- (20) Brice, J.; McLellan, L. SUPPRESSION OF INTENTION TREMOR BY CONTINGENT DEEP-BRAIN STIMULATION. *Lancet* **1980**, *315*, 1221–1222.
- (21) Krauss, J. K.; Lipsman, N.; Aziz, T.; Boutet, A.; Brown, P.; Chang, J. W.; Davidson, B.; Grill, W. M.; Hariz, M. I.; Horn, A.; et al. Technology of Deep Brain Stimulation: Current Status and Future Directions. *Nat. Rev. Neurol.* **2021**, *17*, 75–87.
- (22) Dobkin, B. H. Strategies for Stroke Rehabilitation. *Lancet Neurol.* **2004**, *3*, 528–536.
- (23) Webster, B. R.; Celnik, P. A.; Cohen, L. G. Noninvasive Brain Stimulation in Stroke Rehabilitation. *NeuroRx* **2006**, *3*, 474–481.
- (24) Vunjak-Novakovic, G.; Bhatia, S.; Chen, C.; Hirschi, K. HeLiVa Platform: Integrated Heart-Liver-Vascular Systems for Drug Testing in Human Health and Disease. *Stem Cell Res. Ther.* **2013**, *4*, S8.
- (25) Jensen, J.; Hyllner, J.; Björquist, P. Human Embryonic Stem Cell Technologies and Drug Discovery. *J. Cell. Physiol.* **2009**, *219*, 513–519.
- (26) Sternecker, J. L.; Reinhardt, P.; Schöler, H. R. Investigating Human Disease Using Stem Cell Models. *Nat. Rev. Genet.* **2014**, *15*, 625–639.
- (27) Blau, H. M.; Daley, G. Q. Stem Cells in the Treatment of Disease. *N. Engl. J. Med.* **2019**, *380*, 1748–1760.
- (28) Singh, S. K.; Clarke, I. D.; Terasaki, M.; Bonn, V. E.; Hawkins, C.; Squire, J.; Dirks, P. B. Identification of a Cancer Stem Cell in Human Brain Tumors. *Cancer Res.* **2003**, *63*, 5821.
- (29) Bjerkvig, R.; Tysnes, B. B.; Aboody, K. S.; Najbauer, J.; Terzis, A. J. A. The Origin of the Cancer Stem Cell: Current Controversies and New Insights. *Nat. Rev. Cancer* **2005**, *5*, 899–904.
- (30) Chen, M.; Maimaitili, M.; Habekost, M.; Gill, K. P.; Mermet-Joret, N.; Nabavi, S.; Febbraro, F.; Denham, M. Rapid Generation of

Regionally Specified CNS Neurons by Sequential Patterning and Conversion of Human Induced Pluripotent Stem Cells. *Stem Cell Res.* **2020**, *48*, 101945.

(31) Bardy, C.; van den Hurk, M.; Kakaradov, B.; Erwin, J. A.; Jaeger, B. N.; Hernandez, R. V.; Eames, T.; Paucar, A. A.; Gorris, M.; Marchand, C.; et al. Predicting the Functional States of Human iPSC-Derived Neurons with Single-Cell RNA-Seq and Electrophysiology. *Mol. Psychiatry* **2016**, *21*, 1573–1588.

(32) Ronchi, S.; Buccino, A. P.; Prack, G.; Kumar, S. S.; Schröter, M.; Fiscella, M.; Hierlemann, A. Electrophysiological Phenotype Characterization of Human iPSC-Derived Neuronal Cell Lines by Means of High-Density Microelectrode Arrays. *Adv. Biol.* **2021**, *5*, 2000223.

(33) Shew, W. L.; Bellay, T.; Pleniz, D. Simultaneous Multi-Electrode Array Recording and Two-Photon Calcium Imaging of Neural Activity. *J. Neurosci. Methods* **2010**, *192*, 75–82.

(34) Trujillo, C. A.; Gao, R.; Negraes, P. D.; Gu, J.; Buchanan, J.; Preissl, S.; Wang, A.; Wu, W.; Haddad, G. G.; Chaim, I. A.; et al. Complex Oscillatory Waves Emerging from Cortical Organoids Model Early Human Brain Network Development. *Cell Stem Cell* **2019**, *25*, 558–569.e7.

(35) Peng, Y.; Mittermaier, F. X.; Planert, H.; Schneider, U. C.; Alle, H.; Geiger, J. R. P. High-Throughput Microcircuit Analysis of Individual Human Brains through next-Generation Multineuron Patch-Clamp. *eLife* **2019**, *8*, No. e48178.

(36) Gunhanlar, N.; Shpak, G.; van der Kroeg, M.; Gouty-Colomer, L. A.; Munshi, S. T.; Lendemeijer, B.; Ghazvini, M.; Dupont, C.; Hoogendijk, W. J. G.; Gribnau, J.; et al. A Simplified Protocol for Differentiation of Electrophysiologically Mature Neuronal Networks from Human Induced Pluripotent Stem Cells. *Mol. Psychiatry* **2018**, *23*, 1336–1344.

(37) Lancaster, M. A.; Knoblich, J. A. Organogenesis in a Dish: Modeling Development and Disease Using Organoid Technologies. *Science (Washington, DC, U. S.)* **2014**, *345*, 1247125.

(38) Xiang, Y.; Tanaka, Y.; Cakir, B.; Patterson, B.; Kim, K. Y.; Sun, P.; Kang, Y. J.; Zhong, M.; Liu, X.; Patra, P.; et al. hESC-Derived Thalamic Organoids Form Reciprocal Projections When Fused with Cortical Organoids. *Cell Stem Cell* **2019**, *24*, 487–497.e7.

(39) Yoon, S. J.; Elahi, L. S.; Paşca, A. M.; Marton, R. M.; Gordon, A.; Revah, O.; Miura, Y.; Walczak, E. M.; Holdgate, G. M.; Fan, H. C.; et al. Reliability of Human Cortical Organoid Generation. *Nat. Methods* **2019**, *16*, 75–78.

(40) Quadrato, G.; Nguyen, T.; Macosko, E. Z.; Sherwood, J. L.; Min Yang, S.; Berger, D. R.; Maria, N.; Scholvin, J.; Goldman, M.; Kinney, J. P.; et al. Cell Diversity and Network Dynamics in Photosensitive Human Brain Organoids. *Nature* **2017**, *545*, 48–53.

(41) Nakano, T.; Ando, S.; Takata, N.; Kawada, M.; Muguruma, K.; Sekiguchi, K.; Saito, K.; Yonemura, S.; Eiraku, M.; Sasai, Y. Self-Formation of Optic Cups and Storable Stratified Neural Retina from Human ESCs. *Cell Stem Cell* **2012**, *10*, 771–785.

(42) Eiraku, M.; Takata, N.; Ishibashi, H.; Kawada, M.; Sakakura, E.; Okuda, S.; Sekiguchi, K.; Adachi, T.; Sasai, Y. Self-Organizing Optic-Cup Morphogenesis in Three-Dimensional Culture. *Nature* **2011**, *472*, 51–58.

(43) Chen, Y. W.; Huang, S. X.; De Carvalho, A. L. R. T.; Ho, S. H.; Islam, M. N.; Volpi, S.; Notarangelo, L. D.; Ciancanelli, M.; Casanova, J. L.; Bhattacharya, J.; et al. A Three-Dimensional Model of Human Lung Development and Disease from Pluripotent Stem Cells. *Nat. Cell Biol.* **2017**, *19*, 542–549.

(44) Takasato, M.; Er, P. X.; Chiu, H. S.; Maier, B.; Baillie, G. J.; Ferguson, C.; Parton, R. G.; Wolvetang, E. J.; Roost, M. S.; De Sousa Lopes, S. M. C.; et al. Kidney Organoids from Human iPSCs Contain Multiple Lineages and Model Human Nephrogenesis. *Nature* **2015**, *526*, 564–568.

(45) Spence, J. R.; Mayhew, C. N.; Rankin, S. A.; Kuhar, M. F.; Vallance, J. E.; Tolle, K.; Hoskins, E. E.; Kalinichenko, V. V.; Wells, S. I.; Zorn, A. M.; et al. Directed Differentiation of Human Pluripotent Stem Cells into Intestinal Tissue in Vitro. *Nature* **2011**, *470*, 105–110.

(46) Lancaster, M. A.; Corsini, N. S.; Wolfinger, S.; Gustafson, E. H.; Phillips, A. W.; Burkard, T. R.; Otani, T.; Livesey, F. J.; Knoblich, J. A.

Guided Self-Organization and Cortical Plate Formation in Human Brain Organoids. *Nat. Biotechnol.* **2017**, *35*, 659–666.

(47) Paşca, A. M.; Sloan, S. A.; Clarke, L. E.; Tian, Y.; Makinson, C. D.; Huber, N.; Kim, C. H.; Park, J.-Y. Y.; O'Rourke, N. A.; Nguyen, K. D.; et al. Functional Cortical Neurons and Astrocytes from Human Pluripotent Stem Cells in 3D Culture. *Nat. Methods* **2015**, *12*, 671–678.

(48) Lancaster, M. A. Brain Organoids Get Vascularized. *Nat. Biotechnol.* **2018**, *36*, 407–408.

(49) Lancaster, M. A.; Renner, M.; Martin, C. A.; Wenzel, D.; Bicknell, L. S.; Hurler, M. E.; Homfray, T.; Penninger, J. M.; Jackson, A. P.; Knoblich, J. A. Cerebral Organoids Model Human Brain Development and Microcephaly. *Nature* **2013**, *501*, 373–379.

(50) Li, Q.; Nan, K.; Le Floch, P.; Lin, Z.; Sheng, H.; Blum, T. S.; Liu, J. Cyborg Organoids: Implantation of Nanoelectronics via Organogenesis for Tissue-Wide Electrophysiology. *Nano Lett.* **2019**, *19*, 5781–5789.

(51) Feiner, R.; Engel, L.; Fleischer, S.; Malki, M.; Gal, I.; Shapira, A.; Shacham-Diamand, Y.; Dvir, T. Engineered Hybrid Cardiac Patches with Multifunctional Electronics for Online Monitoring and Regulation of Tissue Function. *Nat. Mater.* **2016**, *15*, 679–685.

(52) Cools, J.; Jin, Q.; Yoon, E.; Alba Burbano, D.; Luo, Z.; Cuyper, D.; Callewaert, G.; Braeken, D.; Gracias, D. H. A Micropatterned Multielectrode Shell for 3D Spatiotemporal Recording from Live Cells. *Adv. Sci.* **2018**, *5*, 1700731.

(53) Kalmykov, A.; Huang, C.; Bliley, J.; Shiwarski, D.; Tashman, J.; Abdullah, A.; Rastogi, S. K.; Shukla, S.; Mataev, E.; Feinberg, A. W.; et al. Organ-on-a-Chip: Three-Dimensional Self-Rolled Biosensor Array for Electrical Interrogations of Human Electrogenic Spheroids. *Sci. Adv.* **2019**, *5*, eaax0729.

(54) Park, Y.; Franz, C. K.; Ryu, H.; Luan, H.; Cotton, K. Y.; Kim, J. U.; Chung, T. S.; Zhao, S.; Vazquez-Guardado, A.; Yang, D. S.; et al. Three-Dimensional, Multifunctional Neural Interfaces for Cortical Spheroids and Engineered Assembloids. *Sci. Adv.* **2021**, *7*, eab9153.

(55) Shin, H.; Jeong, S.; Lee, J. H.; Sun, W.; Choi, N.; Cho, I. J. 3D High-Density Microelectrode Array with Optical Stimulation and Drug Delivery for Investigating Neural Circuit Dynamics. *Nat. Commun.* **2021**, *12*, 1–18.

(56) Chen, R.; Romero, G.; Christiansen, M. G.; Mohr, A.; Anikeeva, P. Wireless Magnetothermal Deep Brain Stimulation. *Science (Washington, DC, U. S.)* **2015**, *347*, 1477–1480.

(57) Roet, M.; Heschem, S. A.; Jahanshahi, A.; Rutten, B. P. F.; Anikeeva, P. O.; Temel, Y. Progress in Neuromodulation of the Brain: A Role for Magnetic Nanoparticles? *Prog. Neurobiol.* **2019**, *177*, 1–14.

(58) Maresca, D.; Lakshmanan, A.; Abedi, M.; Bar-Zion, A.; Farhadi, A.; Lu, G. J.; Szablowski, J. O.; Wu, D.; Yoo, S.; Shapiro, M. G. Biomolecular Ultrasound and Sonogenetics. *Annu. Rev. Chem. Biomol. Eng.* **2018**, *9*, 229–252.

(59) Wu, X.; Zhu, X.; Chong, P.; Liu, J.; Andre, L. N.; Ong, K. S.; Brinson, K.; Mahdi, A. I.; Li, J.; Fenno, L. E.; et al. Sono-Optogenetics Facilitated by a Circulation-Delivered Rechargeable Light Source for Minimally Invasive Optogenetics. *Proc. Natl. Acad. Sci. U. S. A.* **2019**, *116*, 26332–26342.

(60) Jiang, Y.; Tian, B. Inorganic Semiconductor Biointerfaces. *Nat. Rev. Mater.* **2018**, *3*, 473–490.

(61) Schaumann, E. N.; Tian, B. Biological Interfaces, Modulation, and Sensing with Inorganic Nano-Bioelectronic Materials. *Small Methods* **2020**, *4*, 1900868.

(62) Fang, Y.; Meng, L.; Prominski, A.; Schaumann, E. N.; Seebald, M.; Tian, B. Recent Advances in Bioelectronics Chemistry. *Chem. Soc. Rev.* **2020**, *49*, 7978–8035.

(63) Chen, R.; Canales, A.; Anikeeva, P. Neural Recording and Modulation Technologies. *Nat. Rev. Mater.* **2017**, *2*, 1–16.

(64) Mickle, A. D.; Won, S. M.; Noh, K. N.; Yoon, J.; Meacham, K. W.; Xue, Y.; McIlvried, L. A.; Copits, B. A.; Samineni, V. K.; Crawford, K. E.; et al. A Wireless Closed-Loop System for Optogenetic Peripheral Neuromodulation. *Nature* **2019**, *565*, 361–365.

- (65) Rivnay, J.; Wang, H.; Fenno, L.; Deisseroth, K.; Malliaras, G. G. Next-Generation Probes, Particles, and Proteins for Neural Interfacing. *Sci. Adv.* **2017**, *3*, No. e1601649.
- (66) Cogan, S. F. Neural Stimulation and Recording Electrodes. *Annu. Rev. Biomed. Eng.* **2008**, *10*, 275–309.
- (67) Oka, H.; Shimono, K.; Ogawa, R.; Sugihara, H.; Taketani, M. A New Planar Multielectrode Array for Extracellular Recording: Application to Hippocampal Acute Slice. *J. Neurosci. Methods* **1999**, *93*, 61–67.
- (68) Weiland, J. D.; Anderson, D. J.; Humayun, M. S. In Vitro Electrical Properties for Iridium Oxide versus Titanium Nitride Stimulating Electrodes. *IEEE Trans. Biomed. Eng.* **2002**, *49*, 1574–1579.
- (69) Keefer, E. W.; Botterman, B. R.; Romero, M. I.; Rossi, A. F.; Gross, G. W. Carbon Nanotube Coating Improves Neuronal Recordings. *Nat. Nanotechnol.* **2008**, *3*, 434–439.
- (70) Khodagholy, D.; Gelinias, J. N.; Thesen, T.; Doyle, W.; Devinsky, O.; Malliaras, G. G.; Buzsáki, G. NeuroGrid: Recording Action Potentials from the Surface of the Brain. *Nat. Neurosci.* **2015**, *18*, 310–315.
- (71) Roncali, J. Conjugated Poly(Thiophenes): Synthesis, Functionalization, and Applications. *Chem. Rev.* **1992**, *92*, 711–738.
- (72) Sung, C.; Jeon, W.; Nam, K. S.; Kim, Y.; Butt, H.; Park, S. Multimaterial and Multifunctional Neural Interfaces: From Surface-Type and Implantable Electrodes to Fiber-Based Devices. *J. Mater. Chem. B* **2020**, *8*, 6624–6666.
- (73) Lu, Y.; Lyu, H.; Richardson, A. G.; Lucas, T. H.; Kuzum, D. Flexible Neural Electrode Array Based on Porous Graphene for Cortical Microstimulation and Sensing. *Sci. Rep.* **2016**, *6*, 1–9.
- (74) Vitale, F.; Summerson, S. R.; Aazhang, B.; Kemere, C.; Pasquali, M. Neural Stimulation and Recording with Bidirectional, Soft Carbon Nanotube Fiber Microelectrodes. *ACS Nano* **2015**, *9*, 4465–4474.
- (75) Rastogi, S. K.; Bilely, J.; Matino, L.; Garg, R.; Santoro, F.; Feinberg, A. W.; Cohen-Karni, T. Three-Dimensional Fuzzy Graphene Ultra-Microelectrodes for Subcellular Electrical Recordings. *Nano Res.* **2020**, *13*, 1444–1452.
- (76) Aqrave, Z.; Montgomery, J.; Travas-Sejdic, J.; Svirskis, D. Conducting Polymers for Neuronal Microelectrode Array Recording and Stimulation. *Sens. Actuators, B* **2018**, *257*, 753–765.
- (77) McCreery, R. L. Advanced Carbon Electrode Materials for Molecular Electrochemistry. *Chem. Rev.* **2008**, *108*, 2646–2687.
- (78) Yuk, H.; Lu, B.; Zhao, X. Hydrogel Bioelectronics. *Chem. Soc. Rev.* **2019**, *48*, 1642–1667.
- (79) Ferro, M. D.; Melosh, N. A. Electronic and Ionic Materials for Neurointerfaces. *Adv. Funct. Mater.* **2018**, *28*, 1704335.
- (80) Miller, K. J.; Hermes, D.; Staff, N. P. The Current State of ElectroCorticography-Based Brain-Computer Interfaces. *Neurosurg. Focus* **2020**, *49*, E2.
- (81) Boehler, C.; Stieglitz, T.; Asplund, M. Nanostructured Platinum Grass Enables Superior Impedance Reduction for Neural Microelectrodes. *Biomaterials* **2015**, *67*, 346–353.
- (82) Won, S. M.; Song, E.; Reeder, J. T.; Rogers, J. A. Emerging Modalities and Implantable Technologies for Neuromodulation. *Cell* **2020**, *181*, 115–135.
- (83) Nakamura, T.; Tsutsumi, N.; Juni, N.; Fujii, H. Improvement of Coupling-out Efficiency in Organic Electroluminescent Devices by Addition of a Diffusive Layer. *J. Appl. Phys.* **2004**, *96*, 6016.
- (84) Green, R. A.; Hassarati, R. T.; Bouchinet, L.; Lee, C. S.; Cheong, G. L. M.; Yu, J. F.; Dodds, C. W.; Suaning, G. J.; Poole-Warren, L. A.; Lovell, N. H. Substrate Dependent Stability of Conducting Polymer Coatings on Medical Electrodes. *Biomaterials* **2012**, *33*, 5875–5886.
- (85) Kozai, T. D. Y.; Catt, K.; Du, Z.; Na, K.; Srivannavit, O.; Haque, R. U. M.; Seymour, J.; Wise, K. D.; Yoon, E.; Cui, X. T. Chronic In Vivo Evaluation of PEDOT/CNT for Stable Neural Recordings. *IEEE Trans. Biomed. Eng.* **2016**, *63*, 111–119.
- (86) Min, J.; Sempionatto, J. R.; Teymourian, H.; Wang, J.; Gao, W. Wearable Electrochemical Biosensors in North America. *Biosens. Bioelectron.* **2021**, *172*, 112750.
- (87) Bucher, E. S.; Wightman, R. M. Electrochemical Analysis of Neurotransmitters. *Annu. Rev. Anal. Chem.* **2015**, *8*, 239–261.
- (88) Zhao, L.; Jiang, Y.; Wei, H.; Jiang, Y.; Ma, W.; Zheng, W.; Cao, A. M.; Mao, L. In Vivo Measurement of Calcium Ion with Solid-State Ion-Selective Electrode by Using Shelled Hollow Carbon Nanospheres as a Transducing Layer. *Anal. Chem.* **2019**, *91*, 4421–4428.
- (89) Bobacka, J.; Ivaska, A.; Lewenstam, A. Potentiometric Ion Sensors. *Chem. Rev.* **2008**, *108*, 329–351.
- (90) Nakatsuka, N.; Yang, K.-A.; Abendroth, J. M.; Cheung, K. M.; Xu, X.; Yang, H.; Zhao, C.; Zhu, B.; Rim, Y. S.; Yang, Y.; et al. Aptamer-Field-Effect Transistors Overcome Debye Length Limitations for Small-Molecule Sensing. *Science (Washington, DC, U. S.)* **2018**, *362*, 319–324.
- (91) Ribeiro, J. A.; Fernandes, P. M. V.; Pereira, C. M.; Silva, F. Electrochemical Sensors and Biosensors for Determination of Catecholamine Neurotransmitters: A Review. *Talanta* **2016**, *160*, 653–679.
- (92) Belaidi, F. S.; Civélas, A.; Castagnola, V.; Tsopela, A.; Mazenq, L.; Gros, P.; Launay, J.; Temple-Boyer, P. PEDOT-Modified Integrated Microelectrodes for the Detection of Ascorbic Acid, Dopamine and Uric Acid. *Sens. Actuators, B* **2015**, *214*, 1–9.
- (93) Ramirez, S.; Silva, N.; Oyarzun, M. P.; Pavez, J.; Silva, J. F. Gold Nanostructures on Self-Assembled Monolayers Activity for Epinephrine, Noradrenaline and Dopamine. *J. Electroanal. Chem.* **2017**, *799*, 349–357.
- (94) Eryigit, M.; Gür, E. P.; Hosseinpour, M.; Özer, T. Ö.; Doğan, H. Ö. Amperometric Detection of Dopamine on Prussian Blue Nanocube-Decorated Electrochemically Reduced Graphene Oxide Hybrid Electrode. *Mater. Today Proc.* **2021**, *46*, 6991.
- (95) Lee, J. S.; Oh, J.; Kim, S. G.; Jang, J. Highly Sensitive and Selective Field-Effect-Transistor Nonenzyme Dopamine Sensors Based on Pt/Conducting Polymer Hybrid Nanoparticles. *Small* **2015**, *11*, 2399–2406.
- (96) Tian, B.; Liu, J.; Dvir, T.; Jin, L.; Tsui, J. H.; Qing, Q.; Suo, Z.; Langer, R.; Kohane, D. S.; Lieber, C. M. Macroporous Nanowire Nanoelectronic Scaffolds for Synthetic Tissues. *Nat. Mater.* **2012**, *11*, 986–994.
- (97) Tian, B.; Cohen-Karni, T.; Qing, Q.; Duan, X.; Xie, P.; Lieber, C. M. Three-Dimensional, Flexible Nanoscale Field-Effect Transistors as Localized Bioprobes. *Science (Washington, DC, U. S.)* **2010**, *329*, 830–834.
- (98) Liu, J.; Fu, T. M.; Cheng, Z.; Hong, G.; Zhou, T.; Jin, L.; Duvvuri, M.; Jiang, Z.; Kruskal, P.; Xie, C.; et al. Syringe-Injectable Electronics. *Nat. Nanotechnol.* **2015**, *10*, 629–635.
- (99) Kim, D.-H.; Viventi, J.; Amsden, J. J.; Xiao, J.; Vigeland, L.; Kim, Y.-S.; Blanco, J. A.; Panilaitis, B.; Frechette, E. S.; Contreras, D.; et al. Dissolvable Films of Silk Fibroin for Ultrathin Conformal Bio-Integrated Electronics. *Nat. Mater.* **2010**, *9*, 511–517.
- (100) Qiang, Y.; Artoni, P.; Seo, K. J.; Culacli, S.; Hogan, V.; Zhao, X.; Zhong, Y.; Han, X.; Wang, P. M.; Lo, Y. K.; et al. Transparent Arrays of Bilayer-Nanomesh Microelectrodes for Simultaneous Electrophysiology and Two-Photon Imaging in the Brain. *Sci. Adv.* **2018**, *4*, eaat0626.
- (101) Kwon, K. Y.; Sirowatka, B.; Weber, A.; Li, W. Opto- μ ECoG Array: A Hybrid Neural Interface with Transparent μ ECoG Electrode Array and Integrated LEDs for Optogenetics. *IEEE Trans. Biomed. Circuits Syst.* **2013**, *7*, 593–600.
- (102) Park, D.-W.; Schendel, A. A.; Mikael, S.; Brodnick, S. K.; Richner, T. J.; Ness, J. P.; Hayat, M. R.; Atry, F.; Frye, S. T.; Pashaie, R.; et al. Graphene-Based Carbon-Layered Electrode Array Technology for Neural Imaging and Optogenetic Applications. *Nat. Commun.* **2014**, *5*, 1–11.
- (103) Vreeland, R. F.; Atcherley, C. W.; Russell, W. S.; Xie, J. Y.; Lu, D.; Laude, N. D.; Porreca, F.; Heien, M. L. Biocompatible PEDOT:Nafion Composite Electrode Coatings for Selective Detection of Neurotransmitters in Vivo. *Anal. Chem.* **2015**, *87*, 2600–2607.
- (104) Ferreira, N. R.; Ledo, A.; Laranjinha, J.; Gerhardt, G. A.; Barbosa, R. M. Simultaneous Measurements of Ascorbate and Glutamate in Vivo in the Rat Brain Using Carbon Fiber Nanocomposite

Sensors and Microbiosensor Arrays. *Bioelectrochemistry* **2018**, *121*, 142–150.

(105) Cao, Q.; Shin, M.; Lavrik, N. V.; Venton, B. J. 3D-Printed Carbon Nanoelectrodes for in Vivo Neurotransmitter Sensing. *Nano Lett.* **2020**, *20*, 6831–6836.

(106) Booth, M. A.; Gowers, S. A. N.; Hersey, M.; Samper, I. C.; Park, S.; Anikeeva, P.; Hashemi, P.; Stevens, M. M.; Boutelle, M. G. Fiber-Based Electrochemical Biosensors for Monitoring PH and Transient Neurometabolic Lactate. *Anal. Chem.* **2021**, *93*, 6646–6655.

(107) Tybrandt, K.; Khodagholy, D.; Dielacher, B.; Stauffer, F.; Renz, A. F.; Buzsáki, G.; Vörös, J. High-Density Stretchable Electrode Grids for Chronic Neural Recording. *Adv. Mater.* **2018**, *30*, 1706520.

(108) Yuk, H.; Lu, B.; Lin, S.; Qu, K.; Xu, J.; Luo, J.; Zhao, X. 3D Printing of Conducting Polymers. *Nat. Commun.* **2020**, *11*, 1–8.

(109) Afanasenkau, D.; Kalinina, D.; Lyakhovetskii, V.; Tondera, C.; Gorsky, O.; Moosavi, S.; Pavlova, N.; Merkulyeva, N.; Kalueff, A. V.; Minev, I. R.; et al. Rapid Prototyping of Soft Bioelectronic Implants for Use as Neuromuscular Interfaces. *Nat. Biomed. Eng.* **2020**, *4*, 1010–1022.

(110) Sim, K.; Ershad, F.; Zhang, Y.; Yang, P.; Shim, H.; Rao, Z.; Lu, Y.; Thukral, A.; Elgalad, A.; Xi, Y.; et al. An Epicardial Bioelectronic Patch Made from Soft Rubbery Materials and Capable of Spatiotemporal Mapping of Electrophysiological Activity. *Nat. Electron.* **2020**, *3*, 775–784.

(111) Yang, C.; Suo, Z. Hydrogel Ionotronics. *Nat. Rev. Mater.* **2018**, *3*, 125–142.

(112) Liu, Y.; Liu, J.; Chen, S.; Lei, T.; Kim, Y.; Niu, S.; Wang, H.; Wang, X.; Foudeh, A. M.; Tok, J. B. H.; et al. Soft and Elastic Hydrogel-Based Microelectronics for Localized Low-Voltage Neuromodulation. *Nat. Biomed. Eng.* **2019**, *3*, 58–68.

(113) Minev, I. R.; Musienko, P.; Hirsch, A.; Barraud, Q.; Wenger, N.; Moraud, E. M.; Gandar, J.; Capogrosso, M.; Milekovic, T.; Asboth, L.; et al. Electronic Dura Mater for Long-Term Multimodal Neural Interfaces. *Science (Washington, DC, U. S.)* **2015**, *347*, 159–163.

(114) Tringides, C. M.; Vachicouras, N.; de Lázaro, I.; Wang, H.; Trouillet, A.; Seo, B. R.; Elosegui-Artola, A.; Fallegger, F.; Shin, Y.; Casiraghi, C.; et al. Viscoelastic Surface Electrode Arrays to Interface with Viscoelastic Tissues. *Nat. Nanotechnol.* **2021**, *16*, 1019.

(115) Liu, Y.; Li, J.; Song, S.; Kang, J.; Tsao, Y.; Chen, S.; Mottini, V.; McConnell, K.; Xu, W.; Zheng, Y. Q.; et al. Morphing Electronics Enable Neuromodulation in Growing Tissue. *Nat. Biotechnol.* **2020**, *38*, 1031–1036.

(116) Wen, X.; Wang, B.; Huang, S.; Liu, T.; Lee, M. S.; Chung, P. S.; Chow, Y. T.; Huang, I. W.; Monbouquette, H. G.; Maidment, N. T.; et al. Flexible, Multifunctional Neural Probe with Liquid Metal Enabled, Ultra-Large Tunable Stiffness for Deep-Brain Chemical Sensing and Agent Delivery. *Biosens. Bioelectron.* **2019**, *131*, 37–45.

(117) Choi, Y.; Koo, J.; Rogers, J. A. Inorganic Materials for Transient Electronics in Biomedical Applications. *MRS Bull.* **2020**, *45*, 103–112.

(118) Lee, G.; Choi, Y. S.; Yoon, H.-J.; Rogers, J. A. Advances in Physicochemically Stimuli-Responsive Materials for On-Demand Transient Electronic Systems. *Matter* **2020**, *3*, 1031–1052.

(119) Chang, J. K.; Chang, H. P.; Guo, Q.; Koo, J.; Wu, C. I.; Rogers, J. A. Biodegradable Electronic Systems in 3D, Heterogeneously Integrated Formats. *Adv. Mater.* **2018**, *30*, 1704955.

(120) Hwang, S. W.; Huang, X.; Seo, J. H.; Song, J. K.; Kim, S.; Hage-Ali, S.; Chung, H. J.; Tao, H.; Omenetto, F. G.; Ma, Z.; et al. Materials for Bioresorbable Radio Frequency Electronics. *Adv. Mater.* **2013**, *25*, 3526–3531.

(121) Kang, S. K.; Murphy, R. K. J.; Hwang, S. W.; Lee, S. M. S. H. S. M.; Harburg, D. V.; Krueger, N. A.; Shin, J.; Gamble, P.; Cheng, H.; Yu, S.; et al. Bioresorbable Silicon Electronic Sensors for the Brain. *Nature* **2016**, *530*, 71–76.

(122) Jin, S. H.; Kang, S. K.; Cho, I. T.; Han, S. Y.; Chung, H. U.; Lee, D. J.; Shin, J.; Baek, G. W.; Kim, T. Il; Lee, J. H.; et al. Water-Soluble Thin Film Transistors and Circuits Based on Amorphous Indium-Gallium-Zinc Oxide. *ACS Appl. Mater. Interfaces* **2015**, *7*, 8268–8274.

(123) Kim, H. S.; Yang, S. M.; Jang, T. M.; Oh, N.; Kim, H. S.; Hwang, S. W. Bioresorbable Silicon Nanomembranes and Iron Catalyst

Nanoparticles for Flexible, Transient Electrochemical Dopamine Monitors. *Adv. Healthcare Mater.* **2018**, *7*, 1801071.

(124) Lee, J.; Cho, H. R.; Cha, G. D.; Seo, H.; Lee, S. T. S.; Park, C. K.; Kim, J. W. J.; Qiao, S.; Wang, L.; Kang, D.; et al. Flexible, Sticky, and Biodegradable Wireless Device for Drug Delivery to Brain Tumors. *Nat. Commun.* **2019**, *10*, 1–9.

(125) Yu, K. J.; Kuzum, D.; Hwang, S. W.; Kim, B. H.; Juul, H.; Kim, N. H.; Won, S. M.; Chiang, K.; Trumpis, M.; Richardson, A. G.; et al. Bioresorbable Silicon Electronics for Transient Spatiotemporal Mapping of Electrical Activity from the Cerebral Cortex. *Nat. Mater.* **2016**, *15*, 782–791.

(126) Koo, J.; MacEwan, M. R.; Kang, S. K.; Won, S. M.; Stephen, M.; Gamble, P.; Xie, Z.; Yan, Y.; Chen, Y. Y.; Shin, J.; et al. Wireless Bioresorbable Electronic System Enables Sustained Nonpharmacological Neuroregenerative Therapy. *Nat. Med.* **2018**, *24*, 1830–1836.

(127) Calabrese, V.; Mancuso, C.; Calvani, M.; Rizzarelli, E.; Butterfield, D. A.; Giuffrida Stella, A. M. Nitric Oxide in the Central Nervous System: Neuroprotection versus Neurotoxicity. *Nat. Rev. Neurosci.* **2007**, *8*, 766–775.

(128) Li, R.; Qi, H.; Ma, Y.; Deng, Y.; Liu, S.; Jie, Y.; Jing, J.; He, J.; Zhang, X.; Wheatley, L.; et al. A Flexible and Physically Transient Electrochemical Sensor for Real-Time Wireless Nitric Oxide Monitoring. *Nat. Commun.* **2020**, *11*, 1–11.

(129) Stieglitz, T.; Ruf, H.; Gross, M.; Schuettler, M.; Meyer, J. U. A Biohybrid System to Interface Peripheral Nerves after Traumatic Lesions: Design of a High Channel Sieve Electrode. *Biosens. Bioelectron.* **2002**, *17*, 685–696.

(130) Rochford, A. E.; Carnicer-Lombarte, A.; Curto, V. F.; Malliaras, G. G.; Barone, D. G. When Bio Meets Technology: Biohybrid Neural Interfaces. *Adv. Mater.* **2020**, *32*, 1903182.

(131) Shen, W.; Das, S.; Vitale, F.; Richardson, A.; Ananthkrishnan, A.; Struzyna, L. A.; Brown, D. P.; Song, N.; Ramkumar, M.; Lucas, T.; et al. Microfabricated Intracortical Extracellular Matrix-Microelectrodes for Improving Neural Interfaces. *Microsystems Nanoeng.* **2018**, *4*, 1–15.

(132) Serruya, M. D.; Harris, J. P.; Adewole, D. O.; Struzyna, L. A.; Burrell, J. C.; Nemes, A.; Petrov, D.; Kraft, R. H.; Chen, H. I.; Wolf, J. A.; et al. Engineered Axonal Tracts as “Living Electrodes” for Synaptic-Based Modulation of Neural Circuitry. *Adv. Funct. Mater.* **2018**, *28*, 1701183.

(133) Struzyna, L. A.; Katiyar, K.; Cullen, D. K. Living Scaffolds for Neuroregeneration. *Curr. Opin. Solid State Mater. Sci.* **2014**, *18*, 308–318.

(134) Adewole, D. O.; Struzyna, L. A.; Burrell, J. C.; Harris, J. P.; Nemes, A. D.; Petrov, D.; Kraft, R. H.; Chen, H. I.; Serruya, M. D.; Wolf, J. A.; et al. Development of Optically Controlled “Living Electrodes” with Long-Projecting Axon Tracts for a Synaptic Brain-Machine Interface. *Sci. Adv.* **2021**, *7*, 5347–5369.

(135) Abay, T. Y.; Kyriacou, P. A. Photoplethysmography for Blood Volumes and Oxygenation Changes during Intermittent Vascular Occlusions. *J. Clin. Monit. Comput.* **2018**, *32*, 447–455.

(136) Morone, K. A.; Neimat, J. S.; Roe, A. W.; Friedman, R. M. Review of Functional and Clinical Relevance of Intrinsic Signal Optical Imaging in Human Brain Mapping. *Neurophotonics* **2017**, *4*, No. 031220.

(137) Shen, Y.; Nasu, Y.; Shkolnikov, I.; Kim, A.; Campbell, R. E. Engineering Genetically Encoded Fluorescent Indicators for Imaging of Neuronal Activity: Progress and Prospects. *Neurosci. Res.* **2020**, *152*, 3–14.

(138) Zhu, A.; Qureshi, A. A.; Kozin, E. D.; Lee, D. J. Concepts in Neural Stimulation. *Otolaryngol. Clin. North Am.* **2020**, *53*, 31–43.

(139) Chen, G.; Song, F.; Xiong, X.; Peng, X. Fluorescent Nanosensors Based on Fluorescence Resonance Energy Transfer (FRET). *Ind. Eng. Chem. Res.* **2013**, *52*, 11228–11245.

(140) Chen, T. W.; Wardill, T. J.; Sun, Y.; Pulver, S. R.; Renninger, S. L.; Baohan, A.; Schreiter, E. R.; Kerr, R. A.; Orger, M. B.; Jayaraman, V.; et al. Ultrasensitive Fluorescent Proteins for Imaging Neuronal Activity. *Nature* **2013**, *499*, 295–300.

- (141) Stoeber, M.; Jullié, D.; Lobingier, B. T.; Laeremans, T.; Steyaert, J.; Schiller, P. W.; Manglik, A.; von Zastrow, M. A Genetically Encoded Biosensor Reveals Location Bias of Opioid Drug Action. *Neuron* **2018**, *98*, 963–976.e5.
- (142) Lin, M. Z.; Schnitzer, M. J. Genetically Encoded Indicators of Neuronal Activity. *Nat. Neurosci.* **2016**, *19*, 1142–1153.
- (143) Villette, V.; Chavarha, M.; Dimov, I. K.; Bradley, J.; Pradhan, L.; Mathieu, B.; Evans, S. W.; Chamberland, S.; Shi, D.; Yang, R.; et al. Ultrafast Two-Photon Imaging of a High-Gain Voltage Indicator in Awake Behaving Mice. *Cell* **2019**, *179*, 1590–1608.e23.
- (144) Piatkevich, K. D.; Bensussen, S.; Tseng, H. an; Shroff, S. N.; Lopez-Huerta, V. G.; Park, D.; Jung, E. E.; Shemesh, O. A.; Straub, C.; Gritton, H. J.; et al. Population Imaging of Neural Activity in Awake Behaving Mice. *Nature* **2019**, *574*, 413–417.
- (145) Abdelfattah, A. S.; Kawashima, T.; Singh, A.; Novak, O.; Liu, H.; Shuai, Y.; Huang, Y. C.; Campagnola, L.; Seeman, S. C.; Yu, J.; et al. Bright and Photostable Chemigenetic Indicators for Extended in Vivo Voltage Imaging. *Science (Washington, DC, U. S.)* **2019**, *365*, 699–704.
- (146) Marvin, J. S.; Shimoda, Y.; Magloire, V.; Leite, M.; Kawashima, T.; Jensen, T. P.; Kolb, I.; Knott, E. L.; Novak, O.; Podgorski, K.; et al. A Genetically Encoded Fluorescent Sensor for in Vivo Imaging of GABA. *Nat. Methods* **2019**, *16*, 763–770.
- (147) Patriarchi, T.; Cho, J. R.; Merten, K.; Howe, M. W.; Marley, A.; Xiong, W. H.; Folk, R. W.; Broussard, G. J.; Liang, R.; Jang, M. J.; et al. Ultrafast Neuronal Imaging of Dopamine Dynamics with Designed Genetically Encoded Sensors. *Science (Washington, DC, U. S.)* **2018**, DOI: 10.1126/science.aat4422.
- (148) Patriarchi, T.; Mohebi, A.; Sun, J.; Marley, A.; Liang, R.; Dong, C.; Puhger, K.; Mizuno, G. O.; Davis, C. M.; Wiltgen, B.; et al. An Expanded Palette of Dopamine Sensors for Multiplex Imaging in Vivo. *Nat. Methods* **2020**, *17*, 1147–1155.
- (149) Sun, F.; Zhou, J.; Dai, B.; Qian, T.; Zeng, J.; Li, X.; Zhuo, Y.; Zhang, Y.; Wang, Y.; Qian, C.; et al. Next-Generation GRAB Sensors for Monitoring Dopaminergic Activity in Vivo. *Nat. Methods* **2020**, *17*, 1156–1166.
- (150) Helassa, N.; Dürst, C. D.; Coates, C.; Kerruth, S.; Arif, U.; Schulze, C.; Wiegert, J. S.; Geeves, M.; Oertner, T. G.; Török, K. Ultrafast Glutamate Sensors Resolve High-Frequency Release at Schaffer Collateral Synapses. *Proc. Natl. Acad. Sci. U. S. A.* **2018**, *115*, 5594–5599.
- (151) Boyden, E. S.; Zhang, F.; Bamberg, E.; Nagel, G.; Deisseroth, K. Millisecond-Timescale, Genetically Targeted Optical Control of Neural Activity. *Nat. Neurosci.* **2005**, *8*, 1263–1268.
- (152) Nagel, G.; Szellas, T.; Huhn, W.; Kateriya, S.; Adeishvili, N.; Berthold, P.; Ollig, D.; Hegemann, P.; Bamberg, E. Channelrhodopsin-2, a Directly Light-Gated Cation-Selective Membrane Channel. *Proc. Natl. Acad. Sci. U. S. A.* **2003**, *100*, 13940–13945.
- (153) Pastrana, E. Optogenetics: Controlling Cell Function with Light. *Nat. Methods* **2011**, *8*, 24–25.
- (154) Vázquez-Guardado, A.; Yang, Y.; Bandodkar, A. J.; Rogers, J. A. Recent Advances in Neurotechnologies with Broad Potential for Neuroscience Research. *Nat. Neurosci.* **2020**, *23*, 1522–1536.
- (155) Grienberger, C.; Konnerth, A. Imaging Calcium in Neurons. *Neuron* **2012**, *73*, 862–885.
- (156) Skocek, O.; Nöbauer, T.; Weilguny, L.; Martinez Traub, F.; Xia, C. N.; Molodtsov, M. I.; Grama, A.; Yamagata, M.; Aharoni, D.; Cox, D. D.; et al. High-Speed Volumetric Imaging of Neuronal Activity in Freely Moving Rodents. *Nat. Methods* **2018**, *15*, 429–432.
- (157) Zong, W.; Wu, R.; Li, M.; Hu, Y.; Li, Y.; Li, J.; Rong, H.; Wu, H.; Xu, Y.; Lu, Y.; et al. Fast High-Resolution Miniature Two-Photon Microscopy for Brain Imaging in Freely Behaving Mice. *Nat. Methods* **2017**, *14*, 713–719.
- (158) Pisanello, F.; Sileo, L.; Oldenburg, I. A.; Pisanello, M.; Martiradonna, L.; Assad, J. A.; Sabatini, B. L.; De Vittorio, M. Multipoint-Emitting Optical Fibers for Spatially Addressable in Vivo Optogenetics. *Neuron* **2014**, *82*, 1245–1254.
- (159) Segev, E.; Reimer, J.; Moreaux, L. C.; Fowler, T. M.; Chi, D.; Sacher, W. D.; Lo, M.; Deisseroth, K.; Tolias, A. S.; Faraon, A.; et al. Patterned Photostimulation via Visible-Wavelength Photonic Probes for Deep Brain Optogenetics. *Neurophotonics* **2017**, *4*, 1.
- (160) Kim, T. Il; Jung, Y. H.; Song, J.; Kim, D.; Li, Y.; Kim, H. S.; Song, I. S.; Wierer, J. J.; Pao, H. A.; Huang, Y.; et al. High-Efficiency, Microscale GaN Light-Emitting Diodes and Their Thermal Properties on Unusual Substrates. *Small* **2012**, *8*, 1643–1649.
- (161) Wu, F.; Stark, E.; Ku, P. C.; Wise, K. D.; Buzsáki, G.; Yoon, E. Monolithically Integrated MLEDs on Silicon Neural Probes for High-Resolution Optogenetic Studies in Behaving Animals. *Neuron* **2015**, *88*, 1136–1148.
- (162) Kim, T. - i.; McCall, J. G.; Jung, Y. H.; Huang, X.; Siuda, E. R.; Li, Y.; Song, J.; Song, Y. M.; Pao, H. A.; Kim, R.-H.; et al. Injectable, Cellular-Scale Optoelectronics with Applications for Wireless Optogenetics. *Science (Washington, DC, U. S.)* **2013**, *340*, 211–216.
- (163) Lee, J.; Parker, K. E.; Kawakami, C.; Kim, J. R.; Qazi, R.; Yea, J.; Zhang, S.; Kim, C. Y.; Bilbily, J.; Xiao, J.; et al. Rapidly Customizable, Scalable 3D-Printed Wireless Optogenetic Probes for Versatile Applications in Neuroscience. *Adv. Funct. Mater.* **2020**, *30*, 2004285.
- (164) Zhao, Y.; Liu, C.; Liu, Z.; Luo, W.; Li, L.; Cai, X.; Liang, D.; Su, Y.; Ding, H.; Wang, Q.; et al. Wirelessly Operated, Implantable Optoelectronic Probes for Optogenetics in Freely Moving Animals. *IEEE Trans. Electron Devices* **2019**, *66*, 785–792.
- (165) Park, S. Il; Brenner, D. S.; Shin, G.; Morgan, C. D.; Copits, B. A.; Chung, H. U.; Pullen, M. Y.; Noh, K. N.; Davidson, S.; Oh, S. J.; et al. Soft, Stretchable, Fully Implantable Miniaturized Optoelectronic Systems for Wireless Optogenetics. *Nat. Biotechnol.* **2015**, *33*, 1280–1286.
- (166) Shin, G.; Gomez, A. M.; Al-Hasani, R.; Jeong, Y. R.; Kim, J. J. K. J.; Xie, Z.; Banks, A.; Lee, S. M. H. M.; Han, S. Y.; Yoo, C. J.; et al. Flexible Near-Field Wireless Optoelectronics as Subdermal Implants for Broad Applications in Optogenetics. *Neuron* **2017**, *93*, S09–S21.e3.
- (167) Kim, J.; Banks, A.; Xie, Z.; Heo, S. Y.; Gutruf, P.; Lee, J. W.; Xu, S.; Jang, K. I.; Liu, F.; Brown, G.; et al. Miniaturized Flexible Electronic Systems with Wireless Power and Near-Field Communication Capabilities. *Adv. Funct. Mater.* **2015**, *25*, 4761–4767.
- (168) Kim, J.; Banks, A.; Cheng, H.; Xie, Z.; Xu, S.; Jang, K. I.; Lee, J. W.; Liu, Z.; Gutruf, P.; Huang, X.; et al. Epidermal Electronics with Advanced Capabilities in Near-Field Communication. *Small* **2015**, *11*, 906–912.
- (169) Gutruf, P.; Krishnamurthi, V.; Vázquez-Guardado, A.; Xie, Z.; Banks, A.; Su, C. J.; Xu, Y.; Haney, C. R.; Waters, E. A.; Kandala, I.; et al. Fully Implantable Optoelectronic Systems for Battery-Free, Multimodal Operation in Neuroscience Research. *Nat. Electron.* **2018**, *1*, 652–660.
- (170) Yang, Y.; Wu, M.; Vázquez-Guardado, A.; Wegener, A. J.; Grajales-Reyes, J. G.; Deng, Y.; Wang, T.; Avila, R.; Moreno, J. A.; Minkowicz, S.; et al. Wireless Multilateral Devices for Optogenetic Studies of Individual and Social Behaviors. *Nat. Neurosci.* **2021**, *24*, 1035–1045.
- (171) Lacour, S. P.; Courtine, G.; Guck, J. Materials and Technologies for Soft Implantable Neuroprostheses. *Nat. Rev. Mater.* **2016**, *1*, 16063.
- (172) Loke, G.; Yan, W.; Khudiyev, T.; Noel, G.; Fink, Y. Recent Progress and Perspectives of Thermally Drawn Multimaterial Fiber Electronics. *Adv. Mater.* **2020**, *32*, 1904911.
- (173) Lu, C.; Park, S.; Richner, T. J.; Derry, A.; Brown, I.; Hou, C.; Rao, S.; Kang, J.; Moritz, C. T.; Fink, Y.; et al. Flexible and Stretchable Nanowire-Coated Fibers for Optoelectronic Probing of Spinal Cord Circuits. *Sci. Adv.* **2017**, *3*, No. e1600955.
- (174) Wang, L. L.; Zhong, C.; Ke, D.; Ye, F.; Tu, J.; Wang, L. L.; Lu, Y. Ultrasoft and Highly Stretchable Hydrogel Optical Fibers for In Vivo Optogenetic Modulations. *Adv. Opt. Mater.* **2018**, *6*, 1800427.
- (175) Park, S.; Yuk, H.; Zhao, R.; Yim, Y. S.; Woldeghiebril, E. W.; Kang, J.; Canales, A.; Fink, Y.; Choi, G. B.; Zhao, X.; et al. Adaptive and Multifunctional Hydrogel Hybrid Probes for Long-Term Sensing and Modulation of Neural Activity. *Nat. Commun.* **2021**, *12*, 3435.
- (176) Applegate, M. B.; Perotto, G.; Kaplan, D. L.; Omenetto, F. G. Biocompatible Silk Step-Index Optical Waveguides. *Biomed. Opt. Express* **2015**, *6*, 4221.

- (177) Shan, D.; Zhang, C.; Kalaba, S.; Mehta, N.; Kim, G. B.; Liu, Z.; Yang, J. Flexible Biodegradable Citrate-Based Polymeric Step-Index Optical Fiber. *Biomaterials* **2017**, *143*, 142–148.
- (178) Fu, R.; Luo, W.; Nazempour, R.; Tan, D.; Ding, H.; Zhang, K.; Yin, L.; Guan, J.; Sheng, X. Implantable and Biodegradable Poly(L-Lactic Acid) Fibers for Optical Neural Interfaces. *Adv. Opt. Mater.* **2018**, *6*, 1700941.
- (179) Bai, W.; Shin, J.; Fu, R.; Kandela, I.; Lu, D.; Ni, X.; Park, Y.; Liu, Z.; Hang, T.; Wu, D.; et al. Bioresorbable Photonic Devices for the Spectroscopic Characterization of Physiological Status and Neural Activity. *Nat. Biomed. Eng.* **2019**, *3*, 644–654.
- (180) Shim, J.-S.; Rogers, J. A.; Kang, S.-K. Physically Transient Electronic Materials and Devices. *Mater. Sci. Eng., R* **2021**, *145*, 100624.
- (181) Feng, J.; Jiang, Q.; Rogin, P.; De Oliveira, P. W.; Del Campo, A. Printed Soft Optical Waveguides of PLA Copolymers for Guiding Light into Tissue. *ACS Appl. Mater. Interfaces* **2020**, *12*, 20287–20294.
- (182) Lu, D.; Liu, T. L.; Chang, J. K.; Peng, D.; Zhang, Y.; Shin, J.; Hang, T.; Bai, W.; Yang, Q.; Rogers, J. A. Transient Light-Emitting Diodes Constructed from Semiconductors and Transparent Conductors That Biodegrade Under Physiological Conditions. *Adv. Mater.* **2019**, *31*, 1902739.
- (183) Thiel, C. M.; Henson, R. N. A.; Morris, J. S.; Friston, K. J.; Dolan, R. J. Pharmacological Modulation of Behavioral and Neuronal Correlates of Repetition Priming. *J. Neurosci.* **2001**, *21*, 6846–6852.
- (184) Iannetti, G. D.; Zambreau, L.; Wise, R. G.; Buchanan, T. J.; Huggins, J. P.; Smart, T. S.; Vennart, W.; Tracey, I. Pharmacological Modulation of Pain-Related Brain Activity during Normal and Central Sensitization States in Humans. *Proc. Natl. Acad. Sci. U. S. A.* **2005**, *102*, 18195–18200.
- (185) Banghart, M. R.; Sabatini, B. L. Photoactivatable Neuropeptides for Spatiotemporally Precise Delivery of Opioids in Neural Tissue. *Neuron* **2012**, *73*, 249–259.
- (186) Ramadi, K. B.; Cima, M. J. Materials and Devices for Micro-Invasive Neural Interfacing. *MRS Adv.* **2019**, *4*, 2805–2816.
- (187) Sim, J. Y.; Haney, M. P.; Park, S. II; McCall, J. G.; Jeong, J.-W. Microfluidic Neural Probes: In Vivo Tools for Advancing Neuroscience. *Lab Chip* **2017**, *17*, 1406–1435.
- (188) Chappel, E. Implantable Drug Delivery Devices. In *Drug Delivery Devices and Therapeutic Systems*; Elsevier: 2021; pp 129–156. DOI: 10.1016/B978-0-12-819838-4.00001-8.
- (189) Vadalouca, A.; Raptis, E.; Moka, E.; Zis, P.; Sykioti, P.; Siafaka, I. Pharmacological Treatment of Neuropathic Cancer Pain: A Comprehensive Review of the Current Literature. *Pain Pract.* **2012**, *12*, 219–251.
- (190) Himmerich, H.; Kan, C.; Au, K.; Treasure, J. Pharmacological Treatment of Eating Disorders, Comorbid Mental Health Problems, Malnutrition and Physical Health Consequences. *Pharmacol. Ther.* **2021**, *217*, 107667.
- (191) Chefer, V. I.; Thompson, A. C.; Zapata, A.; Shippenberg, T. S. Overview of Brain Microdialysis. *Curr. Protoc. Neurosci.* **2009**, *47*, 7–8.
- (192) Raman, R.; Rousseau, E. B.; Wade, M.; Tong, A.; Cotler, M. J.; Kuang, J.; Lugo, A. A.; Zhang, E.; Graybiel, A. M.; White, F. M.; et al. Platform for Micro-Invasive Membrane-Free Biochemical Sampling of Brain Interstitial Fluid. *Sci. Adv.* **2020**, *6*, eabb0657.
- (193) Dagdeviren, C.; Ramadi, K. B.; Joe, P.; Spencer, K.; Schwerdt, H. N.; Shimazu, H.; Delcasso, S.; Amemori, K. I.; Nunez-Lopez, C.; Graybiel, A. M.; et al. Miniaturized Neural System for Chronic, Local Intracerebral Drug Delivery. *Sci. Transl. Med.* **2018**, *10*, 2742.
- (194) Ramadi, K. B.; Dagdeviren, C.; Spencer, K. C.; Joe, P.; Cotler, M.; Rousseau, E.; Nunez-Lopez, C.; Graybiel, A. M.; Langer, R.; Cima, M. J. Focal, Remote-Controlled, Chronic Chemical Modulation of Brain Microstructures. *Proc. Natl. Acad. Sci. U. S. A.* **2018**, *115*, 7254–7259.
- (195) Cotler, M. J.; Rousseau, E. B.; Ramadi, K. B.; Fang, J.; Graybiel, A. M.; Langer, R.; Cima, M. J. Steerable Microinvasive Probes for Localized Drug Delivery to Deep Tissue. *Small* **2019**, *15*, 1901459.
- (196) Zhang, Y.; Castro, D. C.; Han, Y.; Wu, Y.; Guo, H.; Weng, Z.; Xue, Y.; Ausrá, J.; Wang, X.; Li, R.; et al. Battery-Free, Lightweight, Injectable Microsystem for in Vivo Wireless Pharmacology and Optogenetics. *Proc. Natl. Acad. Sci. U. S. A.* **2019**, *116*, 21427–21437.
- (197) Zhang, Y.; Mickle, A. D.; Gutruf, P.; McIlvried, L. A.; Guo, H.; Wu, Y.; Golden, J. P.; Xue, Y.; Grajales-Reyes, J. G.; Wang, X.; et al. Battery-Free, Fully Implantable Optofluidic Cuff System for Wireless Optogenetic and Pharmacological Neuromodulation of Peripheral Nerves. *Sci. Adv.* **2019**, *5*, eaaw5296.
- (198) Koo, J.; Kim, S. B.; Choi, Y. S.; Xie, Z.; Bandodkar, A. J.; Khalifeh, J.; Yan, Y.; Kim, H.; Pezhouh, M. K.; Doty, K.; et al. Wirelessly Controlled, Bioresorbable Drug Delivery Device with Active Valves That Exploit Electrochemically Triggered Crevice Corrosion. *Sci. Adv.* **2020**, *6*, 20.
- (199) Van Der Wal, S. E. I.; Van Den Heuvel, S. A. S.; Radema, S. A.; Van Berkum, B. F. M.; Vaneker, M.; Steegers, M. A. H.; Scheffer, G. J.; Vissers, K. C. P. The in Vitro Mechanisms and in Vivo Efficacy of Intravenous Lidocaine on the Neuroinflammatory Response in Acute and Chronic Pain. *Eur. J. Pain (United Kingdom)* **2016**, *20*, 655–674.
- (200) Shin, H.; Son, Y.; Chae, U.; Kim, J.; Choi, N.; Lee, H. J.; Woo, J.; Cho, Y.; Yang, S. H.; Lee, C. J.; et al. Multifunctional Multi-Shank Neural Probe for Investigating and Modulating Long-Range Neural Circuits in Vivo. *Nat. Commun.* **2019**, *10*, 1–11.
- (201) Park, S.; Guo, Y.; Jia, X.; Choe, H. K.; Grena, B.; Kang, J.; Park, J.; Lu, C.; Canales, A.; Chen, R.; et al. One-Step Optogenetics with Multifunctional Flexible Polymer Fibers. *Nat. Neurosci.* **2017**, *20*, 612–619.
- (202) Canales, A.; Jia, X.; Froriep, U. P.; Koppes, R. A.; Tringides, C. M.; Selvidge, J.; Lu, C.; Hou, C.; Wei, L.; Fink, Y.; et al. Multifunctional Fibers for Simultaneous Optical, Electrical and Chemical Interrogation of Neural Circuits in Vivo. *Nat. Biotechnol.* **2015**, *33*, 277–284.
- (203) Jeong, J. W.; McCall, J. G.; Shin, G.; Zhang, Y.; Al-Hasani, R.; Kim, M.; Li, S.; Sim, J. Y.; Jang, K. I.; Shi, Y.; et al. Wireless Optofluidic Systems for Programmable In Vivo Pharmacology and Optogenetics. *Cell* **2015**, *162*, 662–674.
- (204) Liu, C.; Zhao, Y.; Cai, X.; Xie, Y.; Wang, T.; Cheng, D.; Li, L.; Li, R.; Deng, Y.; Ding, H.; et al. A Wireless, Implantable Optoelectrochemical Probe for Optogenetic Stimulation and Dopamine Detection. *Microsystems Nanoeng.* **2020**, *6*, 64.
- (205) Lu, L.; Gutruf, P.; Xia, L.; Bhatti, D. L.; Wang, X.; Vazquez-Guardado, A.; Ning, X.; Shen, X.; Sang, T.; Ma, R.; et al. Wireless Optoelectronic Photometers for Monitoring Neuronal Dynamics in the Deep Brain. *Proc. Natl. Acad. Sci. U. S. A.* **2018**, *115*, E1374–E1383.
- (206) Ueki, H.; Wang, I.-H.; Zhao, D.; Gunzer, M.; Kawaoka, Y. Multicolor Two-Photon Imaging of in Vivo Cellular Pathophysiology upon Influenza Virus Infection Using the Two-Photon IMPRESS. *Nat. Protoc.* **2020**, *15*, 1041–1065.
- (207) Yamaguchi, K.; Kitamura, R.; Kawakami, R.; Otomo, K.; Nemoto, T. In Vivo Two-Photon Microscopic Observation and Ablation in Deeper Brain Regions Realized by Modifications of Excitation Beam Diameter and Immersion Liquid. *PLoS One* **2020**, *15*, No. e0237230.
- (208) Wang, T.; Ouzounov, D. G.; Wu, C.; Horton, N. G.; Zhang, B.; Wu, C. H.; Zhang, Y.; Schnitzer, M. J.; Xu, C. Three-Photon Imaging of Mouse Brain Structure and Function through the Intact Skull. *Nat. Methods* **2018**, *15*, 789–792.
- (209) Hontani, Y.; Xia, F.; Xu, C. Multicolor Three-Photon Fluorescence Imaging with Single-Wavelength Excitation Deep in Mouse Brain. *Sci. Adv.* **2021**, *7*, 3531–3548.
- (210) Kollo, M.; Racz, R.; Hanna, M.-E.; Obaid, A.; Angle, M. R.; Wray, W.; Kong, Y.; Müller, J.; Hierlemann, A.; Melosh, N. A.; et al. CHIME: CMOS-Hosted in Vivo Microelectrodes for Massively Scalable Neuronal Recordings. *Front. Neurosci.* **2020**, *14*, 834.
- (211) Obaid, A.; Hanna, M.-E.; Wu, Y.-W.; Kollo, M.; Racz, R.; Angle, M. R.; Müller, J.; Brackbill, N.; Wray, W.; Franke, F.; et al. Massively Parallel Microwire Arrays Integrated with CMOS Chips for Neural Recording. *Sci. Adv.* **2020**, *6*, eaay2789.
- (212) Steinmetz, N. A.; Aydin, C.; Lebedeva, A.; Okun, M.; Pachitariu, M.; Bauza, M.; Beau, M.; Bhagat, J.; Böhm, C.; Broux, M.; et al. Neuropixels 2.0: A Miniaturized High-Density Probe for Stable, Long-

Term Brain Recordings. *Science (Washington, DC, U. S.)* **2021**, DOI: 10.1126/science.abf4588.

(213) Musk, E.; Neuralink. An Integrated Brain-Machine Interface Platform with Thousands of Channels. *J. Med. Internet Res.* **2019**, *21*, e16194.

(214) Yang, X.; Zhou, T.; ZWang, T. J.; Hong, G.; Zhao, Y.; Viveros, R. D.; Fu, T. M.; Gao, T.; Lieber, C. M. Bioinspired Neuron-like Electronics. *Nat. Mater.* **2019**, *18*, 510–517.

(215) Jun, J. J.; Steinmetz, N. A.; Siegle, J. H.; Denman, D. J.; Bauza, M.; Barbarits, B.; Lee, A. K.; Anastassiou, C. A.; Andrei, A.; Aydin, Ç.; et al. Fully Integrated Silicon Probes for High-Density Recording of Neural Activity. *Nature* **2017**, *551*, 232–236.

(216) Sucher, N. J.; Deitcher, D. L. PCR and Patch-Clamp Analysis of Single Neurons. *Neuron* **1995**, *14*, 1095–1100.

(217) Müller, J.; Ballini, M.; Livi, P.; Chen, Y.; Radivojevic, M.; Shadmani, A.; Viswam, V.; Jones, I. L.; Fiscella, M.; Diggelmann, R.; et al. High-Resolution CMOS MEA Platform to Study Neurons at Subcellular, Cellular, and Network Levels. *Lab Chip* **2015**, *15*, 2767–2780.

(218) Abbott, J.; Ye, T.; Ham, D.; Park, H. Optimizing Nanoelectrode Arrays for Scalable Intracellular Electrophysiology. *Acc. Chem. Res.* **2018**, *51*, 600–608.

(219) Robinson, J. T.; Jorgolli, M.; Shalek, A. K.; Yoon, M. H.; Gertner, R. S.; Park, H. Vertical Nanowire Electrode Arrays as a Scalable Platform for Intracellular Interfacing to Neuronal Circuits. *Nat. Nanotechnol.* **2012**, *7*, 180–184.

(220) Abbott, J.; Ye, T.; Krennek, K.; Gertner, R. S.; Ban, S.; Kim, Y.; Qin, L.; Wu, W.; Park, H.; Ham, D. A Nanoelectrode Array for Obtaining Intracellular Recordings from Thousands of Connected Neurons. *Nat. Biomed. Eng.* **2020**, *4*, 232–241.

(221) Zhang, Y.; Zhang, F.; Yan, Z.; Ma, Q.; Li, X.; Huang, Y.; Rogers, J. A. Printing, Folding and Assembly Methods for Forming 3D Mesostructures in Advanced Materials. *Nat. Rev. Mater.* **2017**, *2*, 17019.

(222) Truby, R. L.; Lewis, J. A. Printing Soft Matter in Three Dimensions. *Nature* **2016**, *540*, 371–378.

(223) Jung, W.; Jung, Y. H.; Pikhitsa, P. V.; Feng, J.; Yang, Y.; Kim, M.; Tsai, H. Y.; Tanaka, T.; Shin, J.; Kim, K. Y.; et al. Three-Dimensional Nanoprinting via Charged Aerosol Jets. *Nature* **2021**, *592*, 54–59.

(224) Murphy, S. V.; Atala, A. 3D Bioprinting of Tissues and Organs. *Nat. Biotechnol.* **2014**, *32*, 773–785.

(225) Mannoor, M. S.; Jiang, Z.; James, T.; Kong, Y. L.; Malatesta, K. A.; Soboyejo, W. O.; Verma, N.; Gracias, D. H.; McAlpine, M. C. 3D Printed Bionic Ears. *Nano Lett.* **2013**, *13*, 2634–2639.

(226) Kupfer, M. E.; Lin, W. H.; Ravikumar, V.; Qiu, K.; Wang, L.; Gao, L.; Bhuiyan, D. B.; Lenz, M.; Ai, J.; Mahutga, R. R.; et al. In Situ Expansion, Differentiation, and Electromechanical Coupling of Human Cardiac Muscle in a 3D Bioprinted, Chambered Organoid. *Circ. Res.* **2020**, *127*, 207–224.

(227) Skylar-Scott, M. A.; Uzel, S. G. M.; Nam, L. L.; Ahrens, J. H.; Truby, R. L.; Damaraju, S.; Lewis, J. A. Biomanufacturing of Organ-Specific Tissues with High Cellular Density and Embedded Vascular Channels. *Sci. Adv.* **2019**, *5*, eaaw2459.

(228) Meng, F.; Meyer, C. M.; Joung, D.; Vallera, D. A.; McAlpine, M. C.; Panoskaltis-Mortari, A. 3D Bioprinted In Vitro Metastatic Models via Reconstruction of Tumor Microenvironments. *Adv. Mater.* **2019**, *31*, 1806899.

(229) Joung, D.; Truong, V.; Neitzke, C. C.; Guo, S.-Z.; Walsh, P. J.; Monat, J. R.; Meng, F.; Park, S. H.; Dutton, J. R.; Parr, A. M.; et al. 3D Printed Stem-Cell Derived Neural Progenitors Generate Spinal Cord Scaffolds. *Adv. Funct. Mater.* **2018**, *28*, 1801850.

(230) Qiu, K.; Zhao, Z.; Haghiashtiani, G.; Guo, S.-Z.; He, M.; Su, R.; Zhu, Z.; Bhuiyan, D. B.; Murugan, P.; Meng, F.; et al. 3D Printed Organ Models with Physical Properties of Tissue and Integrated Sensors. *Adv. Mater. Technol.* **2018**, *3*, 1700235.

(231) Noor, N.; Shapira, A.; Edri, R.; Gal, I.; Wertheim, L.; Dvir, T. 3D Printing of Personalized Thick and Perfusable Cardiac Patches and Hearts. *Adv. Sci.* **2019**, *6*, 1900344.

(232) Laronda, M. M.; Rutz, A. L.; Xiao, S.; Whelan, K. A.; Duncan, F. E.; Roth, E. W.; Woodruff, T. K.; Shah, R. N. A Bioprosthetic Ovary

Created Using 3D Printed Microporous Scaffolds Restores Ovarian Function in Sterilized Mice. *Nat. Commun.* **2017**, *8*, 1–10.

(233) Rutz, A. L.; Hyland, K. E.; Jakus, A. E.; Burghardt, W. R.; Shah, R. N. A Multimaterial Bioink Method for 3D Printing Tunable, Cell-Compatible Hydrogels. *Adv. Mater.* **2015**, *27*, 1607–1614.

(234) De Coppi, P.; Bartsch, G.; Siddiqui, M. M.; Xu, T.; Santos, C. C.; Perin, L.; Mostoslavsky, G.; Serre, A. C.; Snyder, E. Y.; Yoo, J. J.; et al. Isolation of Amniotic Stem Cell Lines with Potential for Therapy. *Nat. Biotechnol.* **2007**, *25*, 100–106.

(235) Kolesky, D. B.; Homan, K. A.; Skylar-Scott, M. A.; Lewis, J. A. Three-Dimensional Bioprinting of Thick Vascularized Tissues. *Proc. Natl. Acad. Sci. U. S. A.* **2016**, *113*, 3179–3184.

(236) Kolesky, D. B.; Truby, R. L.; Gladman, A. S.; Busbee, T. A.; Homan, K. A.; Lewis, J. A. 3D Bioprinting of Vascularized, Heterogeneous Cell-Laden Tissue Constructs. *Adv. Mater.* **2014**, *26*, 3124–3130.

(237) Regehy, M.; Garmshausen, Y.; Reuter, M.; König, N. F.; Israel, E.; Kelly, D. P.; Chou, C. Y.; Koch, K.; Asfari, B.; Hecht, S. Xolography for Linear Volumetric 3D Printing. *Nature* **2020**, *588*, 620–624.

(238) Bagheri, A.; Jin, J. Photopolymerization in 3D Printing. *ACS Appl. Polym. Mater.* **2019**, *1*, 593–611.

(239) Tumbleston, J. R.; Shrivanyants, D.; Ermoshkin, N.; Januszewicz, R.; Johnson, A. R.; Kelly, D.; Chen, K.; Pinschmidt, R.; Rolland, J. P.; Ermoshkin, A.; et al. Continuous Liquid Interface Production of 3D Objects. *Science (Washington, DC, U. S.)* **2015**, *347*, 1349–1352.

(240) Zheng, X.; Smith, W.; Jackson, J.; Moran, B.; Cui, H.; Chen, D.; Ye, J.; Fang, N.; Rodriguez, N.; Weisgraber, T.; et al. Multiscale Metallic Metamaterials. *Nat. Mater.* **2016**, *15*, 1100–1106.

(241) Dudukovic, N. A. A.; Fong, E. J. J.; Gameda, H. B. B.; DeOtte, J. R. R.; Cerón, M. R. R.; Moran, B. D. D.; Davis, J. T. T.; Baker, S. E. E.; Duoss, E. B. B. Cellular Fluidics. *Nature* **2021**, *595*, 58–65.

(242) Bernal, P. N.; Delrot, P.; Loterie, D.; Li, Y.; Malda, J.; Moser, C.; Levato, R. Volumetric Bioprinting of Complex Living-Tissue Constructs within Seconds. *Adv. Mater.* **2019**, *31*, 1904209.

(243) Grigoryan, B.; Paulsen, S. J.; Corbett, D. C.; Sazer, D. W.; Fortin, C. L.; Zaita, A. J.; Greenfield, P. T.; Calafat, N. J.; Gounley, J. P.; Ta, A. H.; et al. Multivascular Networks and Functional Intravascular Topologies within Biocompatible Hydrogels. *Science (Washington, DC, U. S.)* **2019**, *364*, 458–464.

(244) Hsia, C. C. W.; Hyde, D. M.; Weibel, E. R. Lung Structure and the Intrinsic Challenges of Gas Exchange. *Compr. Physiol.* **2016**, *6*, 827–895.

(245) Park, S. H.; Yang, D. Y.; Lee, K. S. Two-Photon Stereolithography for Realizing Ultraprecise Three-Dimensional Nano/Microdevices. *Laser Photonics Rev.* **2009**, *3*, 1–11.

(246) Maibohm, C.; Silvestre, O. F.; Borme, J.; Sinou, M.; Heggarty, K.; Nieder, J. B. Multi-Beam Two-Photon Polymerization for Fast Large Area 3D Periodic Structure Fabrication for Bioapplications. *Sci. Rep.* **2020**, *10*, 1–10.

(247) Zhang, B.; Gao, L.; Ma, L.; Luo, Y.; Yang, H.; Cui, Z. 3D Bioprinting: A Novel Avenue for Manufacturing Tissues and Organs. *Engineering* **2019**, *5*, 777–794.

(248) Zheng, Z.; Eglin, D.; Alini, M.; Richards, G. R.; Qin, L.; Lai, Y. Visible Light-Induced 3D Bioprinting Technologies and Corresponding Bioink Materials for Tissue Engineering: A Review. *Engineering* **2021**, *7*, 966.

(249) Kong, Y. L.; Tamargo, I. A.; Kim, H.; Johnson, B. N.; Gupta, M. K.; Koh, T.-W. W.; Chin, H.-A. A.; Steingart, D. A.; Rand, B. P.; McAlpine, M. C. 3D Printed Quantum Dot Light-Emitting Diodes. *Nano Lett.* **2014**, *14*, 7017–7023.

(250) Muth, J. T.; Vogt, D. M.; Truby, R. L.; Mengüç, Y.; Kolesky, D. B.; Wood, R. J.; Lewis, J. A. Embedded 3D Printing of Strain Sensors within Highly Stretchable Elastomers. *Adv. Mater.* **2014**, *26*, 6307–6312.

(251) Skylar-Scott, M. A.; Mueller, J.; Visser, C. W.; Lewis, J. A. Voxelated Soft Matter via Multimaterial Multinozzle 3D Printing. *Nature* **2019**, *575*, 330–335.

- (252) Skylar-Scott, M. A.; Gunasekaran, S.; Lewis, J. A. Laser-Assisted Direct Ink Writing of Planar and 3D Metal Architectures. *Proc. Natl. Acad. Sci. U. S. A.* **2016**, *113*, 6137–6142.
- (253) Zhou, N.; Liu, C.; Lewis, J. A.; Ham, D. Gigahertz Electromagnetic Structures via Direct Ink Writing for Radio-Frequency Oscillator and Transmitter Applications. *Adv. Mater.* **2017**, *29*, 1605198.
- (254) Derby, B. Printing and Prototyping of Tissues and Scaffolds. *Science (Washington, DC, U. S.)* **2012**, *338*, 921–926.
- (255) Jakus, A. E.; Rutz, A. L.; Shah, R. N. Advancing the Field of 3D Biomaterial Printing. *Biomed. Mater.* **2016**, *11*, No. 014102.
- (256) Hinton, T. J.; Jallerat, Q.; Palchesko, R. N.; Park, J. H.; Grodzicki, M. S.; Shue, H. J.; Ramadan, M. H.; Hudson, A. R.; Feinberg, A. W. Three-Dimensional Printing of Complex Biological Structures by Freeform Reversible Embedding of Suspended Hydrogels. *Sci. Adv.* **2015**, *1*, No. e1500758.
- (257) Lee, A.; Hudson, A. R.; Shiwarski, D. J.; Tashman, J. W.; Hinton, T. J.; Yerneni, S.; Bliley, J. M.; Campbell, P. G.; Feinberg, A. W. 3D Bioprinting of Collagen to Rebuild Components of the Human Heart. *Science (Washington, DC, U. S.)* **2019**, *365*, 482–487.
- (258) Song, S. W.; Lee, S.; Choe, J. K.; Kim, N. H.; Kang, J.; Lee, A. C.; Choi, Y.; Choi, A.; Jeong, Y.; Lee, W.; et al. Direct 2D-to-3D Transformation of Pen Drawings. *Sci. Adv.* **2021**, *7*, eabf3804.
- (259) Pandey, S.; Ewing, M.; Kunas, A.; Nguyen, N.; Gracias, D. H.; Menon, G. Algorithmic Design of Self-Folding Polyhedra. *Proc. Natl. Acad. Sci. U. S. A.* **2011**, *108*, 19885–19890.
- (260) Tian, Z.; Xu, B.; Wan, G.; Han, X.; Di, Z.; Chen, Z.; Mei, Y. Gaussian-Preserved, Non-Volatile Shape Morphing in Three-Dimensional Microstructures for Dual-Functional Electronic Devices. *Nat. Commun.* **2021**, *12*, No. 509.
- (261) Tang, H.; Karnausenko, D. D.; Neu, V.; Gabler, F.; Wang, S.; Liu, L.; Li, Y.; Wang, J.; Zhu, M.; Schmidt, O. G. Stress-Actuated Spiral Microelectrode for High-Performance Lithium-Ion Microbatteries. *Small* **2020**, *16*, 2002410.
- (262) Weng, Q.; Wang, S.; Liu, L.; Lu, X.; Zhu, M.; Li, Y.; Gabler, F.; Schmidt, O. G. A Compact Tube-in-Tube Microsized Lithium-Ion Battery as an Independent Microelectric Power Supply Unit. *Cell Reports Phys. Sci.* **2021**, *2*, 100429.
- (263) Zhou, X.; Tian, Z.; Kim, H. J.; Wang, Y.; Xu, B.; Pan, R.; Chang, Y. J.; Di, Z.; Zhou, P.; Mei, Y. Rolling up MoSe₂ Nanomembranes as a Sensitive Tubular Photodetector. *Small* **2019**, *15*, 1902528.
- (264) Huang, W.; Yang, Z.; Kraman, M. D.; Wang, Q.; Ou, Z.; Rojo, M. M.; Yalamarthy, A. S.; Chen, V.; Lian, F.; Ni, J. H.; et al. Monolithic Mtesla-Level Magnetic Induction by Self-Rolled-up Membrane Technology. *Sci. Adv.* **2020**, *6*, eaay4508.
- (265) Jang, H. S.; Yoo, S.; Kang, S. H.; Park, J.; Kim, G. G.; Ko, H. C. Automatic Transformation of Membrane-Type Electronic Devices into Complex 3D Structures via Extrusion Shear Printing and Thermal Relaxation of Acrylonitrile–Butadiene–Styrene Frameworks. *Adv. Funct. Mater.* **2020**, *30*, 1907384.
- (266) Na, J. H.; Bende, N. P.; Bae, J.; Santangelo, C. D.; Hayward, R. C. Grayscale Gel Lithography for Programmed Buckling of Non-Euclidean Hydrogel Plates. *Soft Matter* **2016**, *12*, 4985–4990.
- (267) Wu, Z. L.; Moshe, M.; Greener, J.; Therien-Aubin, H.; Nie, Z.; Sharon, E.; Kumacheva, E. Three-Dimensional Shape Transformations of Hydrogel Sheets Induced by Small-Scale Modulation of Internal Stresses. *Nat. Commun.* **2013**, *4*, 1–7.
- (268) Xu, C.; Wu, X.; Huang, G.; Mei, Y. Rolled-up Nanotechnology: Materials Issue and Geometry Capability. *Adv. Mater. Technol.* **2018**, *4*, 1800486.
- (269) Karnausenko, D. D.; Müntenrieder, N.; Karnausenko, D. D.; Koch, B.; Meyer, A. K.; Baunack, S.; Petti, L.; Tröster, G.; Makarov, D.; Schmidt, O. G. Biomimetic Microelectronics for Regenerative Neuronal Cuff Implants. *Adv. Mater.* **2015**, *27*, 6797–6805.
- (270) Cho, J. H.; Keung, M. D.; Verellen, N.; Lagae, L.; Moshchalkov, V. V.; Van Dorpe, P.; Gracias, D. H. Nanoscale Origami for 3D Optics. *Small* **2011**, *7*, 1943–1948.
- (271) Cho, J. H.; James, T.; Gracias, D. H. Curving Nanostructures Using Extrinsic Stress. *Adv. Mater.* **2010**, *22*, 2320–2324.
- (272) Guo, Q.; Pan, Y.; Lin, J.; Wan, G.; Xu, B.; Hua, N.; Zheng, C.; Huang, Y.; Mei, Y.; Chen, W.; et al. Programmable 3D Self-Folding Structures with Strain Engineering. *Adv. Intell. Syst.* **2020**, *2*, 2000101.
- (273) Xu, C.; Pan, R.; Guo, Q.; Wu, X.; Li, G.; Huang, G.; An, Z.; Li, X.; Mei, Y. Ultrathin Silicon Nanomembrane in a Tubular Geometry for Enhanced Photodetection. *Adv. Opt. Mater.* **2019**, *7*, 1900823.
- (274) Zakharchenko, S.; Sperling, E.; Ionov, L. Fully Biodegradable Self-Rolled Polymer Tubes: A Candidate for Tissue Engineering Scaffolds. *Biomacromolecules* **2011**, *12*, 2211–2215.
- (275) Cangellaris, O. V.; Corbin, E. A.; Froeter, P.; Michaels, J. A.; Li, X.; Gillette, M. U. Aligning Synthetic Hippocampal Neural Circuits via Self-Rolled-Up Silicon Nitride Microtube Arrays. *ACS Appl. Mater. Interfaces* **2018**, *10*, 35705–35714.
- (276) Herzer, R.; Gebert, A.; Hempel, U.; Hebenstreit, F.; Oswald, S.; Damm, C.; Schmidt, O. G.; Medina-Sánchez, M. Rolled-Up Metal Oxide Microscaffolds to Study Early Bone Formation at Single Cell Resolution. *Small* **2021**, *17*, 2005527.
- (277) Egunov, A. I.; Dou, Z.; Karnausenko, D. D.; Hebenstreit, F.; Kretschmann, N.; Akgün, K.; Ziemssen, T.; Karnausenko, D.; Medina-Sánchez, M.; Schmidt, O. G. Impedimetric Microfluidic Sensor-in-a-Tube for Label-Free Immune Cell Analysis. *Small* **2021**, *17*, 2002549.
- (278) Wu, J.; Yuan, C.; Ding, Z.; Isakov, M.; Mao, Y.; Wang, T.; Dunn, M. L.; Qi, H. J. Multi-Shape Active Composites by 3D Printing of Digital Shape Memory Polymers. *Sci. Rep.* **2016**, *6*, 1–11.
- (279) Chen, Z.; Huang, G.; Trase, I.; Han, X.; Mei, Y. Mechanical Self-Assembly of a Strain-Engineered Flexible Layer: Wrinkling, Rolling, and Twisting. *Phys. Rev. Appl.* **2016**, *5*, No. 017001.
- (280) Yan, Z.; Zhang, F.; Wang, J.; Liu, F.; Guo, X.; Nan, K.; Lin, Q.; Gao, M.; Xiao, D.; Shi, Y.; et al. Controlled Mechanical Buckling for Origami-Inspired Construction of 3D Microstructures in Advanced Materials. *Adv. Funct. Mater.* **2016**, *26*, 2629–2639.
- (281) Xu, S.; Yan, Z.; Jang, K.-I. K.-I.; Huang, W.; Fu, H.; Kim, J.; Wei, Z.; Flavin, M.; McCracken, J.; Wang, R.; et al. Assembly of Micro/Nanomaterials into Complex, Three-Dimensional a by Compressive Buckling. *Science (Washington, DC, U. S.)* **2015**, *347*, 154–159.
- (282) Zhang, Y.; Yan, Z.; Nan, K.; Xiao, D.; Liu, Y.; Luan, H.; Fu, H.; Wang, X.; Yang, Q.; Wang, J. J.; et al. A Mechanically Driven Form of Kirigami as a Route to 3D Mesostructures in Micro/Nanomembranes. *Proc. Natl. Acad. Sci. U. S. A.* **2015**, *112*, 11757–11764.
- (283) Wang, X.; Guo, X.; Ye, J.; Zheng, N.; Kohli, P.; Choi, D.; Zhang, Y.; Xie, Z.; Zhang, Q.; Luan, H.; et al. Freestanding 3D Mesostructures, Functional Devices, and Shape-Programmable Systems Based on Mechanically Induced Assembly with Shape Memory Polymers. *Adv. Mater.* **2019**, *31*, 1805615.
- (284) Fu, H.; Nan, K.; Froeter, P.; Huang, W.; Liu, Y.; Wang, Y.; Wang, J.; Yan, Z.; Luan, H.; Guo, X.; et al. Mechanically-Guided Deterministic Assembly of 3D Mesostructures Assisted by Residual Stresses. *Small* **2017**, *13*, 1700151.
- (285) Won, S. M.; Wang, H.; Kim, B. H.; Lee, K.; Jang, H.; Kwon, K.; Han, M.; Crawford, K. E.; Li, H.; Lee, Y.; et al. Multimodal Sensing with a Three-Dimensional Piezoresistive Structure. *ACS Nano* **2019**, *13*, 10972–10979.
- (286) Park, Y.; Luan, H.; Kwon, K.; Zhao, S.; Franklin, D.; Wang, H.; Zhao, H.; Bai, W.; Kim, J. U.; Lu, W.; et al. Transformable, Freestanding 3D Mesostructures Based on Transient Materials and Mechanical Interlocking. *Adv. Funct. Mater.* **2019**, *29*, 1903181.
- (287) Kim, B. H.; Liu, F.; Yu, Y.; Jang, H.; Xie, Z.; Li, K.; Lee, J. J. Y.; Jeong, J. Y.; Ryu, A.; Lee, Y.; et al. Mechanically Guided Post-Assembly of 3D Electronic Systems. *Adv. Funct. Mater.* **2018**, *28*, 1803149.
- (288) Park, Y.; Kwon, K.; Kwak, S. S.; Yang, D. S.; Kwak, J. W.; Luan, H.; Chung, T. S.; Chun, K. S.; Kim, J. U.; Jang, H.; et al. Wireless, Skin-Interfaced Sensors for Compression Therapy. *Sci. Adv.* **2020**, *6*, 1–10.
- (289) Han, M.; Wang, H.; Yang, Y.; Liang, C.; Bai, W.; Yan, Z.; Li, H.; Xue, Y.; Wang, X.; Akar, B.; et al. Three-Dimensional Piezoelectric Polymer Microsystems for Vibrational Energy Harvesting. *Robotic Interfaces and Biomedical Implants. Nat. Electron.* **2019**, *2*, 26–35.

- (290) Yan, Z.; Zhang, F.; Liu, F.; Han, M.; Ou, D.; Liu, Y.; Lin, Q.; Guo, X.; Fu, H.; Xie, Z.; et al. Mechanical Assembly of Complex, 3D Mesosstructures from Releasable Multilayers of Advanced Materials. *Sci. Adv.* **2016**, *2*, No. e1601014.
- (291) Kwak, J. W.; Han, M.; Xie, Z.; Chung, H. U.; Lee, J. Y.; Avila, R.; Yohay, J.; Chen, X.; Liang, C.; Patel, M.; et al. Wireless sensors for continuous, multimodal measurements at the skin interface with lower limb prostheses. *Sci. Transl. Med.* **2020**, *12*, eabc4327.
- (292) Han, M.; Chen, L.; Aras, K.; Liang, C.; Chen, X.; Zhao, H.; Li, K.; Faye, N. R.; Sun, B.; Kim, J. H.; et al. Catheter-Integrated Soft Multilayer Electronic Arrays for Multiplexed Sensing and Actuation during Cardiac Surgery. *Nat. Biomed. Eng.* **2020**, *4*, 997–1009.
- (293) Ryu, H.; Park, Y.; Luan, H.; Dalgin, G.; Jeffris, K.; Chung, T. S.; Yoon, H.-J.; Kim, J. U.; Kwak, S. S.; Lee, G. Transparent, Compliant 3D Mesosstructures for Precise Evaluation of Mechanical Characteristics of Organoids. *Adv. Mater.* **2021**, *33*, 2100026.
- (294) Fu, H.; Nan, K.; Bai, W.; Huang, W.; Bai, K.; Lu, L.; Zhou, C.; Liu, Y. Y.; Liu, F.; Wang, J.; et al. Morphable 3D Mesosstructures and Microelectronic Devices by Multistable Buckling Mechanics. *Nat. Mater.* **2018**, *17*, 268–276.
- (295) McCracken, J. M.; Xu, S.; Badea, A.; Jang, K.-I. K.; Yan, Z.; Wetzell, D. J.; Nan, K.; Lin, Q.; Han, M.; Anderson, M. A.; et al. 3D Scaffolds: Deterministic Integration of Biological and Soft Materials onto 3D Microscale Cellular Frameworks (Adv. Biosys. 9/2017). *Adv. Biosyst.* **2017**, *1*, 1700068.
- (296) Yan, Z.; Han, M.; Shi, Y.; Badea, A.; Yang, Y.; Kulkarni, A.; Hanson, E.; Kandel, M. E.; Wen, X.; Zhang, F.; et al. Three-Dimensional Mesosstructures as High-Temperature Growth Templates, Electronic Cellular Scaffolds, and Self-Propelled Microrobots. *Proc. Natl. Acad. Sci. U. S. A.* **2017**, *114*, E9455–E9464.
- (297) Soscia, D. A.; Lam, D.; Tooker, A. C.; Enright, H. A.; Triplett, M.; Karande, P.; Peters, S. K. G.; Sales, A. P.; Wheeler, E. K.; Fischer, N. O. A Flexible 3-Dimensional Microelectrode Array for: In Vitro Brain Models. *Lab Chip* **2020**, *20*, 901–911.
- (298) Krishnadoss, V.; Kanjilal, B.; Hesketh, A.; Miller, C.; Mugweru, A.; Akbard, M.; Khademhosseini, A.; leijten, J.; Noshadi, I. In Situ 3D Printing of Implantable Energy Storage Devices. *Chem. Eng. J.* **2021**, *409*, 128213.
- (299) Park, S. H.; Su, R.; Jeong, J.; Guo, S.-Z.; Qiu, K.; Joung, D.; Meng, F.; McAlpine, M. C. 3D Printed Polymer Photodetectors. *Adv. Mater.* **2018**, *30*, 1803980.
- (300) Joung, D.; Lavoie, N. S.; Guo, S.-Z.; Park, S. H.; Parr, A. M.; McAlpine, M. C. 3D Printed Neural Regeneration Devices. *Adv. Funct. Mater.* **2020**, *30*, 1906237.
- (301) Su, R.; Wen, J.; Su, Q.; Wiederoder, M. S.; Koester, S. J.; Uzarski, J. R.; McAlpine, M. C. 3D Printed Self-Supporting Elastomeric Structures for Multifunctional Microfluidics. *Sci. Adv.* **2020**, *6*, eabc9846.
- (302) Haghiashtiani, G.; Habtour, E.; Park, S. H.; Gardea, F.; McAlpine, M. C. 3D Printed Electrically-Driven Soft Actuators. *Extrem. Mech. Lett.* **2018**, *21*, 1–8.
- (303) Zhu, Z.; Park, H. S.; McAlpine, M. C. 3D Printed Deformable Sensors. *Sci. Adv.* **2020**, *6*, 5575–5592.
- (304) Haghiashtiani, G.; Qiu, K.; Sanchez, J. D. Z.; Fuenning, Z. J.; Nair, P.; Ahlberg, S. E.; Iaizzo, P. A.; McAlpine, M. C. 3D Printed Patient-Specific Aortic Root Models with Internal Sensors for Minimally Invasive Applications. *Sci. Adv.* **2020**, *6*, 4641–4669.
- (305) Wang, G.; McCain, M. L.; Yang, L.; He, A.; Pasqualini, F. S.; Agarwal, A.; Yuan, H.; Jiang, D.; Zhang, D.; Zangi, L.; et al. Modeling the Mitochondrial Cardiomyopathy of Barth Syndrome with Induced Pluripotent Stem Cell and Heart-on-Chip Technologies. *Nat. Med.* **2014**, *20*, 616–623.
- (306) Grosberg, A.; Alford, P. W.; McCain, M. L.; Parker, K. K. Ensembles of Engineered Cardiac Tissues for Physiological and Pharmacological Study: Heart on a Chip. *Lab Chip* **2011**, *11*, 4165–4173.
- (307) Lind, J. U.; Busbee, T. A.; Valentine, A. D.; Pasqualini, F. S.; Yuan, H.; Yadid, M.; Park, S. J.; Kotikian, A.; Nesmith, A. P.; Campbell, P. H.; et al. Instrumented Cardiac Microphysiological Devices via Multimaterial Three-Dimensional Printing. *Nat. Mater.* **2017**, *16*, 303–308.
- (308) Asulin, M.; Michael, I.; Shapira, A.; Dvir, T. One-Step 3D Printing of Heart Patches with Built-In Electronics for Performance Regulation. *Adv. Sci.* **2021**, *8*, 2004205.
- (309) Zhao, H.; Kim, Y.; Wang, H.; Ning, X.; Xu, C.; Suh, J.; Han, M.; Pagan-Diaz, G. J.; Lu, W.; Li, H.; et al. Compliant 3D Frameworks Instrumented with Strain Sensors for Characterization of Millimeter-Scale Engineered Muscle Tissues. *Proc. Natl. Acad. Sci. U. S. A.* **2021**, *118*, No. e2100077118.
- (310) Koo, B.; Choi, B.; Park, H.; Yoon, K. J. Past, Present, and Future of Brain Organoid Technology. *Mol. Cells* **2019**, *42*, 617–627.
- (311) Jo, J.; Xiao, Y.; Sun, A. X. X.; Cukuroglu, E.; Tran, H.-D. D.; Göke, J.; Tan, Z. Y. Y.; Saw, T. Y. Y.; Tan, C.-P. P.; Lokman, H.; et al. Midbrain-like Organoids from Human Pluripotent Stem Cells Contain Functional Dopaminergic and Neuromelanin-Producing Neurons. *Cell Stem Cell* **2016**, *19*, 248–257.
- (312) Mugaruma, K.; Nishiyama, A.; Kawakami, H.; Hashimoto, K.; Sasai, Y. Self-Organization of Polarized Cerebellar Tissue in 3D Culture of Human Pluripotent Stem Cells. *Cell Rep.* **2015**, *10*, 537–550.
- (313) Andersen, J.; Revah, O.; Miura, Y.; Thom, N.; Amin, N. D.; Kelley, K. W.; Singh, M.; Chen, X.; Thete, M. V.; Walczak, E. M.; et al. Generation of Functional Human 3D Cortico-Motor Assembloids. *Cell* **2020**, *183*, 1913–1929.e26.
- (314) Xiang, Y.; Tanaka, Y.; Patterson, B.; Kang, Y. J.; Govindaiah, G.; Roselaar, N.; Cakir, B.; Kim, K. Y.; Lombroso, A. P.; Hwang, S. M.; et al. Fusion of Regionally Specified hPSC-Derived Organoids Models Human Brain Development and Interneuron Migration. *Cell Stem Cell* **2017**, *21*, 383–398.e7.
- (315) Faustino Martins, J. M.; Fischer, C.; Urzi, A.; Vidal, R.; Kunz, S.; Ruffault, P. L.; Kabuss, L.; Hube, I.; Gazzero, E.; Birchmeier, C.; et al. Self-Organizing 3D Human Trunk Neuromuscular Organoids. *Cell Stem Cell* **2020**, *26*, 172–186.e6.
- (316) Nawroth, J. C.; Lee, H.; Feinberg, A. W.; Ripplinger, C. M.; McCain, M. L.; Grosberg, A.; Dabiri, J. O.; Parker, K. K. A Tissue-Engineered Jellyfish with Biomimetic Propulsion. *Nat. Biotechnol.* **2012**, *30*, 792–797.
- (317) Feinberg, A. W.; Feigel, A.; Shevkoplyas, S. S.; Sheehy, S.; Whitesides, G. M.; Parker, K. K. Muscular Thin Films for Building Actuators and Powering Devices. *Science (Washington, DC, U. S.)* **2007**, *317*, 1366–1370.
- (318) Chan, V.; Park, K.; Collens, M. B.; Kong, H.; Saif, T. A.; Bashir, R. Development of Miniaturized Walking Biological Machines. *Sci. Rep.* **2012**, *2*, No. 857.
- (319) Neal, D.; Sakar, M. S.; Ong, L.-L. S.; Asada, H. H. Formation of Elongated Fascicle-Inspired 3D Tissues Consisting of High-Density, Aligned Cells Using Sacrificial Outer Molding. *Lab Chip* **2014**, *14*, 1907–1916.
- (320) Sakar, M. S.; Neal, D.; Boudou, T.; Borochin, M. A.; Li, Y.; Weiss, R.; Kamm, R. D.; Chen, C. S.; Asada, H. H. Formation and Optogenetic Control of Engineered 3D Skeletal Muscle Bioactuators. *Lab Chip* **2012**, *12*, 4976–4985.
- (321) Cvetkovic, C.; Raman, R.; Chan, V.; Williams, B. J.; Tolish, M.; Bajaj, P.; Sakar, M. S.; Asada, H. H.; Saif, M. T. A.; Bashir, R. Three-Dimensionally Printed Biological Machines Powered by Skeletal Muscle. *Proc. Natl. Acad. Sci. U. S. A.* **2014**, *111*, 10125–10130.
- (322) Park, S. J. S.; Gazzola, M.; Park, K. S.; Park, S. J. S.; Di Santo, V.; Blevins, E. L.; Lind, J. U.; Campbell, P. H.; Dauth, S.; Capulli, A. K.; et al. Phototactic Guidance of a Tissue-Engineered Soft-Robotic Ray. *Science (Washington, DC, U. S.)* **2016**, *353*, 158–162.
- (323) Aydin, O.; Zhang, X.; Nuethong, S.; Pagan-Diaz, G. J.; Bashir, R.; Gazzola, M.; Saif, M. T. A. Neuromuscular Actuation of Biohybrid Motile Bots. *Proc. Natl. Acad. Sci. U. S. A.* **2019**, *116*, 19841–19847.
- (324) Morimoto, Y.; Onoe, H.; Takeuchi, S. Biohybrid Robot Powered by an Antagonistic Pair of Skeletal Muscle Tissues. *Sci. Robot.* **2018**, *3*, 4440.
- (325) Cho, Y.; Park, J.; Lee, C.; Lee, S. Recent Progress on Peripheral Neural Interface Technology towards Bioelectronic Medicine. *Bioelectron. Med.* **2020**, *61*, 1–10.

(326) Bettinger, C. J. Recent Advances in Materials and Flexible Electronics for Peripheral Nerve Interfaces. *Bioelectron. Med.* **2018**, *4*, 1–10.

(327) Lee, S.; Lee, C. Toward Advanced Neural Interfaces for the Peripheral Nervous System (PNS) and Their Future Applications. *Curr. Opin. Biomed. Eng.* **2018**, *6*, 130–137.

(328) Larson, C. E.; Meng, E. A Review for the Peripheral Nerve Interface Designer. *J. Neurosci. Methods* **2020**, *332*, 108523.

(329) Yu, H.; Xiong, W.; Zhang, H.; Wang, W.; Li, Z. A Parylene Self-Locking Cuff Electrode for Peripheral Nerve Stimulation and Recording. *J. Microelectromech. Syst.* **2014**, *23*, 1025–1035.

(330) Song, K.-I.; Seo, H.; Seong, D.; Kim, S.; Yu, K. J.; Kim, Y.-C.; Kim, J.; Kwon, S. J.; Han, H.-S.; Youn, I.; et al. Adaptive Self-Healing Electronic Epineurium for Chronic Bidirectional Neural Interfaces. *Nat. Commun.* **2020**, *11*, 1–10.

(331) Wark, H. A. C.; Sharma, R.; Mathews, K. S.; Fernandez, E.; Yoo, J.; Christensen, B.; Tresco, P.; Rieth, L.; Solzbacher, F.; Normann, R. A.; et al. A New High-Density (25 Electrodes/Mm²) Penetrating Microelectrode Array for Recording and Stimulating Sub-Millimeter Neuroanatomical Structures. *J. Neural Eng.* **2013**, *10*, No. 045003.

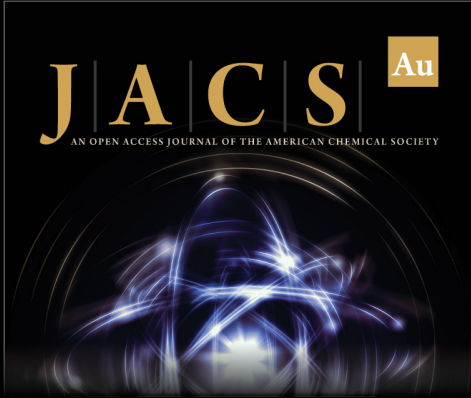
(332) Garde, K. Early Interfaced Neural Activity from Chronic Amputated Nerves. *Front. Neuroeng.* **2009**, *2*, 5.

(333) Song, K.-I.; Park, S. E.; Lee, S.; Kim, H.; Lee, S. H.; Youn, I. Compact Optical Nerve Cuff Electrode for Simultaneous Neural Activity Monitoring and Optogenetic Stimulation of Peripheral Nerves. *Sci. Rep.* **2018**, *8*, 1–11.

(334) Choi, Y. S.; Hsueh, Y. Y.; Koo, J.; Yang, Q.; Avila, R.; Hu, B.; Xie, Z.; Lee, G.; Ning, Z.; Liu, C.; et al. Stretchable, Dynamic Covalent Polymers for Soft, Long-Lived Bioresorbable Electronic Stimulators Designed to Facilitate Neuromuscular Regeneration. *Nat. Commun.* **2020**, *11*, 1–14.

NOTE ADDED AFTER ASAP PUBLICATION

This paper was published ASAP on November 5, 2021, with an error in Figure 5. This was corrected in the version posted ASAP on November 9, 2021.



JACS Au
AN OPEN ACCESS JOURNAL OF THE AMERICAN CHEMICAL SOCIETY

 Editor-in-Chief
Prof. Christopher W. Jones
Georgia Institute of Technology, USA

Open for Submissions 

pubs.acs.org/jacsau  ACS Publications
Most Trusted. Most Cited. Most Read.